Doctor Dissertation

Study on Characteristics of Tidal Current Energy and Ocean Environmental Pollution at Indonesia Archipelago

（インドネシア島嶼域における潮流エネルギー特性と海洋環境汚染に関する研究）

November 2017

Graduate School of Engineering
Faculty of Engineering
Hiroshima University

Shade Rahmawati

Abstract

Ocean has been an important source for human life and earth ecosystems. It has many potential that has not been taken for advantage, such as renewable energy. However there are also some problems in the ocean that can affect human activity, for example water pollution. The topic of the dissertation is motivated by the desire to understand in more detail not only the ocean potential including renewable energy, fishery, and aquaculture, but also the environmental problems that occurred due to human activity, especially in archipelago area. Both aspects should be balanced to keep ocean resources sustainability. Indonesian archipelago is chosen as it is one of the largest tidal current resource in the world. Investigation on tidal current characteristics and its energy potential shows that the tidal current velocity is relatively high in narrow straits at Maluku islands and Nusa Tenggara islands. In particular, Lombok strait is the most notable location with the maximum tidal current velocity, 4m/s. The narrow straits at Nusa Tenggara islands can produce more than 2.8m/s for tidal current and more than 12kW/m^2 for tidal current energy. In the northern and the southern part of Halmahera island, the resultant tidal current kinetic power also produces about 5kW/m^2.

In order to harvest the tidal current energy in Indonesia and distribute it to local communities, a small-sized HAT 10kW class with the diameter 2.2m, was theoretically and numerically designed and optimized considering the specific tidal-current at the archipelago areas, and also velocity field around the designed turbine and pressure distribution on it were examined. The designed turbine can generate electric power for more than one hundred people at Lombok strait. The power distribution produced by the designed turbine was mapped by using the estimated power curve at Maluku islands and Nusa Tenggara islands. For country with aquaculture such as Indonesia and Japan, small-sized tidal current turbine can be combined with Fish Aggregating Device (FAD) considering several sea states for practical use. FAD can also be utilized as a scientific platform to produce environment-friendly ecosystem by an artificial infrastructure. In this study, a mooring type of FAD with Horizontal Axis Turbine (HAT) and Vertical Axis Turbine (VAT) was designed considering collision with a marine vertebrate, fish and a rotational turbine. The designed FAD has been optimized to reduce fluid force and motion using elastic mooring. In Indonesian archipelago area, the estimated electric power could reach 220W in Bali strait and 700W in Lombok strait, due to higher current velocity, by using the mooring type of FAD with the designed turbine. It could be adequate to turn on LED for gathering fishes

and to boot up and activate several sensors such as beacon, ocean environmental, disaster and security devices.

In order to accomplish the balance between coastal development and ecosystem sustainability, environmental research should be conducted especially in urban coastal area such as enclosed sea in Japan. Study on hydrogen sulfide reduction in order to recover ocean environment by utilizing recycled material had been conducted using Eulerian-Lagrangian model with ocean circulation model in order to consider fluid-particle interaction between tidal current and steelmaking slag, and advection-diffusion of dissolved sulfide. The model was also applied to Fukuyama inner harbor and Tokyo Bay using the experimental and field data. The numerical results demonstrated that steelmaking slag can control advection-diffusion of concentration of DO and H_2S which is highly toxic and fatal to benthic organisms and it causes oxygen-deficient water and the blue tide at the dredged trench in Tokyo Bay. Accordingly, steelmaking slag could improve organically enriched sea bottom in enclosed sea area.

Furthermore, preliminary assessment of ocean pollution effect on fishery and aquaculture is a very important step in order to prevent further marine production loss and ocean environmental damage in Indonesian seas. Sunda Strait is chosen to be specific study site because it is one of important strait where industry, transportation, and tourism are heavily established, while fishery has been a major income for local communities. Environmental analyses of marine pollution in Sunda Strait, which consider the tidal current flow in South East Monsoon (SEM) and North West Monsoon (NWM) seasons are simulated for one month period at each case. Pb (lead) has chosen as the main contaminant because of its high concentration in this area. Validations with field data shows good agreement with little discrepancy which does not affect the end results of the simulations. SEM case results show dominant flow to the north which affect the Pb (lead) and Suspended Solid (SS) concentration distribution. In NWM case, tidal current flows to south mostly and spread Pb and SS concentration to wider area from the east to the west side of the strait. This is also affect more contaminated area which has lower photosynthesis rate of phytoplankton algae, about 60-75%. Meanwhile, in 5km radius from Source1 of Pb concentration, photosynthesis rate is very low, or nearly 0%, and threaten the living ability of the phytoplankton algae. Moreover, high SS concentration phenomena in Sunda Strait as part of tropic area could also decrease algae photosynthesis rate because of less sunlight penetration.

Acknowledgements

I would like to express my best gratitude to my advisor, Asc. Prof. Hidemi Mutsuda who have been helping me in academic and also in settling down for Japan life in Hiroshima University. With his inspiration and enthusiasm, he provided valuable advice, ideas, and guidance for my research and helped me in the writing of this dissertation. It is my honour being his student. I also wish to express my gratitude to Prof.Yasuaki Doi as the head of Fluid Dynamics for Vehicle and Environmental Systems Laboratory, Hiroshima University and also as my second advisor for his genuine support, valuable advice, sincere comments and encouragement which help me a lot to finish this study. I would like to express my gratitude to Prof. Hironori Yasukawa from Marine Transportation System Laboratory and Prof. Hidetsugu Iwashita from Airworthiness and Seakeeping for Vehicles Laboratory for their excellent advice and detailed review which very beneficial during the preparation of this dissertation. I would like to express my gratitude to Ast. Prof. Takuji Nakashima for his many important advice, suggestions, and insightful discussions in my study. I would also like to express my gratitude to Prof. Arata Kaneko from Ocean-Atmosphere Systems Laboratory for for their help in Indonesian tidal-current research using CAT system.

I would also like to acknowledge Mr. Yasuo Moriyama from SAKAI OVEX Co. Ltd., and Mr. Inaba from COAST Co. Ltd. as research collaborators in the Fish Aggregating Device (FAD) research. I also would like to acknowledge Mr.Yasuhito Miyata from JFE Steel Co. and Mr. Inaba from COAST Co. Ltd. Japan, as the research collaborator of the Steelmaking Slag research. I would also like to acknowledge Mr.Syunsyuke Yokota, Mr.Syunsyuke Hada, Mr.Taiga Kanehira, and Ms.Erika Yoshitomi as former student of Fluid Dynamics for Vehicle and Environmental Systems Laboratory, Hiroshima University for their help in researches and other laboratory activities. My gratitude also extends to Andi Ardianti from Hasanuddin University, Iis Rohmawati, Aruni Dinan Hanifa, and other members of Fluid Dynamics for Vehicle and Environmental Systems Laboratory, Hiroshima University for their genuine help, support, and advices during my doctoral study. I am particularly grateful to my Indonesian friends in Hiroshima for their support and contribution in my study and daily life in Japan. I would also to extends my gratitude to my collague in Institut Teknologi Sepuluh Nopember (ITS) Surabaya. Finally, I warmly thank and appreciate my family for their great encouragement and support for me in pursuing the doctoral degree.

Contents

Abstract **i**

Acknowledgements **iii**

1 Introduction **1**

1.1 Background 1

1.1.1 Ocean Energy 1

1.1.2 Ocean Energy Harvester 3

1.1.3 Ocean Environment 5

1.1.4 Archipelago Area 6

1.2 Aims and Objectives 9

1.3 Structure of The Dissertation 10

Bibliography 11

2 Estimation of Tidal Current Energy in Indonesia **15**

2.1 Characteristics of A Focused Site in Indonesia 15

2.2 Computational Domains and Conditions 16

2.3 Validations 18

2.4 Estimation of Tidal Current Energy at Archipelago in Indonesia 20

2.5 Conclusions 27

Bibliography 27

3 Design of Small-sized Tidal-current Turbine for Archipelago in Indonesia 31

3.1 Selection of Suitable Hydrofoil 32

3.2 Small-sized Turbine Design and Its Optimization 33

3.3 Hydrodynamic Performance of The Designed Turbine 35

3.4 Estimation of Electric Power at Archipelago of Indonesia 37

3.5 Conclusions 41

Bibliography 42

4 Fish Aggregating Device (FAD) with Ocean Energy Harvester 43

4.1 Overview of FAD 43

4.2 Design of FAD 45

4.3 Design of Current Turbine inside FAD 47

4.4 Experimental Setup 48

4.5 Computational Fluid Analysis for FAD 52

4.6 Theoretical Analysis of Fluid Force on FAD 53

4.7 Blade Element Momentum Theory for Blades of HAT and VAT 55

4.8 Fluid Force on FAD and Its Motions 56

4.8.1 Validation 56

4.8.2 Characteristics of Fluid Force and Flow Field around FAD 59

4.8.3 Reduction of Mooring Forces and Motions 65

4.9 Electric Performance of The Designed Turbine inside FAD 68

4.9.1 Validation and Optimization 68

4.9.2 Power Estimation 70

4.10 Conclusions 73

Bibliography 75

5 Numerical Model on Restoration of Ocean Environment using Steelmaking Slag 79

5.1 Steelmaking Slag in Ocean Restoration 79

5.2 Overview of Field Experiment 81

5.3 Numerical Model 82

5.3.1 Eulerian-Lagrangian Model for Local Area 82

5.3.2 Ocean Circulation Model for Global Area 91

5.4 Validation with Field Experimental Data 97

5.5 Reduction Effect of Dissolved Sulfide using Steelmaking Slag 98

5.6 Application to Tokyo Bay 100

5.7 Conclusions 107

Bibliography 107

6 Prelim. Assessment of Ocean Pollution Effect in Sunda Strait **113**

6.1 Overview of Sunda Strait Environment Conditions 113

6.2 Method 115

6.3 Results and Validation 118

6.4 Conclusions 126

Bibliography 126

7 Conclusions and Future Works **131**

7.1 Conclusions 131

7.2 Future Works 134

List of Tables

3.1 Principal parameters for the designed blade 35

3.2 Computational conditions 39

4.1 Deformation, stress, and strain at survival condition 64

4.2 Design parameters at three different types of NREL S814 for HAT 70

4.3 Design parameters at three different types of NACA0018 for VAT 70

5.1 Computational conditions 95

6.1 Computational conditions 118

List of Figures

1.1 World map of the distribution of tidal current energy based on OSCAR 1/3 degree [3] 2

1.2 Overview of tidal and wave energy harvesting activities in 2014 [4] 3

1.3 Tidal current turbine project in UK (Seagen) by Marine Current Turbine (MCT) and Norway (E-Tide) by Hammerfest Strøm [5] 4

1.4 Coral reef degradation in Florida due to ocean pollution [12] 6

1.5 Ocean renewable energy resources map [22] including Indonesian Throughflow (ITF) [25] 8

1.6 One of ocean pollution in Indonesia from industrial waste which lead to aquaculture damage[27] 8

2.1 Bottom topography in computational domain [15] 17

2.2 Comparisons of time histories in sea surface elevation with the observation data, IOC 19

2.3 Comparisons of tidal current distribution in Bali Strait 21

2.4 Correlation of tidal current between computational results and CAT field data in Bali Strait (left: north current, right: south current) 22

2.5 Depth-averaged tidal current distribution in whole Indonesian sea 23

2.6 Depth-averaged tidal current velocity and energy distribution in Maluku islands 23

2.7 Depth-averaged tidal current velocity and energy distribution in Nusa Tenggara islands 24

2.8 Characteristics of flow direction on Hodograph 24

2.9 Time Variation of tidal current power during one month 25

2.10 Bottom topography at Lombok Strait 26

2.11 Detailed velocity distribution at Lombok Strait 26

3.1 Characteristics of lift-drag ratio C_L/C_D and lift force coefficient C_L versus angle of attack (AoA) for NREL S814 hydrofoil at different Reynolds number. 33

3.2 Characteristics of velocity and pressure fields around NREL S814 hydrofoil at AoA 8° and water velocity 3m/s 34

3.3 Optimization of chord length and twist angle with blade radius 35

3.4 Bird's eye view of 10 kW HAT rotor blade designed for archipelago area 36

3.5 Tetrahedral grid generation on the designed blade 37

3.6 Computational domain and boundary conditions 37

3.7 Hydrodynamic performance of the designed HAT 10kW 38

3.8 Estimated torque of the designed blade with current speed 38

3.9 Power coefficient curve of the designed turbine with TSR 39

3.10 Estimated power curve of the designed HAT 10kW with current speed 40

3.11 Estimated electric power generated by the designed HAT at (a) Maluku islands and (b) Nusa Tenggara islands 41

4.1 Illustration of mooring type of Fish Aggregating Device (FAD) 46

4.2 Snapshots of mooring type of FAD surrounded by many swimming fishes recorded by a diver in real sea condition 46

4.3 Illustration of FAD with ocean energy harvester 47

4.4 Mooring situations of FAD in several sea states 47

4.5 A current turbine installed at bottom part of FAD, (a) HAT and (b) VAT . . . 48

4.6 Overview of FAD model in real scale (left) and model scale 1/100 (right) 50

4.7 Experimental setup and measuring system in towing tank 50

4.8 Mooring model of FAD with elastic rubber 51

4.9 Relations between tensile force and strain of elastic mooring part 51

4.10 Example of time history of mooring force acting on Model-A 57

4.11 Comparison of wave force on FAD between numerical result and experimental one 58

4.12 Comparison of current force on FAD between numerical result and experimental one 58

4.13 Comparison of wave-current force on FAD between numerical result and experimental one when the current velocity is 0.1 m/s 58

4.14 Comparison of wave-current force on FAD between numerical result and experimental one when the current velocity is 0.25 m/s 59

4.15 Comparison of inclined angle of FAD caused by current 59

4.16 Comparison of fluid force due to wave-current interaction with wave steepness . 60

4.17 Streamline around FAD with turbine and pressure distribution on FAD at low velocity condition 61

4.18 Streamline around FAD with turbine and pressure distribution on FAD at high velocity condition 62

4.19 Streamline around HAT at high velocity condition 62

4.20 Streamline around VAT at low velocity condition 62

4.21 Pressure distribution on (a) horizontal, and (b) vertical axis tidal current turbine 63

4.22 Mechanical response on (a) horizontal and (b) vertical axis turbine in survival condition 64

4.23 Time history of mooring force in Model-A 66

4.24 Reduction ratio of snap load with wave steepness H/λ 66

4.25 Example of time history of sway motion of FAD at $U = 0.2$m/s 67

4.26 Reduction ratio of sway motion in Model-B 67

4.27 Reduction ratio of surge motion in Model-B 68

4.28 Reduction ratio of heave motion in Model-B 68

4.29 Comparison of lift coefficient with AoA 69

4.30 Comparison of chord length and twist angle with blade radius at each designed HAT 70

4.31 Power coefficient of designed turbine with tip speed ratio at each type 71

4.32 Estimated power of the designed turbine at each current condition 71

4.33 Tidal current distribution computed by ocean circulation model[33] in a typical archipelago area with active fishery and aquacultures in Indonesia 72

4.34 Distribution of estimated electric power generated by the designed turbine . . . 72

4.35 First prototype of FAD installed near Okinawa island in Japan 75

5.1 Field experimental site at Fukuyama inner harbor. 82

5.2 Arrangement of grids and particles in computational domain (Left: Definition of density function and particles, Right : Staggered grid system) 85

5.3 Computational domain and condition in Fukuyama inner harbor 92

5.4 One example of time histories of tidal current velocity 92

5.5 Computational domain and bottom topography including trench and navigation channel 94

5.6 Comparison of turbidity to current velocity between sediment and sediment-slag 96

5.7 Relationship between turbidity and Suspended Solids (SS) 96

5.8 Comparison of dissolved sulfide between slag and sediment (mud) 96

5.9 Relationship between H_2S and DO [29] 96

5.10 Comparison of tidal elevation at the nearest location, Onoshima, provided by JMA 98

5.11 Comparison of dissolved sulfide at three different vertical positions with filed experimental data in Fukuyama inner harbor 99

5.12 Comparison of spatial distribution of dissolved sulfide for three different vertical constructions 100

5.13 Comparison of vertical distribution of dissolved sulfide for three different construction conditions 101

5.14 Comparison of time history of water elevation between model results, prediction and observed ones by JMA 102

5.15 Comparison of time history of current velocity near sea bottom with the observed data at Tokyo light beacon 103

5.16 One example of velocity field in flood tide and ebb tide at whole area of Tokyo Bay 103

5.17 Spatial variation of dissolved oxygen, DO in Makuhari trench 104

5.18 Spatial variation of dissolved oxygen, DO in Funabashi line 104

5.19 Spatial variation of hydrogen sulfide (H_2S) in Makuhari trench 105

5.20 Spatial variation of hydrogen sulfide (H_2S) in Funabashi line 105

5.21 Spatial variation of suspended solid (SS) in Funabashi line 105

5.22 Time histories of DO at Makuhari trench (St.2 and St.4) and Funabashi line (St.10 and St.12) 106

5.23 Time histories of H_2S at Makuhari trench (St.2 and St.4) and Funabashi line (St.10 and St.12) 106

5.24 Time histories of SS at Funabashi line (St.10 and St.12) 106

6.1 Main study site location of Sunda Strait in Indonesia. Study site is marked with yellow square. 114

6.2 Topography map of Sunda Strait including pollutant point sources and monitoring points of numerical model 117

6.3 Photosynthesis rate of *Bacillariophyceae* algae after 72hours laboratory treatment [14] 118

6.4 Water elevation of Sunda Strait in SEM and NWM season validated with tide data from Geospatial Information Agency Indonesia [24] 119

6.5 Tidal current flow in Sunda Strait at different monsoon season 120

6.6 Pb distribution from point-sources due to tidal current flow and Algae photosynthesis rate due to Pb contamination in SEM season 121

6.7 Pb distribution from point-sources due to tidal current flow and Algae photosynthesis rate due to Pb contamination in NWM season 122

6.8 distribution from point-sources due to tidal current flow in SEM and NWM season123

6.9 Time histories of Pb concentration and algae photosynthesys rate in Sunda Strait during SEM season 124

6.10 Time histories of Pb concentration and algae photosynthesys rate in Sunda Strait during NWM season 125

6.11 Time histories of SS concentration in Sunda Strait during SEM and NWM season125

Chapter 1

Introduction

1.1 Background

Ocean has been an important source for human life and earth ecosystems. It has many potential that has not been taken for advantage, such as renewable energy. However there are also some problems in the ocean that can affect human activity, for example water pollution. To take the advantage from the ocean and to keep its sustainability as a support system of earth ecosystem, it is important to understand both aspect in detail. At this point, the author would like to specifically investigate the potential and the problem of certain location in the world, so that the solutions are more detail and practical for real application, especially in archipelago area which has vast ocean territory. Below the author will explain the research backgrounds about: (1) ocean energy potential, (2) ocean energy harvesting method, (3) ocean environment problem, and (4) potential study site that is archipelago area.

1.1.1 Ocean Energy

Ocean as the largest portion of the earth contains huge renewable energy resources from tidal current 50-100 GW, 2 TW wave, ocean thermal 10 TW, and over than 100 GW offshore wind [1]. Those amount of energy can meet total worldwide demand for power many times over if

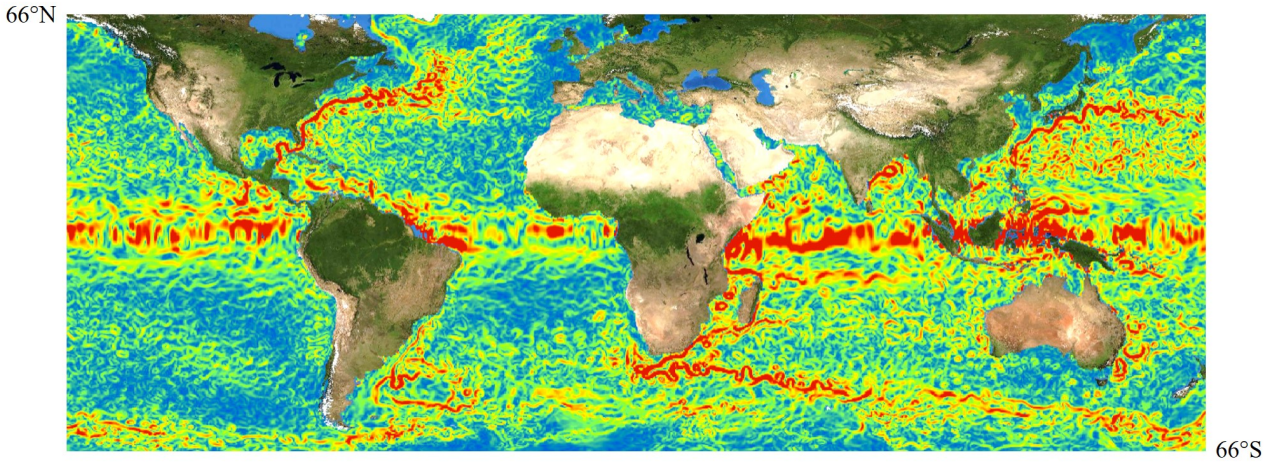

Figure 1.1: World map of the distribution of tidal current energy based on OSCAR 1/3 degree [3]

harvested effectively [2]. Among the various above-mentioned existing resources, tidal current power has the distinct advantage of being highly predictable, compared to wave, wind, and solar energy. Spring tide (high tide) occurs on new as well as full moon and neap tide (low tide) occurs in waxing or waning half moon due to misalignment of the earth and the sun. Based on Ocean Surface Current Analyses Real-time (OSCAR) 1/3 degree data which belongs to Earth & Space Research (ESR) [3], a color map estimates tidal current energy dissipation in the ocean between 66°N and 66°S as shown in Fig.1.1. Red areas show high energy territory. It can be seen that there are many high energy sources in the world. However, small islands especially in archipelago area are the most likely to get the highest advantage of the tidal current energy by exploit the straits among them, such as in Indonesia.

In fact, tidal current energy resource has not yet been utilized in many potential area. In its annual report in 2014, Ocean Energy System (OES), an intergovernmental collaboration established by the International Energy Agency in Paris known as 'Implementing Agreement on Ocean Energy Systems', summarize the tidal and wave energy harvesting activities worldwide as shown in Fig.1.2 [4]. The possibilities to explore more tidal current energy are wide open as the potential of tidal current energy in archipelago areas is explained in subsection 1.1.4, and along with an immense energy potential, the tides regularity helps make tidal current energy development attractive. The ocean energy harvesters that potentially to be used to harvest tidal current energy are explained in next subsection.

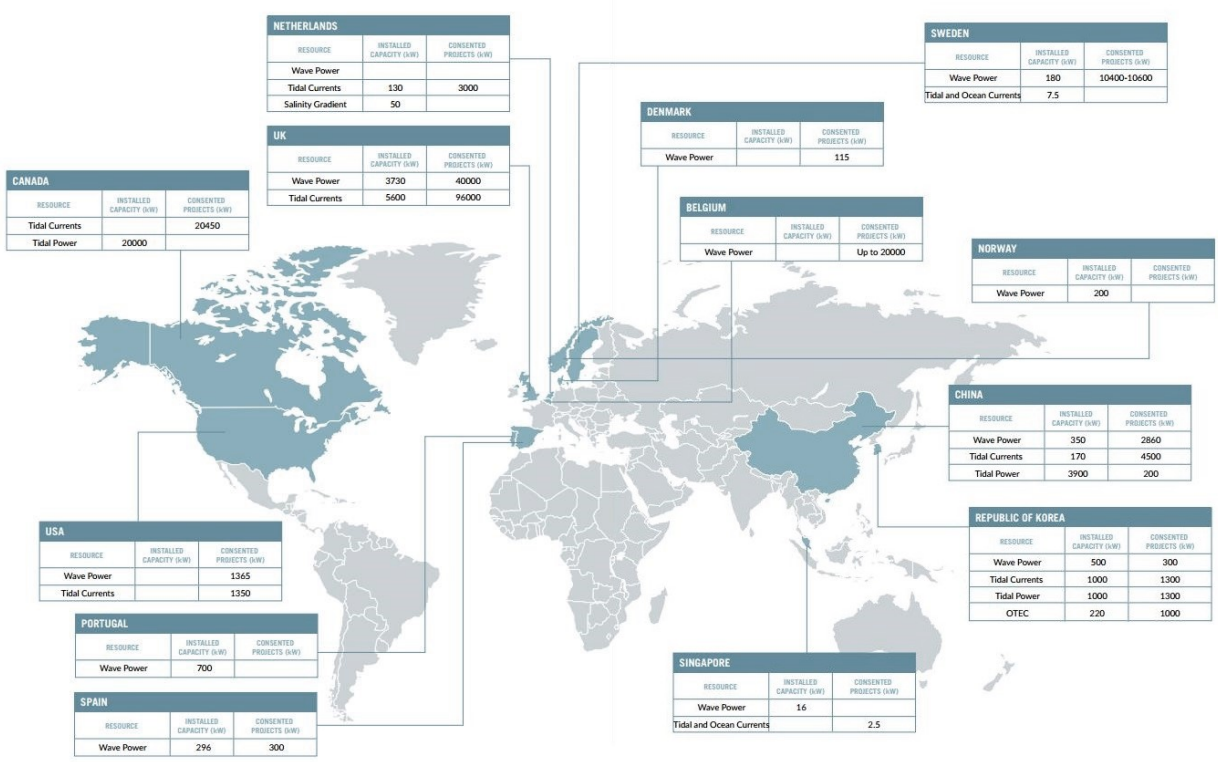

Figure 1.2: Overview of tidal and wave energy harvesting activities in 2014 [4]

1.1.2 Ocean Energy Harvester

By deciding to harvest tidal current energy, the harvesting method should also be defined by select the most suitable energy harvester, depend on the installation site characteristic, although the most common harvesting method is by generate the electricity from generator that activated by rotor rotation due to tidal stream force which we called as tidal current turbine. In general, there are two types of tidal current turbine, horizontal axis turbine (HAT) and vertical axis turbine (VAT). HAT type is suitable at one direction flow and its effective to harvest high velocity flow. Otherwise, VAT type can handle multi-direction flow and also drag-type of VAT can be operated even if tidal current is relatively low. To decide a suitable type of tidal current turbine and design it, a flow direction and dominant velocity should be carefully examined at archipelago region where potential energy due to tidal current is so high.

Tidal current energy harvesting is actually inspired by wind power which is more mature with its rapid advancements in technology over the past two decades. Many kinds of large tidal current turbine has been studied under commercial research and been examined its performance

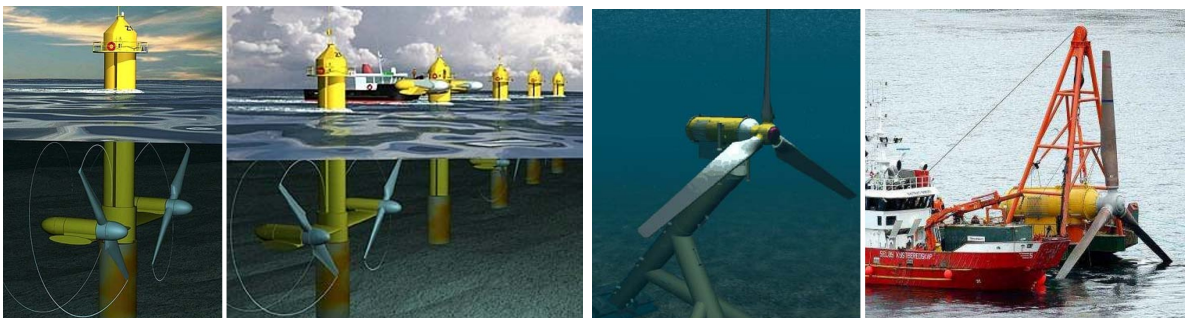

Figure 1.3: Tidal current turbine project in UK (Seagen) by Marine Current Turbine (MCT) and Norway (E-Tide) by Hammerfest Strøm [5]

practically. HAT were installed in ht Bristol Channel between Wales and England, VAT were installed in Messina Strait between Sicily and Italy. HATs include 1-2 MW Tidal Stream, Lunar energy, TidEL, Hydrovision, Sea Flow and Seagen (UK), 0.75-1 MW Blue Tide (Norway) and 1 MW HydroHelix (France). VATs include 20 kW Enermar (Italy), 200 kw Blue Energy (Canada), 180 kW - 1 MW Gorlov Helical (USA), 90-250 kW Stingray (UK) and OpenCentre (Ireland) [5]. Some of the projects have been installed and operated as shown in Fig.1.3. Along with large energy results, large turbine also has many consequences, not only for its high production and maintenance cost, but also to environment. The structure could affect the sediment transport and damage the underwater ecosystems. During the construction process of tidal turbine in La Rance (France), the estuary was entirely closed off from the ocean for about 3 year, which lead to damaged ecological equilibrium. Change caused by the structure include reduced range of salinity, a reduction in intertidal area, changed bottom water characteristics, and slower current flow [1].

In contrast to a commercial tidal current turbine, a small scale turbine suitable for archipelagos have not been advanced at the same rate as a commercial turbine due to limited location in space and sea state condition, low efficiency, as well as highly cost for construction and maintenance. A small scale tidal current turbine have the potential to be utilized and integrated into local residential environments near coastal area, especially in developing country. The tidal current flow in nearshore zone and complicated straits among islands has many specific characteristics. To avoid a big energy crisis as Tohoku earthquake in Japan 2011, the tidal current energy harvesting for a dispersed local community could be necessary and important infrastructure connecting the life line. Therefore the local community requires a small-sized

and dispersed energy harvester without electric cables rather than a big-sized and concentrated energy harvester with longer cables for power supply. By developing the suitable tidal current turbines for each specific area, energy harvesting will be more effective and easy to be accessed by local communities. Small tidal current turbines also could be the most environmentally friendly tidal power option. They do not block large area of channels, interrupt fish migration or alter hydrology [6]. Small scale tidal current turbine can be applied as a solitary device or it can be combined with another device as an energy supplier for independent structure, such as ocean buoy that contain data censors.

1.1.3 Ocean Environment

About half of world's population is living within 200 kilometers of a coastline [7]. Coastal urbanization and industrialization has brought many economic advantages in many sector to human life. However, it also bring water pollution as the side effect. In recent years, the continuing threat of pollution on coastal and marine environment has been addressed on regional scale [8].

Marine and coastal pollution can be caused by several case. First, it can be caused by land-based wast disposal. Mostly it contains water contaminants such as chemical materials and heavy metals. Heavy metals are conventionally defines as elements with metallic properties and an atomic number >20. The most common heavy metal contaminants are Cd, Cr, Cu, Hg, Pb, and Zn. Metals are natural components in soil [9]. Some of these metals are micronutrients necessary for plant growth, such as Zn, Cu, Mn, Ni, and Co, while others have unknown biological function such as Cd, Pb, and Hg [10]. Metal pollution also has harmful effect on biological systems and does not undergo biodegradation. Toxic heavy metals such as Pb, Co, Cd can be differentiated from other pollutants, since they can not be biodegraded but can be accumulated in living organisms, thus causing various diseases and disorders en in relatively lower concentrations [11]. Fig.1.4 shows ocean pollution effect on coral reefs [12] which undergo degradation by pollution increase. Heavy metals, with soil residence times of thousands of years, pose numerous health dangers to higher organisms. They are also known to have effect

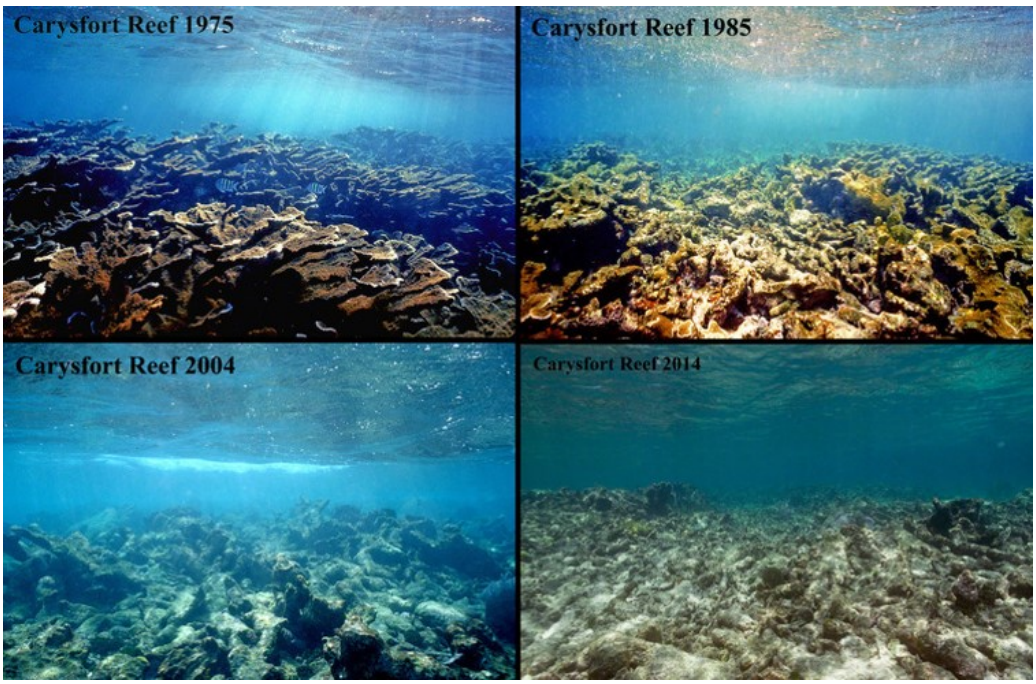

Figure 1.4: Coral reef degradation in Florida due to ocean pollution [12]

on plant growth, ground cover and have a negative impact on soil microflora [13]. It is well known that heavy metals can not be chemically degraded and need to be physically removed or be transformed into nontoxic compounds [10]. Ocean pollution also can be occurred due to ecosystem equilibrium damage. For example, hydrogen sulfide is often generated due to sulfate reduction under anaerobic conditions in the sea bottom which caused by coastal dredging. Hydrogen sulfide highly toxic, depletes oxygen and forms blue tides. Hydrogen sulfides are highly toxic and fatal to benthic organisms and could cause oxygen deficiency which lead to blue tide [14]. The balance between economic development and environment sustainability is very important. Therefore, investigation of ocean pollution must be taken and based on scientific information. Moreover, research about pollution effects on fisheries and aquaculture in certain area should also be done to estimate the quantitative damages [15].

1.1.4 Archipelago Area

Considering benefits and problems that facing ocean environment management, archipelago area is the most affected site and therefore is also an important research object. With an area dominated by seas, archipelago area has abundant resources of renewable energy from ocean but

also complex problems in the matter of marine pollution. Many researches have been conducted to boost archipelago area productivity whether in term of fishery [16] or energy harvesting [17], or otherwise to solve the environmental problems [18]. Because each area is unique with its ocean environment characteristics, most of the researches are specific for only one area and can not be generalized for all cases. Therefore, this study should be specifically focused on some archipelago area which can be developed more.

In Asia, there are several countries with potential archipelago area, such as Japan and Indonesia. Indonesia as the second largest fish producing country [19] is a rapid developing country which now also concern in renewable energy harvesting to support its local development especially for remote area and ocean environment issues to keep marine sustainability. Several researches has been conducted to study ocean renewable energy [20][21][22][23] and it is understood that Indonesia has large energy resources which can be extracted and distributed in whole area especially in eastern part where Indonesian Throughflow (ITF), or the current flow from Pacific Ocean to Indian Ocean, is exist [24] as shown in Fig.1.5. However, the previous researches only gave the estimation of energy potential. The suitable device to harvest the energy is not proposed yet. It is can be seen in previous Fig.1.2 that in Indonesia there is still no ocean energy harvesting activities yet. In order to support the ocean energy development, especially the tidal current power, potential area should be described with detail flow characteristics, then the suitable energy harvesting device should be designed. As the consequence of developing and rapid urbanization at coastal region, ocean pollution are occurred mostly as the effect of land-based waste disposal, especially around Java Island which is the most inhabited island in Indonesia, and causing reef degradation and coral biodiversity decline [26]. Fig.1.6 shows one of ocean pollution in Indonesia which came from industrial waste and damaged the aquaculture [27]. The pollutants are over the allowed threshold, especially the heavy metals contaminant [28]. Recovery step should be taken so that larger damage can be avoided in the future. Therefore, a preliminary research about ocean pollution and its effect on fishery and aquaculture should be conducted considering ocean circulation as Indonesian seas are under the effect of monsoon seasons. Meanwhile, Japan is one of most rapid country in industrial development. Unfortunately, in recent years, there is an increase in environmental pollution which come

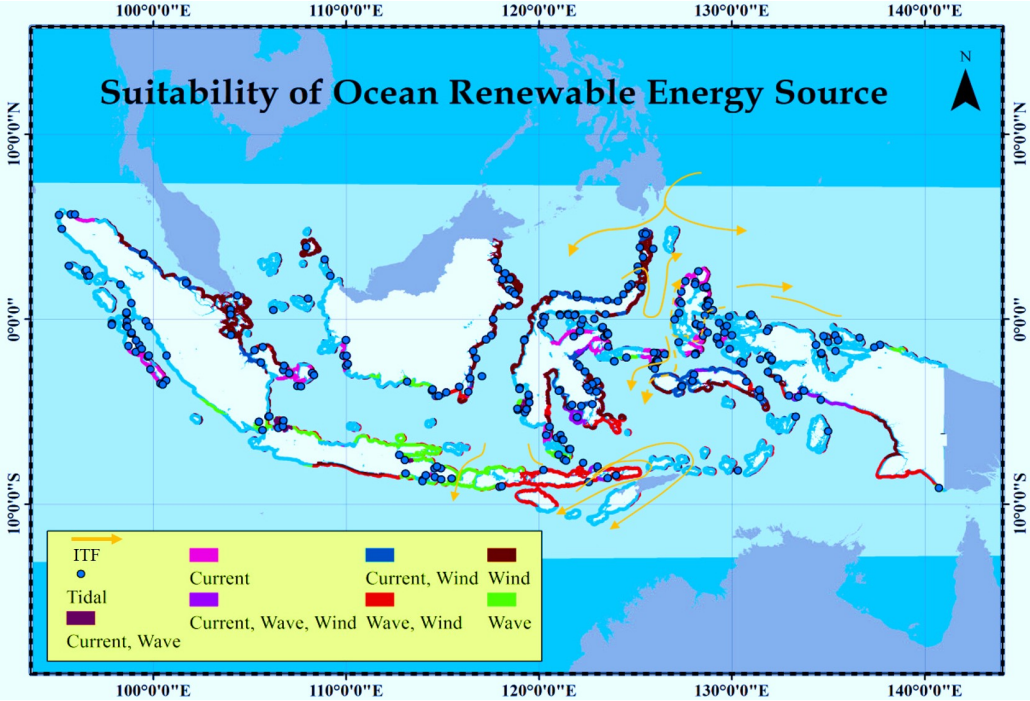

Figure 1.5: Ocean renewable energy resources map [22] including Indonesian Throughflow (ITF) [25]

Figure 1.6: One of ocean pollution in Indonesia from industrial waste which lead to aquaculture damage[27]

to serious proportion especially in bays and inland seas. Classification according to source and type of marine pollution revealed that the major cases were due to industrial wastes and dredging operations [29]. These environmental changes have caused severe damage to living resources and fisheries. Ichioka [30] had studied sulfide as the cause of blue tide in navigation channel and dredged channel in Tokyo Bay. In the other hand, deterioration of sedimentary environment can also affect benthic organism [31]. This condition lead to the urgency to develop the technical solution to reduce the ocean pollution and recover coastal environment quality which Japan government has encouraged to use the recycled material such as steelmaking slag [32].

1.2 Aims and Objectives

Based on previous researches, it is very important to understand the potential ocean energy resource, especially in archipelago area which is not yet well describe. Moreover, ocean energy harvester should also be designed to be applied in target area. The different point, instead of using large turbine, small-sized turbine is the chosen device for harvesting energy in local area to provide electricity with low transmission and maintenance cost. Finally, the environmental condition should also be analyzed to accomplish the balance between coastal development and ecosystem sustainability.

Within this aim, the specific objectives of this study to be reach are focused to the followings:

- Investigation on tidal current characteristics and its energy potential in Indonesian archipelago area, as it is one of the largest tidal current resource in the world.
- Design a small scale tidal current turbine dedicated for a specific potential site considering characteristics of tidal current at Indonesian archipelago area
- Develop a new type of Fish Aggregating Device with an ocean energy harvester based on numerical and experimental works considering several sea states for practical use, especially for country with aquaculture such as Indonesia and Japan.
- Investigation on advection-diffusion of dissolved sulfide based on the results in the field experiment using numerical models with considering fluid-particle interaction between ocean circulation and steelmaking slag. This step shows the innovation in recovering the ocean environment by using recycled material.
- Investigation on marine pollution in Indonesia based on numerical estimation in different monsoon seasons and its effect on fisheries and aquaculture. This research is very important as the preliminary step to resolve the pollution problem in Indonesian ocean and avoid further loss of marine resources. By considering tidal current flow in different monsoon season in Indonesia, pollutant distribution can be estimated and spatial effect on marine aquaculture can be predicted, which was not achieved in other researches before.

1.3 Structure of The Dissertation

The dissertation is structured as follows. Chapter 1 introduce and explain the background of this study which provides previous researches in relation to this study. Hereafter, the author clarify the objectives of the study and close this chapter by the structure of dissertation. In order to harvest the ocean renewable energy in Indonesian archipelago, target location should be investigated from whole area to specific site on details. Therefore, Chapter 2 explains the tidal current energy estimation in archipelago in Indonesia by using an ocean circulation model for whole area and computational fluid dynamic method to analyze the local tidal current flow in more specific chosen area. Chapter 3 follow up the previous chapter by providing the suitable small-sized turbine in order to harvest the estimated potential tidal current energy. The proposed small-sized tidal current turbine is designed considering the flow characteristics of target installation site, including hydrodynamic performance and generated power estimation so that it is applicable in field application. By using small-sized turbines, it is expected to be more ecosystem friendly and less production and maintenance cost. In Chapter 3, the small-sized turbine is designed to be a solitary operating device to fulfill energy needs especially in remote area. Then in the next chapter, the use of small-sized turbine is proposed to be a supporting component to supply electrical power for an ocean structure. In chapter 4, a new type of Fish Aggregating Devices (FADs), which is an environment-friendly artificial ocean infrastructure, is proposed and developed together with a small-sized current turbine to generate independent electric power for navigational and environmental sensors, especially at archipelago areas with fishery and aquaculture. The hydrodynamic and mechanical responses of FAD including the turbine are investigated to make sure its ability to operate in ocean environment especially in extreme condition.

In order to keep the balance between marine-based development and ocean sustainability, the study to reduce the negative impacts on ocean environment should be taken. First, the research is focused in Japan area because its sufficient field data, and some field experiments were done in previous research. Chapter 5 is concerning about the remediation of contaminated seas by employing the steelmaking slag in order to reduce the hydrogen sulfides concentration in en-

closed seas in Japan. In this chapter, a numerical model has been proposed and developed using Eulerian-Lagrangian model coupled with ocean circulation model in order to compute advection-diffusion of dissolved sulfide and fluid-particle interaction between ocean circulation and steelmaking slag. The model is applied to Fukuyama inner harbor and Tokyo Bay comparing with field experiment data. After that, the study continues to explore the marine pollution in archipelago in Indonesia in Chapter 6. The marine pollution is investigated using an ocean circulation model in order to understand the contaminant distribution and its effects on fishery and aquaculture so that the ocean remediation method can be prepared for specific area in the future. In the end, all of the researches are concluded in Chapter 7 and the future works that should be taken are presented.

Bibliography

[1] Robin Pelc and Rod M. Fujita. Renewable energy from the ocean. *Marine Policy*, 26(6):471–479, 2002.

[2] Patrick K. Takahashi and Andrew Trenka. Ocean thermal energy conversion: Its promise as a total resource system. *Energy*, 17(7):657–668, 1992.

[3] Earth and Space Research. OSCAR third degree resolution ocean surface currents. Ver. 1. PO.DAAC, 2009.

[4] Ocean Energy System. Annual Report 2014. Technical report, Paris, 2014.

[5] S.E. Ben Elghali, M.E.H. Benbouzid, and J.F. Charpentier. Marine tidal current electric power generation technology: State of the art and current status. *Proceedings of IEEE International Electric Machines and Drives Conference, IEMDC 2007*, 2:1407–1412, 2007.

[6] P Osborne. Electricity from The Sea. *Fujita research report*, 1998.

[7] Christopher J Crossland, Dan Baird, Jean-Paul Ducrotoy, Han Lindeboom, Robert W Buddemeier, William C Dennison, Bruce A Maxwell, Stephen V Smith, and Dennis P

Swaney. *The Coastal Zone — a Domain of Global Interactions*, pages 1–37. Springer Berlin Heidelberg, Berlin, Heidelberg, 2005.

[8] Ma Gregoria Joanne P. Tiquio, Nicolas Marmier, and Patrice Francour. Management frameworks for coastal and marine pollution in the European and South East Asian regions, jan 2017.

[9] M M Lasat. Phytoextraction of metals from contaminated soil: A review of plant/soil/ metal interaction and assessment of pertinent agronomic issues. *Journal of Hazardous Substance Research*, 2(1980):5–25, 2003.

[10] a Gaur and a Adholeya. Prospects of arbuscular mycorrhizal fungi in phytoremediation of heavy metal contaminated soils. *Current Science*, 86(4):528–534, 2004.

[11] E. Pehlivan, A.M. Özkan, S. Dinç, and S. Parlayici. Adsorption of Cu2+and Pb2+ ion on dolomite powder. *Journal of Hazardous Materials*, 167(1-3), 2009.

[12] Coral Vita. Coral Vita: Reef Restoration Solutions, 2014.

[13] Sébastien Roy, Suzanne Labelle, Punita Mehta, Anca Mihoc, Nathalie Fortin, Claude Masson, René Leblanc, Guy Châteauneuf, Christine Sura, Christine Gallipeau, Caroline Olsen, Serge Delisle, Michel Labrecque, and Charles W. Greer. Phytoremediation of heavy metal and PAH-contaminated brownfield sites. *Plant and Soil*, 272(1-2):277–290, 2005.

[14] Yasuhito Miyata, Akio Hayashi, Michihiro Kuwayama, Tamiji Yamamoto, and Norito Urabe. Reduction test of hydrogen sulfide in silty sediment of fukuyama inner harbor using steelmaking slag. *ISIJ International*, 55(12):2686–2693, 2015.

[15] C. J. Sindermann. Pollution effects on fisheries - potential management activities. *Helgoländer Meeresuntersuchungen*, 33(1-4):674–686, 1980.

[16] Andrés Miguel Aguirre-mendoza, Claudia Díaz-mendoza, and Jorgelina Pasqualino. Renewable energy potential analysis in non-interconnected islands. Case study: Isla Grande, Corales del Rosario Archipelago, Colombia. *Ecological Engineering*, (August):0–1, sep 2017.

[17] Uwe Zajonz, Edouard Lavergne, Rebecca Klaus, Friedhelm Krupp, Moteah Sheikh Aideed, and Fouad Naseeb Saeed. The coastal fishes and fisheries of the Socotra Archipelago, Yemen. *Marine Pollution Bulletin*, 105(2):660–675, apr 2016.

[18] Yvonne Sawall, Jamaluddin Jompa, Magdalena Litaay, Andi Maddusila, and Claudio Richter. Coral recruitment and potential recovery of eutrophied and blast fishing impacted reefs in Spermonde Archipelago, Indonesia. *Marine Pollution Bulletin*, 74(1):374–382, sep 2013.

[19] Food and Agriculture Organization of the United Nations. FAO Global Capture Production Database. Technical report, United Nations, 2015.

[20] M. H. Hasan, T. M.I. Mahlia, and Hadi Nur. A review on energy scenario and sustainable energy in Indonesia, 2012.

[21] L.S. S. Blunden, A.S. S. Bahaj, and N.S. S. Aziz. Tidal current power for Indonesia? An initial resource estimation for the Alas Strait. *Renewable Energy*, 49:137–142, jan 2013.

[22] Noir P. Purba, Jaya Kelvin, Rona Sandro, Syahrir Gibran, Resti A.I. Permata, Fatimah Maulida, and Marine K. Martasuganda. Suitable Locations of Ocean Renewable Energy (ORE) in Indonesia Region? GIS Approached. *Energy Procedia*, 65:230–238, 2015.

[23] Deger Saygin Dolf Gielen and Jasper Rigter. Renewable Energy prospects: Indonesia. Technical Report March, 2017.

[24] Yudi N. Ihsan, Armyanda Tussadiah, Niomi Pridina, Rizky M. Utamy, Karina M. Astriandhita, and Kartika Nurhasanah. Renewable Energy from Ocean Currents on the Outflow ITF Pathway, Indonesia. *Energy Procedia*, 65:131–139, 2015.

[25] J. Sprintall. Indonesian Throughflow. In *Encyclopedia of Ocean Sciences*, pages 237–243. 2010.

[26] Evan N. Edinger, Jamaluddìn Jompa, Gino V. Limmon, Wisnu Widjatmoko, and Michael J. Risk. Reef degradation and coral biodiversity in Indonesia: Effects of land-

based pollution, destructive fishing practices and changes over time. *Marine Pollution Bulletin*, 36(8):617–630, 1998.

[27] SEPUTARRIAU.CO. Terbukti Buang Limbah Sembarangan, PT Putera Keritang Sawit Dijatuhi Sanksi, 2017.

[28] Noverita Dian Takarina, David R. Browne, and Michael J. Risk. Speciation of heavy metals in coastal sediments of Semarang, Indonesia. *Marine Pollution Bulletin*, 49(9-10):861–868, 2004.

[29] Tokyo Suisan Daigaku., Food and Agriculture Organization of the United Nations., and United Nations Environment Programme. *An assessment of the effects of pollution on fisheries and aquaculture in Japan.* Food and Agriculture Organization of the United Nations, 1976.

[30] Shiho Ichioka, Jun Sasaki, Yuya Yoshimoto, Kenichiro Shimosako, and Shunsuke Kimura. Analysis of sulfide dynamics including outbreak of blue tide in navigation channels and dredged trench of tokyo bay. *Journal of Japan Society of Civil Engineers, Ser. B2 (Coastal Engineering)*, 65(1):1041–1045, 2009.

[31] Maki Hideaki. Deterioration of sedimentary environment and assessment of its impact on benthic fauna in coastal sea close to urbanized area. Technical report, National Institute Environmental Studies, 2013.

[32] Ministry of Land, Infrastructure, Transport and Tourism, Japan. Report of the Transport Policy Council on the Basic Plan of a Future Port Environment Policy. Technical report, Tokyo, 2005.

Chapter 2

Estimation of Tidal Current Energy in Indonesia

2.1 Characteristics of A Focused Site in Indonesia

Indonesia has many archipelagos with complex and long coastlines in Southeast Asia. The total length of the coastal line is 54,556 km[1] and also there are 17,508 islands[2] connecting each other through straits among Pacific ocean, Indian ocean and Indonesian sea. In recent years, to develop the economic corridors under Master Plan for Acceleration and Expansion of Indonesia Economic Development (abbreviated as MP3EI) 2011-2025[3], a large amount of electricity supply is rapidly required using a renewable energy including tidal current as the economic growth is increasing more and more. Seventy percent of the whole Indonesian sea has 160GW in annual tidal current energy[4].

One of the earliest research on tidal current in Indonesia was conducted by Blunden[5] using ocean circulation model. The annual energy was estimated, 640 GWh and the moderate tidal current speed could be about 2m/s in Alas Strait. However, the simulation was run for six days so it could not describe long-term character of tidal current. One more previous work was also investigated at Lombok strait[6] and Makassar strai[7] to evaluate a strong current at those straits. In 2014, Purba in [8] reviewed the potential of utilizing ocean surface current

and wind as energy source of lighthouse at small islands in Indonesia. In 2015, Purba reported on the discovery of current velocity 3m/s at the eastern part of Indonesia by using Geographic Information System (GIS) approach [9]. In other investigation, Ihsan[10] studied the power value of current velocity at five point locations on the outflow of Indonesian Through Flow (ITF)[11] pathway based on INSTANT observation data[12]. However, INSTANT data are limited to certain depth so the study only found the electricity power of 0.12kW and 0.11kW at the northern part of Ombai strait and the eastern part of Lombok strait, respectively. Meanwhile, Orhan[13] assessed the energy potential of tidal current at Larantuka strait, the southern part of Indonesia by using numerical model and estimated 20GWh annual yield. Several researches on ocean circulation in Indonesia have been conducted to investigate characteristics of tidal current using ocean circulation model, satellite data, and Geographic Information Systems (GIS). However, partial study area could not describe complete tidal current energy potential of Indonesia. In this chapter, to harvest tidal current energy from a specific location and to distribute electric resources especially for local community near coastal area, ocean circulation is investigated in not only whole Indonesian area but also a specific local area for installing a suitable tidal current turbine which will be explained in Chapter 3. The magnitude of potential tidal current kinetic energy is also estimated and examined.

2.2 Computational Domains and Conditions

This study employs one of the famous ocean circulation models, Princeton Ocean Model (POM), proposed by Mellor[14]. The vertical coordinate system uses sigma coordinate system expressed by eq.(2.1), while the horizontal grid uses Arakawa C-grid and structured orthogonal coordinates. The governing equations can be written in Cartesian coordinate after conversion to sigma coordinates, σ, as follows:

$$\sigma = \frac{z + \eta}{H + \eta} \tag{2.1}$$

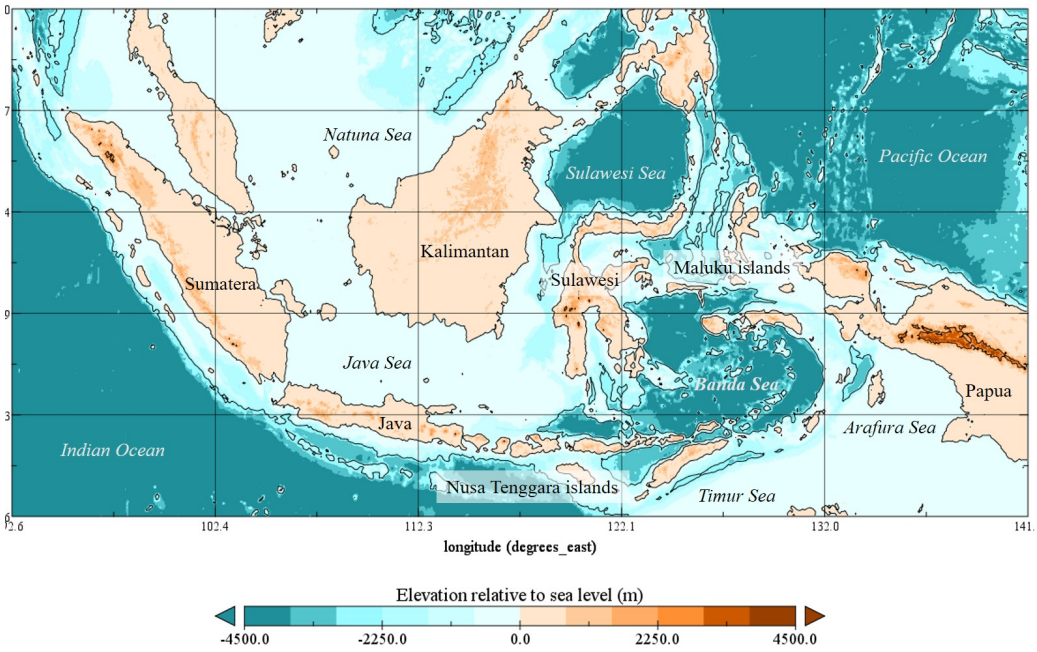

Figure 2.1: Bottom topography in computational domain [15]

$$\frac{\partial DU}{\partial x} + \frac{\partial DV}{\partial y} + \frac{\partial \omega}{\partial \sigma} + \frac{\partial \eta}{\partial t} = 0 \tag{2.2}$$

$$\frac{\partial UD}{\partial t} + \frac{\partial U^2 D}{\partial x} + \frac{\partial UDV}{\partial y} + \frac{\partial U\omega}{\partial \sigma} - fVD + gD\frac{\partial \eta}{\partial x} + \frac{gD^2}{\rho_0}\int_\sigma^0 \left[\frac{\partial \rho'}{\partial x} - \frac{\sigma'}{D}\frac{\partial D}{\partial x}\frac{\partial \rho'}{\partial \sigma'}\right] \partial\sigma' = \frac{\partial}{\partial \sigma}\left[\frac{K_M}{D}\frac{\partial U}{\partial \sigma}\right] + F_x \tag{2.3a}$$

$$\frac{\partial VD}{\partial t} + \frac{\partial V^2 D}{\partial y} + \frac{\partial UDV}{\partial x} + \frac{\partial V\omega}{\partial \sigma} - fUD + gD\frac{\partial \eta}{\partial y} + \frac{gD^2}{\rho_0}\int_\sigma^0 \left[\frac{\partial \rho'}{\partial y} - \frac{\sigma'}{D}\frac{\partial D}{\partial y}\frac{\partial \rho'}{\partial \sigma'}\right] \partial\sigma' = \frac{\partial}{\partial \sigma}\left[\frac{K_M}{D}\frac{\partial V}{\partial \sigma}\right] + F_y \tag{2.3b}$$

where η denotes the surface elevation, H is the bottom topography, D is the summation of H and σ, t is the time, x, y, z are the conventional Cartesian coordinates, and U, V and ω are the velocity components at each direction, f is the Coriolis parameter, ρ_0 is the density, ρ' is the referenced density, σ' is the referenced sigma coordinate, K_M is the vertical kinematic viscosity, F_x and F_y are the diffusivity terms for horizontal and vertical axis respectively, and g is the gravity acceleration.

The bottom topography in whole Indonesian seas is a spatially averaged product of one-minute obtained from Gridded Global Relief Data, ETOPO1[15] as shown in Fig.2.1. The numerical

domain is distributed evenly into $0.05^\circ \times 0.05^\circ$ as the horizontal grid size. The vertical domain from sea bottom to water surface is divided into eight layers in sigma coordinates. The water elevation at boundary conditions for whole Indonesia sea is imposed by the sea level monitoring facilities under Intergovernmental Oceanographic Commission (IOC) program [16]. The tidal current velocity magnitudes and vectors are computed for one month time integration. A run-up period is set to be 48 hours to work well without numerical fluctuation and unstable state. To investigate tidal current energy only, wind force and thermal condition at sea surface are ignored in this study. The time step for external mode in 2D is one second and that for internal mode in quasi-3D is 5 seconds. In this study, we focus on asmall strait such as Bali Strait, and archipelago, such as Maluku islands and Nusa Tenggara islands, where potential of tidal current energy could be relatively higher. Therefore, to investigate a suitable installation site and to evaluate tidal current energy, the nesting technique for sea surface elevation is employed and then the fine grid is used for local region. The minimum grid size is about 200m in horizontal space and ten sigma layers is used in vertical depth.

2.3 Validations

In this section, the numerical results are validated with observation field data in not only whole Indonesian seas but also at a narrow strait. The referred water elevation was obtained by the pressure sensor of the sea level station monitoring facility, IOC as mentioned above. The three monitoring points are selected, Vung Tau (10.34N, 107.071E) , Christmas Islands (10.4294S, 105.6693E) and Malakal (7.3282N, 134.4502E) for validation in whole Indonesia sea. On the other hand, in a local archipelago, Bali strait having the narrowest area, 2.4km, is picked up, where the tidal current data was observed by acoustic tomography technique proposed by Munk et al.[17]. The acoustic tomography technique can construct spatial structures of a current field by measuring sound speed in real sea condition. Especially at coastal region, Coastal Acoustic Tomography (CAT)[18] was proposed and applied to investigate tidal current and ocean environment in shallow water region. In this study, to validate velocity distribution in a local archipelago area, the CAT observation with four acoustic stations was conducted

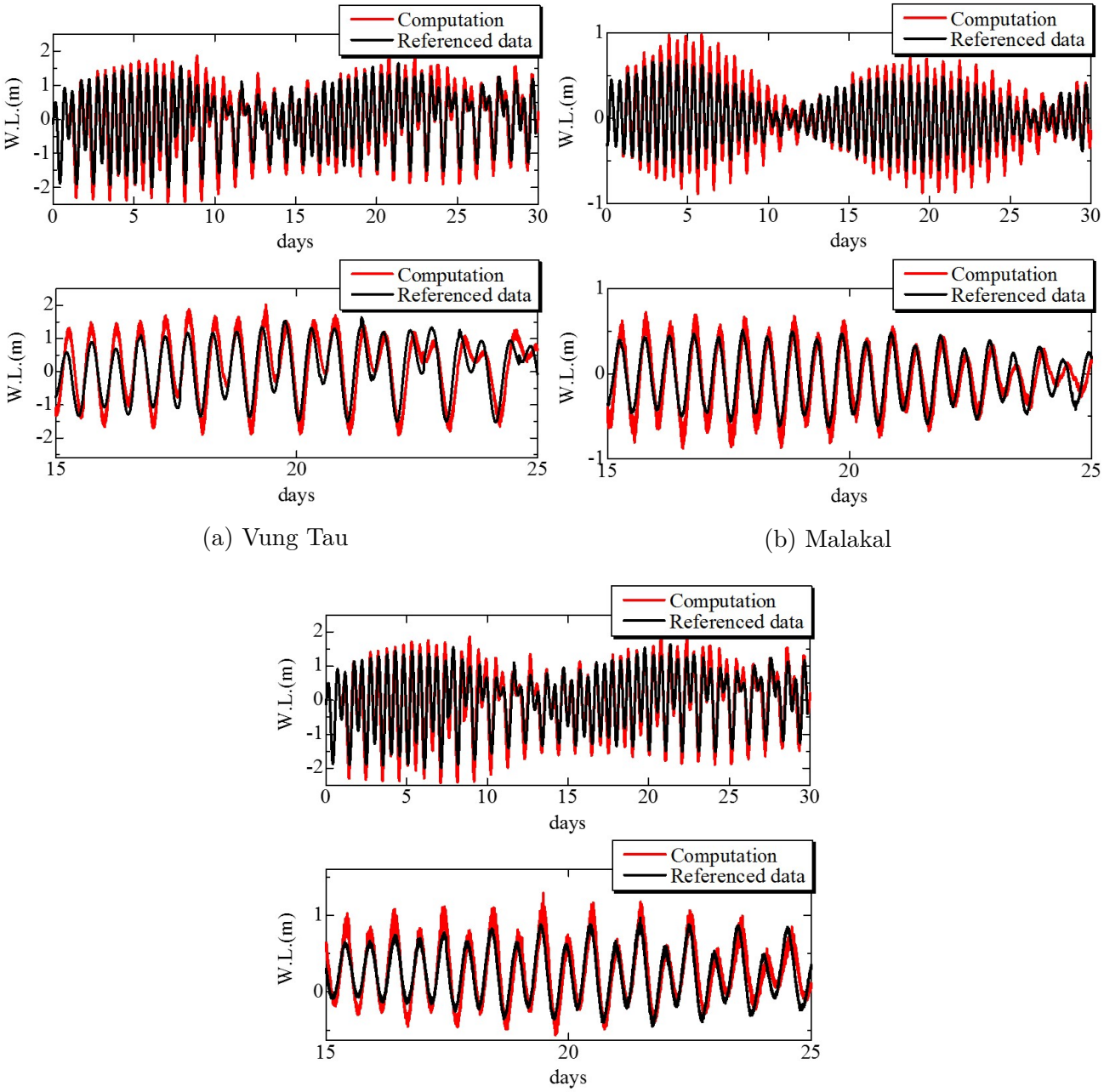

(a) Vung Tau

(b) Malakal

(c) Christmas Islands

Figure 2.2: Comparisons of time histories in sea surface elevation with the observation data, IOC

from 30th May to 5th June in 2016.

Firstly, comparisons of time histories in sea surface elevation at three different locations, Vung Tau, Malakal and Christmas Islands are shown in Fig.2.2. The numerical results are overall agreement with the referenced data, IOC. However there is a little discrepancy in the tide phase at the low tide period and the water elevations are slightly overestimated. The difference is

caused by the implementation of leapfrog advection scheme in this computational model and it should be improved in future effort. The results are reasonable for evaluating tidal current characteristic and potential of energy harvesting. Secondly, the tidal current distributions are compared at two dominant periods, north current time and south current one, with CAT observation data in Bali strait as shown in Fig.2.3. The current velocity on the sound ray between the sound arrays can be measured by CAT system and then the velocity data is usually converted onto the computational grids by the inverse analysis[18]. It can be seen that the maximum current is concentrated at the narrowest region between Bali and Java, where the four sound arrays of CAT system were set to measure the sound speed. The comparisons of tidal current distribution between the computational result and the observed one, are shown in this figure. The tendency of the velocity is overall agreement with observation data but a little difference can be found and the velocity magnitude seems to be slightly stronger, especially at the central region. This is because there is very shallow region near east coastal area at Bari strait and therefore the north-south current is rapidly strengthened at the center region.

Fig.2.4 shows correlation of magnitude of tidal current velocity between the computational results and CAT ones. The regression curve are linearly fitted as shown in this figure. Some of the observed CAT data are larger than the computational ones at the south current case. However the correlation coefficients are relatively high, over 0.9, in both the north and south current cases. The results mean that the computational model is reliable to be used to examine tidal current field even at a narrower region, and to estimate potential of tidal current energy using a designed tidal current turbine.

2.4 Estimation of Tidal Current Energy at Archipelago in Indonesia

Tidal current velocity is necessary to quantify the available energy at a site prior to design a specific tidal current turbine. Fig.2.5 presents the depth-averaged tidal current distribution averaged by one month at a focused archipelago area in the western part of Indonesian sea. It

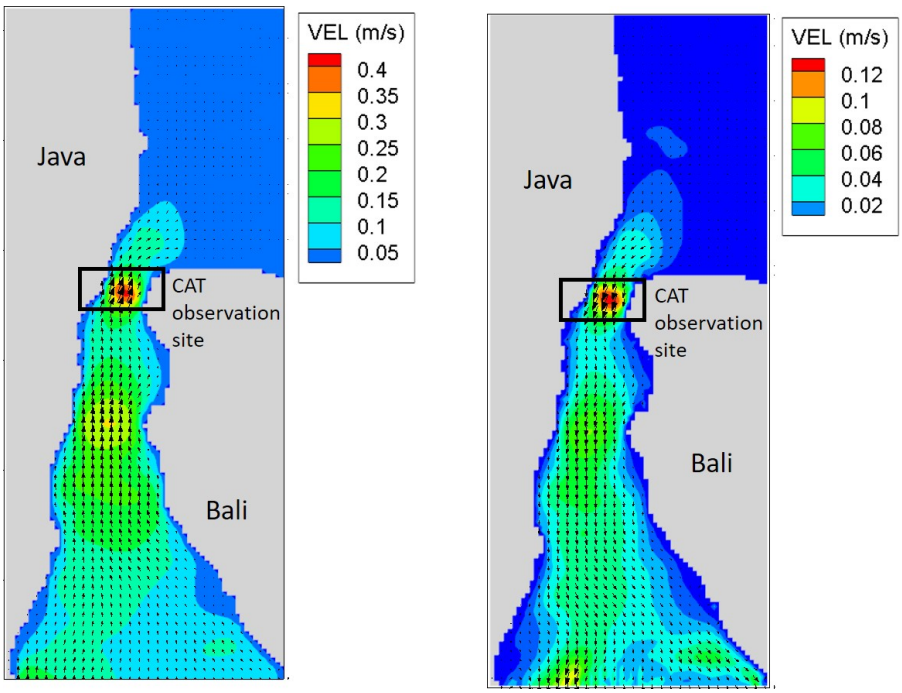

(a) Computational results of velocity field in Bali strait (left: north current, right: south current)

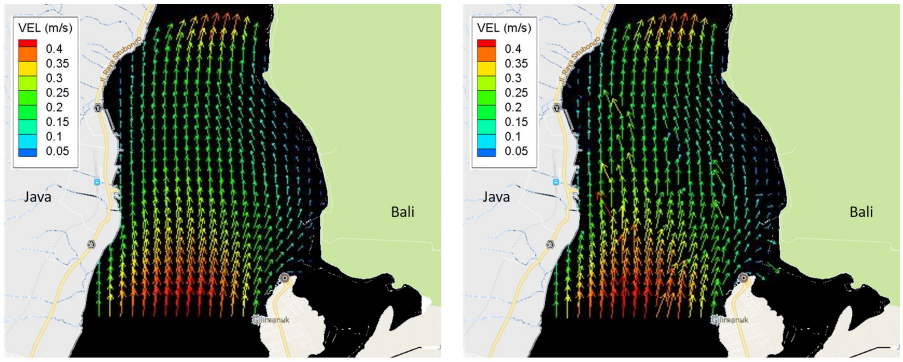

(b) North current (left: computation by POM, right: observation by CAT indicated by black square in (a))

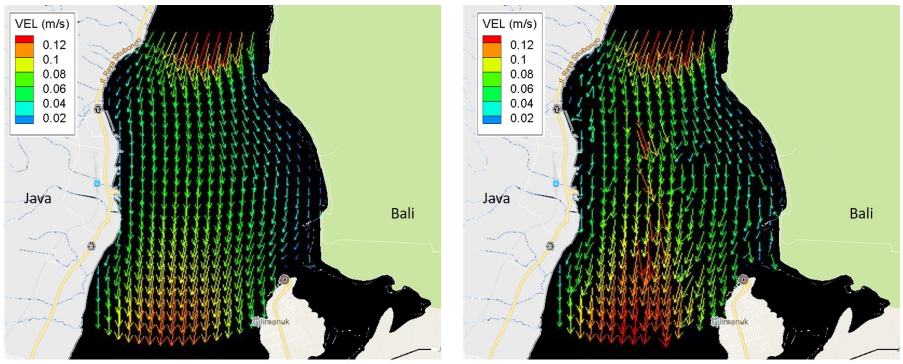

(c) South current (left: computation by POM, right: observation by CAT indicated by black square in (a))

Figure 2.3: Comparisons of tidal current distribution in Bali Strait

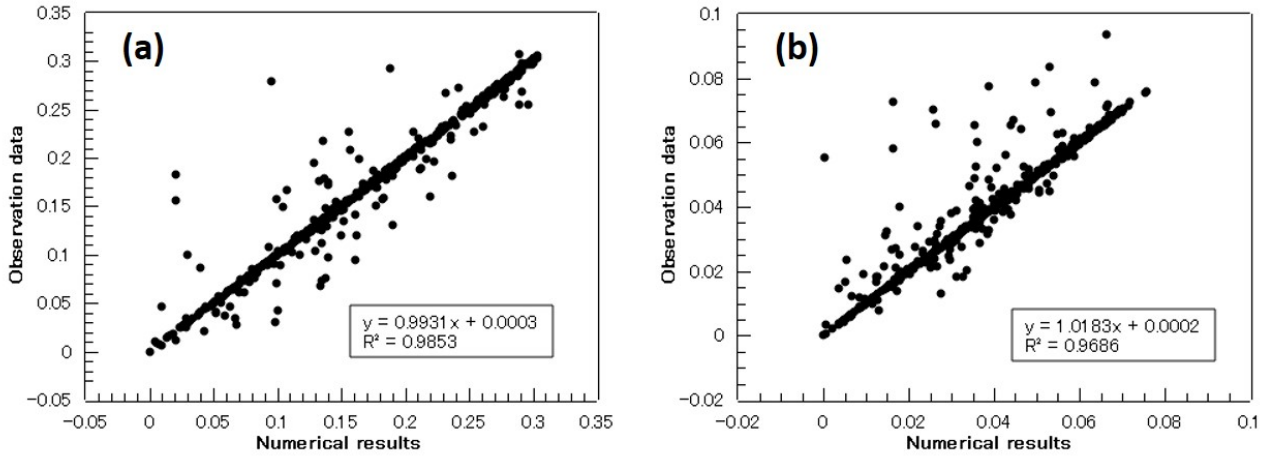

Figure 2.4: Correlation of tidal current between computational results and CAT field data in Bali Strait (left: north current, right: south current)

can be seen that the tidal current at narrow straits is relatively high at archipelago area such as Maluku islands and Nusa Tenggara islands including Bali strait. In particular, at Halmahera Island in Maluku islands, high density of strong tidal current can be found at the northern part and the western one. The west coat of Halmahera Island has the shallower region from 200m to 500m, which would be suitable for installing a tidal current turbine. Meanwhile, Nusa Tenggara islands model is covering from Bali Island at the west side to Alor islands at the east side, where Lombok Strait is the most notable location with the maximum tidal current velocity, 4m/s. The water depth varies from less than 100m near the coastal area to 1.3km at the edge of north side of Nusa Tenggara islands. The Lombok Strait also has a fairly cold water temperature at less than 200m depth, that is about 20°C as investigated by Fieux et al.[19]. Some accidents for aquaculture are sometimes occurred by upwelling of cold water at Lombok Strait.

Figs.2.6 and 2.7 focus on archipelago region in more detail in order to investigate depth-averaged tidal current distribution and to find a hot spot of tidal current energy ($P = 0.5\rho AV^3$, where ρ is the density of sea water, V is the velocity component and A is the projected unit area related to water depth). In Fig.2.6, it can be found that the highest velocity is reached, 2.4 m/s, especially at the narrower strait in the northern and the southern part of Halmahera Island and the resultant tidal current kinetic power could produce about 5kW/m^2. Fig.2.7 suggests that the narrow straits at Nusa Tenggara islands including Lombok Strait, Alas Strait, Sape Strait,

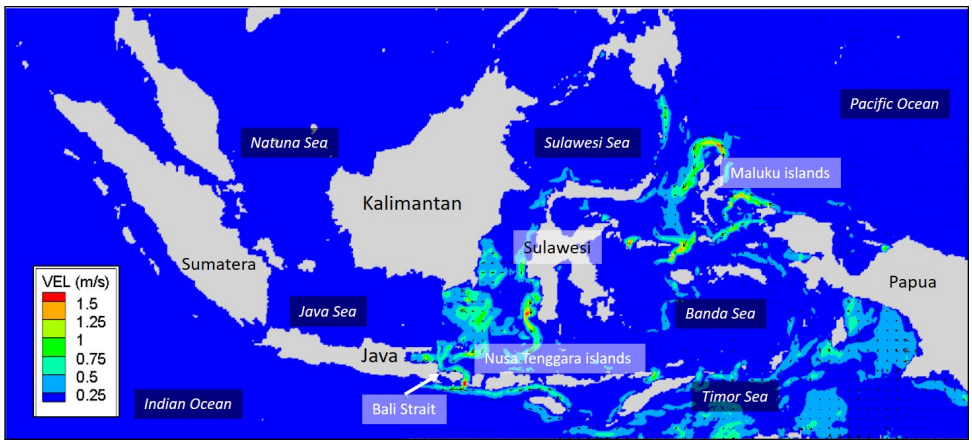

Figure 2.5: Depth-averaged tidal current distribution in whole Indonesian sea

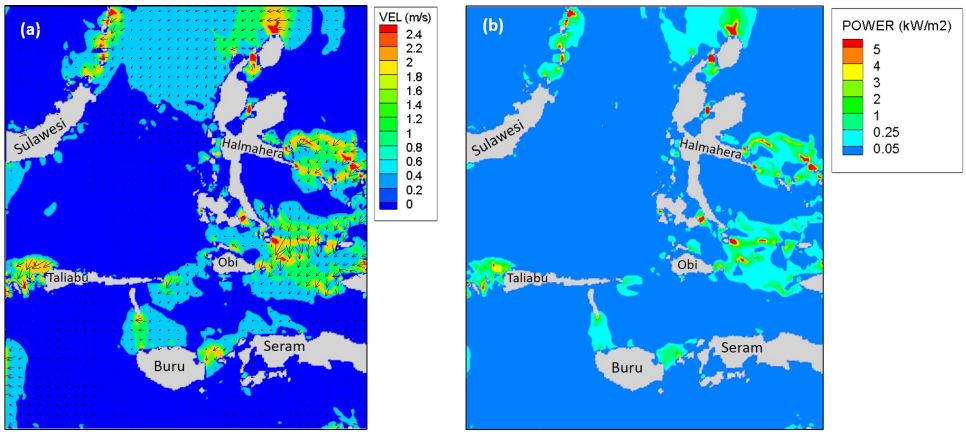

Figure 2.6: Depth-averaged tidal current velocity and energy distribution in Maluku islands

and smaller straits at Alor islands, can produce more than 2.8m/s for tidal current and more than 12kW/m^2 for tidal current energy. The estimated tidal current kinetic power is consistent with the previous report by Orhan[13] who estimates more than 6kW/m^2 at Larantuka strait located at Alor islands. In this model, the maximum tidal current is estimated, over 4m/s at Lombok Strait. Most of the above mentioned sites have relatively shallower region at the archipelago where it is easier to install and maintain a specific tidal current turbine and to set up energy supply for local people living at a small island.

In general, there are two types of tidal current turbine, horizontal axis turbine (HAT) and vertical axis turbine (VAT). HAT type is suitable at one direction flow and its effective to harvest high velocity flow. Otherwise, VAT type can handle multi-direction flow and also drag-type of VAT can be operated even if tidal current is relatively low. To decide a suitable type of tidal current turbine and design it, a flow direction and dominant velocity should be carefully

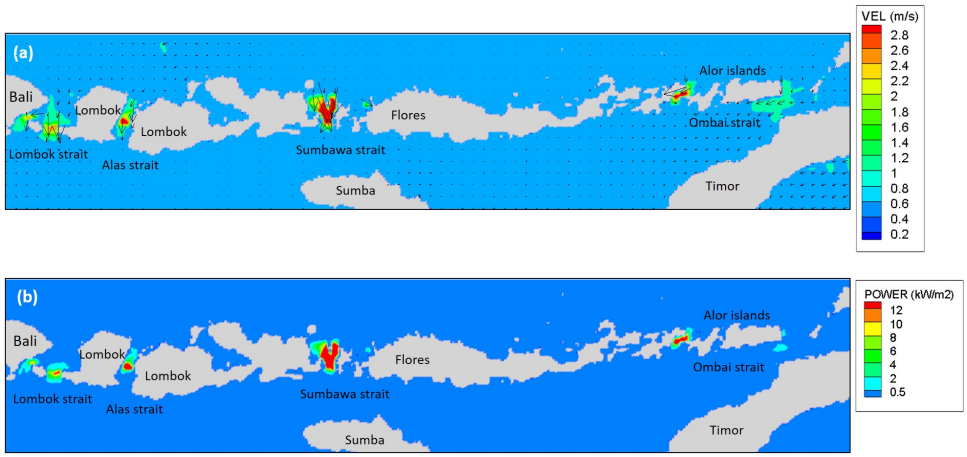

Figure 2.7: Depth-averaged tidal current velocity and energy distribution in Nusa Tenggara islands

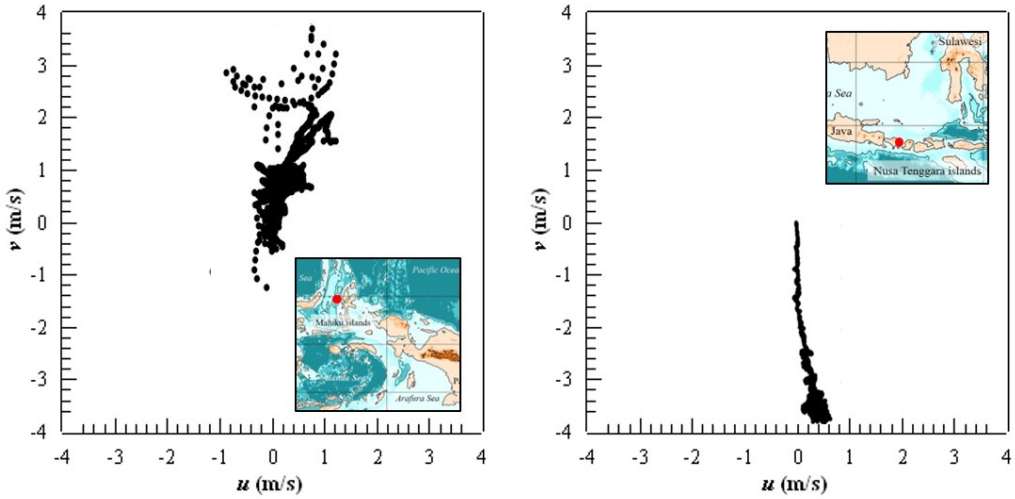

(a) Maluku Sea (b) Lombok Strait

Figure 2.8: Characteristics of flow direction on Hodograph

examined at archipelago region where potential energy due to tidal current is so high. This section focuses on two sites, Maluku Sea and Lombok Strait (Nusa Tenggara islands), where the tidal current is relatively strong, about 4m/s estimated by the previous results and also the electric demand is rapidly increasing for local people.

Fig.2.8 shows characteristics of flow direction at Maluku Sea and Lombok Strait (Nusa Tenggara islands) illustrated by the map. This figure indicates the dominant flow, u at east-west direction and v at north-south direction, during one month period, where positive value for u and v indicates east and north directions, respectively. It can be found that the tendency of tidal current at Lombok Strait is almost south direction but there is no flow at east-west direction

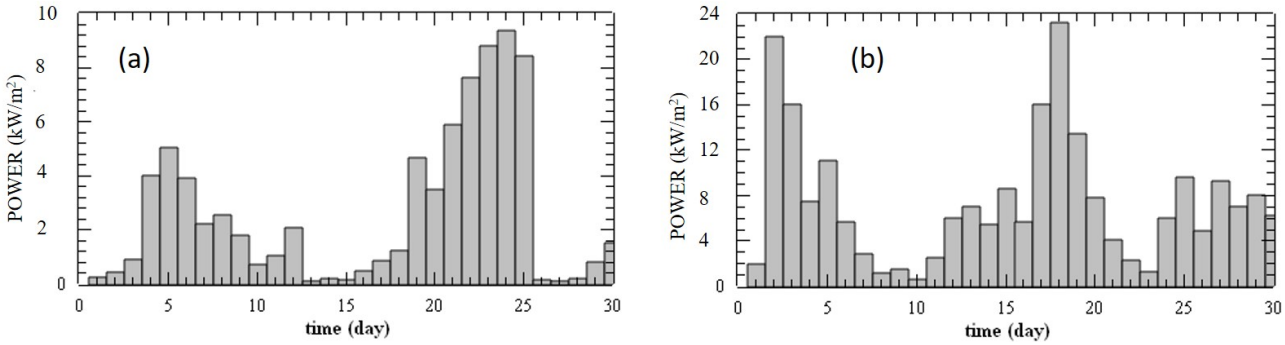

(a) Maluku Sea (b)Lombok Strait

Figure 2.9: Time Variation of tidal current power during one month

because this strait is quite narrow between Bali Island and Lombok Island as shown in Fig.2.7. Whereas, in Maluku Sea, the dominant flow is also north direction but some of them are fluctuated at east-west direction for a certain period. This is because the tidal current can be flowed along the west coast of Halmahera Island but the western part of this site is open sea, which is not strait between islands.

Fig.2.9 shows time variation of tidal current power for one month at Maluku Sea and Lombok Strait. The tidal current at Maluku Sea is mostly affected by the flow features at the northern part of Indonesian seas. The tidal current kinetic power is stronger at the first and third weeks, which depends on neap and spring tides but the average power for one month is about 4kW/m^2. As for Lombok Strait, it is also affected by the tide period at the southern part of Indonesian seas and the average one is about 8kW/m^2.

Furthermore, full-three-dimension model using the Autodesk CFD 2016 is subjected to Lombok strait to understand the tidal current distribution in more detail. Lombok strait divides Bali from Lombok islands and it is 59 km in length, at the north-south direction. The width of the strait varies from 36 km at its north-sill, 70 km at the mid-channel, to 16 km at the south-sill, while the depth varies from less than 100m in coastal areas to 1.3 km in the edge of north-sill as shown in Fig.2.10. The horizontal domain's total grid is 5,143 divided into 1.7 km grid size, while the vertically contour interval is 100 m. By referring to the previous ocean model at Nusa Tenggara islands, the flow from north boundary to the south one is more dominant than the opposite direction, likewise the flow in CFD model can be applied in the same way. By

applying the maximum velocity of 1.2 m/s in the north boundary as the inlet and zero pressure at the south boundary as the outlet, the flow inside Lombok Strait can be estimated as shown in Fig.2.11. The strongest flow is passing the coastal areas at the narrowest part of the southern part of the strait. The mean velocity is 3 m/s and the maximum one is estimated, about 5 m/s at the localized point. Such rapid flows are consistent with earlier reports of strong currents with a magnitude of 3.5 m/s (Murray and Arief, 1988) recorded between the islands of Nusa Penida and Lombok. The ideal installation site near the shore at the water depth 100 to 200m can be selected.

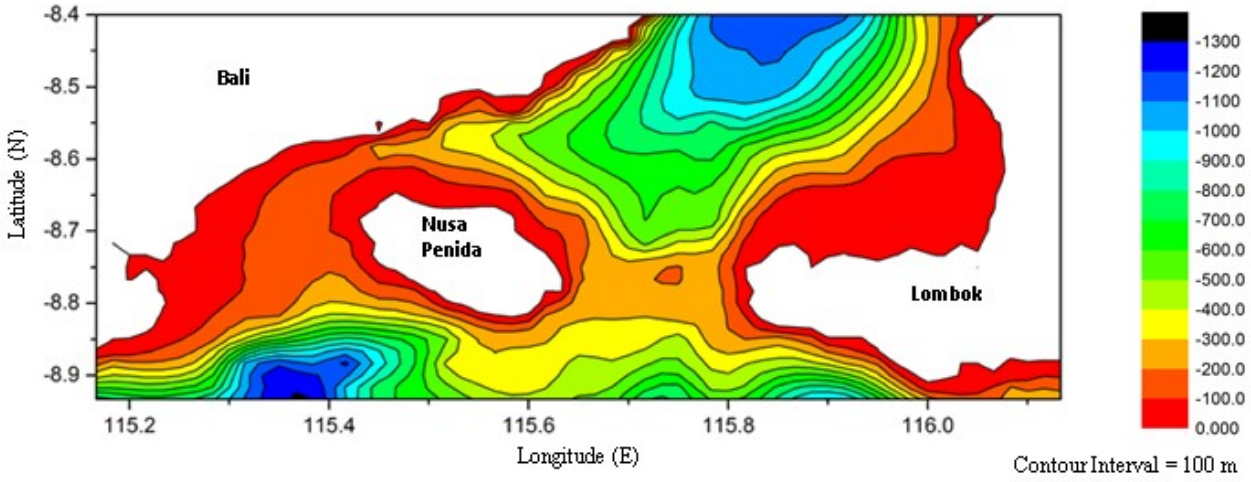

Figure 2.10: Bottom topography at Lombok Strait

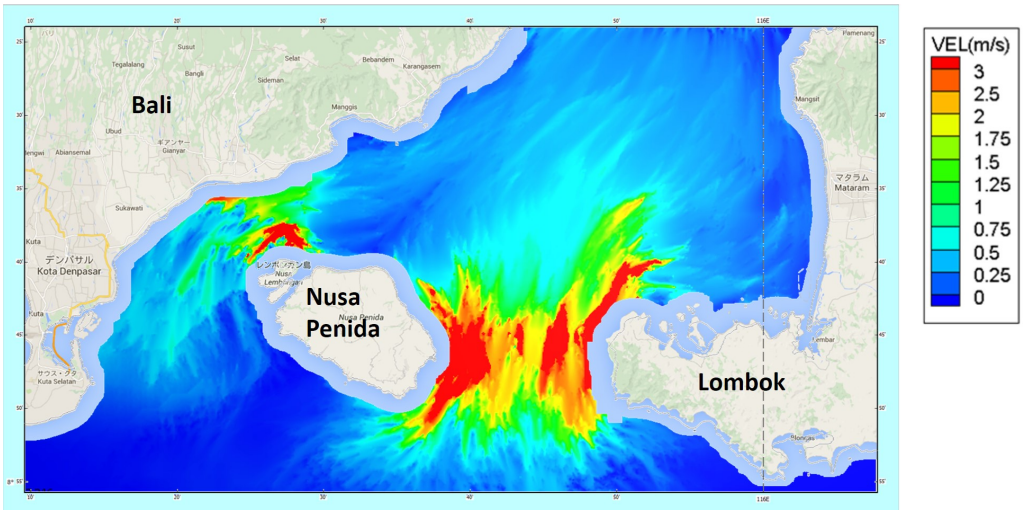

Figure 2.11: Detailed velocity distribution at Lombok Strait

2.5 Conclusions

This study investigated characteristics of tidal current at archipelago in Indonesia. The main conclusions can be summarized as follows. The tidal current at the narrow straits is relatively high at the archipelago area such as Maluku islands and Nusa Tenggara islands including Bali strait. In particular, Lombok strait is the most notable location with the maximum tidal current velocity, 4m/s. The narrow straits at Nusa Tenggara islands can produce more than 2.8m/s for tidal current and more than 12kW/m^2 for tidal current energy. In the northern and the southern part of Halmahera island, the resultant tidal current kinetic power also produces about 5kW/m^2. The tendency of tidal current at Lombok strait and Maluku sea is almost south direction and therefore a small sized Horizontal Axis Turbine (HAT) is appropriate for the flow conditions to generate electric power with high efficiency to avoid ocean environmental damages caused by installing and operating HAT and to suitably supply electric power with low transmission cost to local living people.

Bibliography

[1] Florence Lamoureux. *Indonesia : a global studies handbook*. ABC-Clio, Santa Barbara Calif. [u.a.], 2003.

[2] William Hung Kan Lee, Hiroo Kanamori, Paul Jennings, and Carl Kisslinger. *International Handbook of Earthquake and Engineering Seismology*, volume 81 of *International Geophysics*. Elsevier, 2003.

[3] Republic of Indonesia Coordinating Ministry For Economic. *Master Plan for Acceleration and Expansion of Indonesia Economic Development (MP3EI) 2011-2025*. Coordinating Ministry for Economic Affairs, Republic of Indonesia, Jakarta, 2011.

[4] Mary Ann Joy Robles Quirapas, Htet Lin, Michael Lochinvar Sim Abundo, Sahara Brahim, and Diane Santos. Ocean renewable energy in Southeast Asia: A review. *Renewable and Sustainable Energy Reviews*, 41:799–817, jan 2015.

[5] L.S. S. Blunden, A.S. S. Bahaj, and N.S. S. Aziz. Tidal current power for Indonesia? An initial resource estimation for the Alas Strait. *Renewable Energy*, 49:137–142, jan 2013.

[6] J. P. Matthews and T. Awaji. Synoptic mapping of internal-wave motions and surface currents near the Lombok Strait using the Along-Track Stereo Sun Glitter technique. *Remote Sensing of Environment*, 114:1765–1776, 2010.

[7] A. L. Gordon, R. D. Susanto, A. Ffield, B. A. Huber, W. Pranowo, and S. Wirasantosa. Makassar Strait throughflow, 2004 to 2006. *Geophysical Research Letters*, 35(24), 2008.

[8] NP Purba, Jaya Kelvin, Muallimah Annisaa, and Dessy Teliandi. Preliminary Research of Using Ocean Currents and Wind Energy to Support Lighthouse in Small Island, Indonesia. *Energy Procedia*, 47:204–210, 2014.

[9] Noir P. Purba, Jaya Kelvin, Rona Sandro, Syahrir Gibran, Resti A.I. Permata, Fatimah Maulida, and Marine K. Martasuganda. Suitable Locations of Ocean Renewable Energy (ORE) in Indonesia Region ? GIS Approached. *Energy Procedia*, 65:230–238, 2015.

[10] Yudi N. Ihsan, Armyanda Tussadiah, Niomi Pridina, Rizky M. Utamy, Karina M. Astriandhita, and Kartika Nurhasanah. Renewable Energy from Ocean Currents on the Outflow ITF Pathway, Indonesia. *Energy Procedia*, 65:131–139, 2015.

[11] J. Sprintall. Indonesian Throughflow. In *Encyclopedia of Ocean Sciences*, pages 237–243. 2010.

[12] Arnold L. Gordon, J. Sprintall, H. M. Van Aken, D. Susanto, S. Wijffels, R. Molcard, A. Ffield, W. Pranowo, and S. Wirasantosa. The Indonesian throughflow during 2004-2006 as observed by the INSTANT program. *Dynamics of Atmospheres and Oceans*, 50(2):115–128, 2010.

[13] Kadir Orhan, Roberto Mayerle, and Wahyu Widodo Pandoe. Assesment of Energy Production Potential from Tidal Stream Currents in Indonesia. *Energy Procedia*, 76:7–16, 2015.

[14] George L Mellor. *Users guide for a three-dimensional, primitive equation, numerical ocean model*, volume 8544. 2002.

[15] C Amante and B.W. Eakins. ETOPO1 1 Arc-Minute Global Relief Model: Procedures, Data Sources and Analysis. *NOAA Technical Memorandum NESDIS NGDC-24*, (March):19, 2009.

[16] National Coordinating Agency for Surveys and Mapping (BAKOSURTANAL). Seal Level Station Monitoring Facility from Global Sea Level Observing System program. Intergovernmental Oceanograpchic Commission of UNESCO, 2016.

[17] W. Munk and C. Wunsch. Ocean acoustic tomography: A scheme for large scale monitoring. *Deep-Sea Res.*, 26A:123–161, 2003.

[18] J.-H. Park and A. Kaneko. Assimilation of coastal acoustic tomography data into a barotropic ocean model. *Geophys. Res. Lett.*, 27(20):3373–3376, 2000.

[19] M. Fieux, C. Andrié, P. Delecluse, A.G. Ilahude, A. Kartavtseff, F. Mantisi, R. Molcard, and J.C. Swallow. Measurements within the Pacific-Indian oceans throughflow region. *Deep Sea Research Part I: Oceanographic Research Papers*, 41(7):1091–1130, jul 1994.

Chapter 3

Design of Small-sized Tidal-current Turbine for Archipelago in Indonesia

In this chapter, a small-sized tidal-current turbine is theoretically and numerically designed and optimized considering the specific tidal-current at the archipelago areas. The hydrodynamic responses are also examined, such as velocity field and pressure distribution are examined.

Considering the tendency of the tidal-current at the focusing archipelago, Maluku Sea and Lombok Strait, Horizontal Axis Turbine (HAT) is appropriate for the flow conditions to generate electric power with high efficiency. Because the unidirectional flow is dominant in Maluku Sea and Lombok Strait, turbine blade can be easily controlled to operate perpendicularly to tidal-current flow direction, in order to maximize the harvested power. To avoid ocean environmental damages caused by installing and operating HAT and to suitably supply electric power with low transmission cost to local people living there, a small-sized HAT with the diameter range 1 to 3m should be selected and designed for these sites.

In this chapter, a small-sized HAT is theoretically designed by the open source code, QBlade[1] based on Blade Element Momentum (BEM) theory, which can calculate important parameters such as lift force coefficient C_L, drag force coefficient C_D at several angles of attack with different Reynolds number. Qblade can also estimate performance of electric power generation of a turbine at a certain rotational speed.

3.1 Selection of Suitable Hydrofoil

Generally speaking, hydrofoils are developed for a certain families which have similar features but can vary in aspects such as chord length and thickness ratio. Ratio of lift force L to drag force D, that is lift-drag ratio L/D, should be relatively higher in order to realize electric performance with high efficiency and hydrodynamic one. On the other hand, rotating turbine blade needs to have enough strength to comply with hydrodynamic load due to tidal-current flow. NREL S814 hydrofoil is one of the most commonly used hydrofoil to design a turbine which can harvest tidal current with high efficiency [2]. Previous researches [3] has also found that with its 24% chord thickness, NREL S814 can survive rough environment conditions. Therefore, in this study, NREL, S814 hydrofoil is selected as the baseline blade of HAT and is optimized for archipelago in Indonesia.

First step to design a turbine is by analyzing the hydrofoil that used as baseline blade. NREL S814 is theoretically analyzed by the open source code, QBlade[1] based on Blade Element Momentum (BEM) theory. By calculating each hydrofoil as the local part of a blade, QBlade can calculate important parameters such as lift force coefficient C_L, drag force coefficient C_D at several angles of attack with different Reynolds number.

Angle of attack (AoA) α is the angle between the chordline of airfoil and the relative windspeed experienced by the hydofoil can be expressed as below,

$$\alpha = \theta - \Phi \tag{3.1}$$

where $\phi = \phi_p + \beta$ is a combination of the pitch angle ϕ_p and the twist angle β. From these information, the lift and drag coefficients of the hydrofoil can be obtained from the experiment table and the lift and drag caused by the hydrofoil can be calculated. Characteristic of the desired hydrofoil is higher lift coefficient (C_L) over the drag coefficient (C_D).

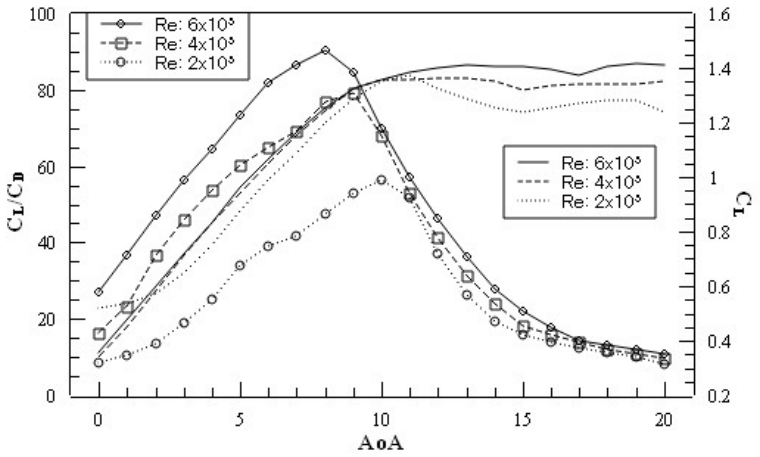

Figure 3.1: Characteristics of lift-drag ratio C_L/C_D and lift force coefficient C_L versus angle of attack (AoA) for NREL S814 hydrofoil at different Reynolds number.

Fig.3.1 shows hydrodynamic performance of the baseline blade, NREL S814 hydrofoil under the different Reynolds number, Re=2×10^5, 4×10^5 and 6×10^5 at different current speed, 1, 2 and 3 m/s, respectively. The current speed can be selected considering the dominant tidal-current at the focusing area, Maluku sea and Lombok strait, found in Sec.2. In order to keep lower drag coefficient, the maximum lift-drag ratio C_L/C_D needs to be considered by keeping angle of attack AoA without fluctuation. At this condition, C_L is not maximum value, but it is still considerably high. For the design of tidal-current turbine of NREL, the baseline blade, S814 hydrofoil with $AoA = 8°$, $C_L = 1.256$ and $C_L/C_D = 90.5$, is selected for the focusing archipelago. Fig.3.2 shows the baseline blade, NREL S814 hydrofoil at AoA 9° subjected by the uniform water flow with 3m/s. The velocity and pressure distributions are also presented. At these conditions, cavitation phenomena cannot be formed and the safety of hydrofoil should be also considered for designing a tidal-current turbine. NREL S814 hydrofoil has 24% chord thickness and 3% camber thickness.

3.2 Small-sized Turbine Design and Its Optimization

By applying the baseline blade, NREL S814 hydrofoil with the high lift coefficient and the lift-drag ratio, a Horizontal Axis Turbine (HAT), with 2.2 diameter, generating electric power 10 kW class can be designed and installed at the focusing area, archipelago island, as shown in

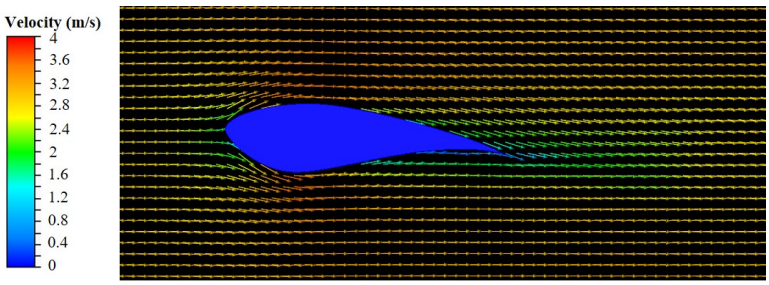

(a) velocity distribution

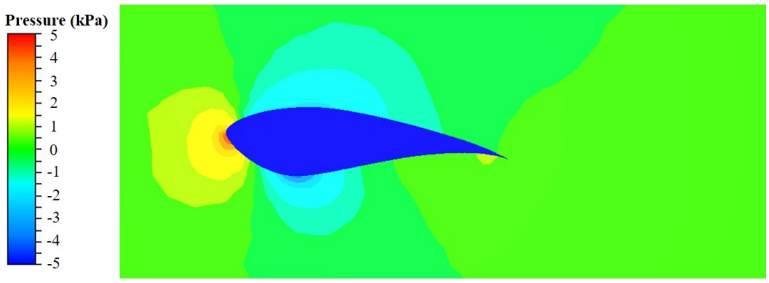

(b) pressure distribution

Figure 3.2: Characteristics of velocity and pressure fields around NREL S814 hydrofoil at *AoA* 8° and water velocity 3m/s

Sec.2. The chord length of the present blade is relatively shorter than that of a typical HAT blade. In this study, to increase the solidity of swept area, three blades turbine are selected. Three-bladed turbine is more stable and does not cause much vibration, thus increase operating life, and reduce fatigue failures [4]. Moreover, three-bladed turbine has lower TSR than two-bladed ones and this reduces the chance of cavitation inception [5]. The principal parameters for the designed blade are specified in Table 3.1.

Each blade is one m long and the hub with the connection to the blade is 0.2m. The rated ocean current velocity is 3m/s, the cut in velocity is 1 m/s, and the cut off velocity is 5m/s. For maximum rotor efficiency, the blade twist and chord distribution needs to be optimized, by considering characteristics of the tidal-current found at the archipelago as shown in Chapter 2. Blade Element Momentum (BEM) theory can be adopted to keep track of theoretical efficiency while optimizing the twist and chord distribution to obtain the best theoretical performance. The baseline blade performance can be optimized to realize the maximum lift-drag ratio C_L/C_D at each chord by applying twist and Schmitz's chord optimization [6] as shown in Fig.3.3. The baseline blade, NREL S814 hydrofoil is employed for the total length of the designed rotor blade. Near the root section of the blade, the cylindrical foil is applied to strengthen the joint

Table 3.1: Principal parameters for the designed blade

Design parameters	Values
Diameter (D)	2.2 m
Estimated power coefficient (C_P)	0.4
Number of blades (N)	3
Rotational speed (n)	75 rpm
Designed tidal-current velocity (v_{rated})	3.0 m/s
Estimated power (P_{rated})	10 kW
Tip Speed Ratio (TSR)	4

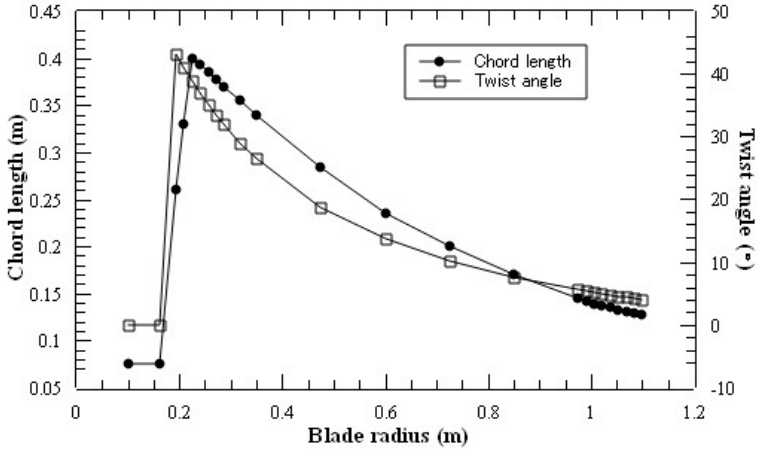

Figure 3.3: Optimization of chord length and twist angle with blade radius

part of the blade connecting with a boss as seen in Fig.3.4.

3.3 Hydrodynamic Performance of The Designed Turbine

In the previous sections, the designed blade was optimized with Prandtl tip and root loss [7] by using QBlade[1] based on Blade Element Momentum (BEM) theory. However viscosity and turbulence should be considered to accurately estimate electric power performance of the designed turbine in Sec.3.2. In this section, Computational Fluid Dynamic (CFD) analysis with incompressible and viscous fluid is carried out in the design condition explained in Sec.2. The numerical simulation is conducted by the commercial software, Autodesk CFD. The governing equations are continuum equation and Navier-stokes equations with turbulent model. For the advection scheme, Modified Petrov-Galerkin is employed to work well on large external flow

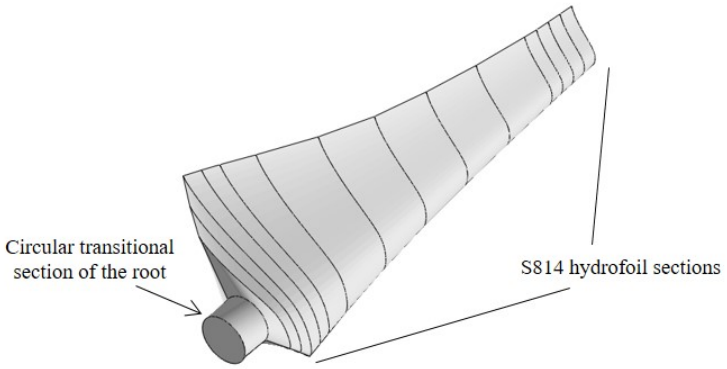

Figure 3.4: Bird's eye view of 10 kW HAT rotor blade designed for archipelago area

domain. For a rotating turbine, the shear stress transport (SST) k-omega is used as a turbulence model in order to accurately reproduce flow separation and vortex occurring on complicated blade surface as shown in [8].

Figs.3.5 and 3.6 are the tetrahedral grid generation on the designed blade and the computational domain including the rotating region by using an overset grid system, respectively. Table 3.2 also shows computational conditions of CFD simulations. The total grid number in the model is about 1.6×10^4. The length between the inlet and outlet boundaries is set to $10R$, where R is the blade radius. The square boundary with $5R$ is imposed at the upstream and downstream sides. The inflow is a constant velocity, 3m/s, with 10% turbulent intensity to be the current conditions. The temperature of sea water is assumed to be 20°C for viscosity and density conditions. The rotational speed is 75rpm for the designed condition in the focusing area. The pressure distribution on the designed blade in the rotational region can be obtained at the tetrahedral grid. If necessary, the structural analysis can be performed then by using Finite Element Method (FEM) in order to evaluate structural strain and stress. Fig.3.7 shows streamline field around the rotational rotor blade and the instantaneous pressure distribution on the surface of the designed blade at the upstream and downstream sides. The torque of the designed blade is also estimated as shown in Fig. 3.8. The streamline around the designed blade is smoothly distributed from the upstream side to downstream one. The maximum pressure on the blade is found at the leading edge of the blade and the largest pressure is generated at the tip of the blade but there is no localized pressure and the strength of blade material would be enough for the design manual in practical use.

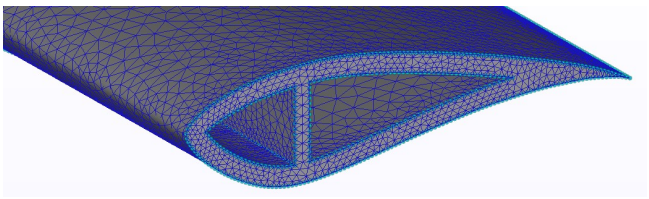

Figure 3.5: Tetrahedral grid generation on the designed blade

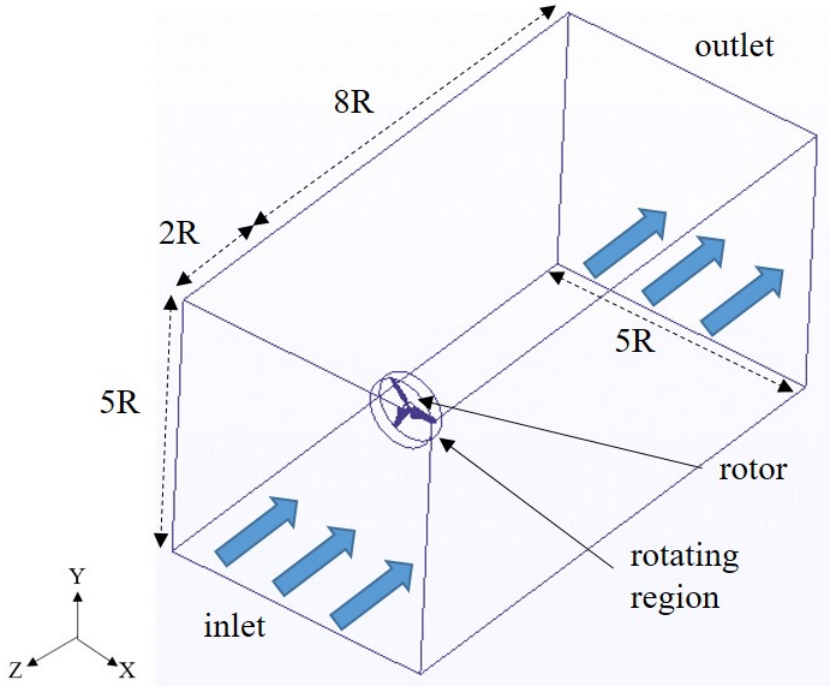

Figure 3.6: Computational domain and boundary conditions

3.4 Estimation of Electric Power at Archipelago of Indonesia

The power coefficient curve for the designed rotor blade can be calculated by $C_P = \tau\omega/0.5\rho AV^3$, where τ is the torque, ω is the angular velocity. The electric performance of the optimized turbine with tip speed ratio (TSR) can be estimated as shown in Fig.3.9. The maximum power coefficient reaches about 0.43 at TSR=3.75, which is slightly lower than the designed TSR, 4 as investigated in Sec3.3. This means that the electric performance of the turbine blade is higher than that one estimated by the designed turbine at lower current condition. Moreover the power coefficient is greater than 0.4 at TSR=3.0∼4.5. This suggests that the designed turbine could operate with good performance over a wide range of tidal-current condition at

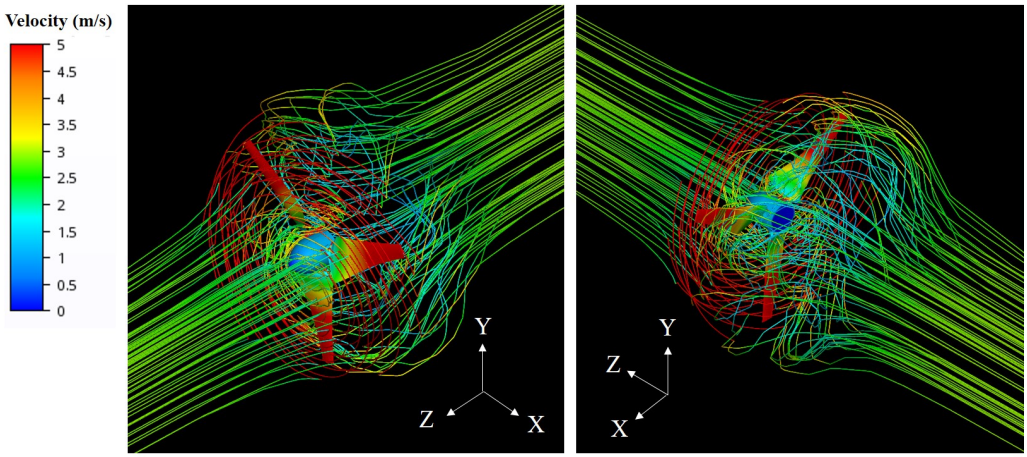

(a) Streamline around rotational blade in 3D

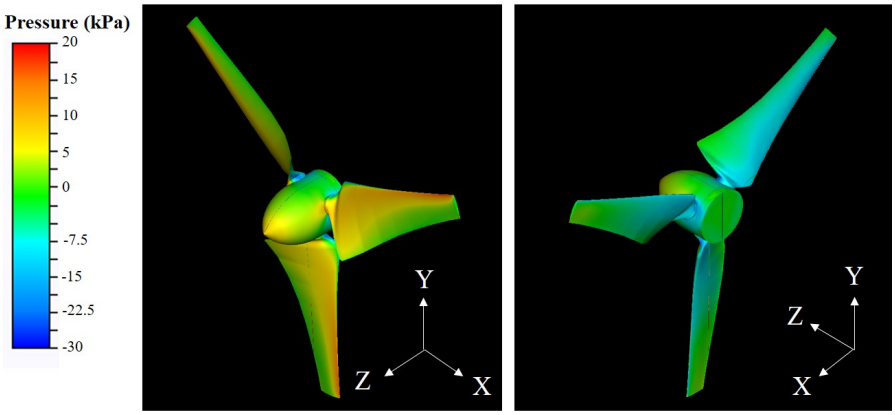

(b) Pressure distribution on the designed blade

Figure 3.7: Hydrodynamic performance of the designed HAT 10kW

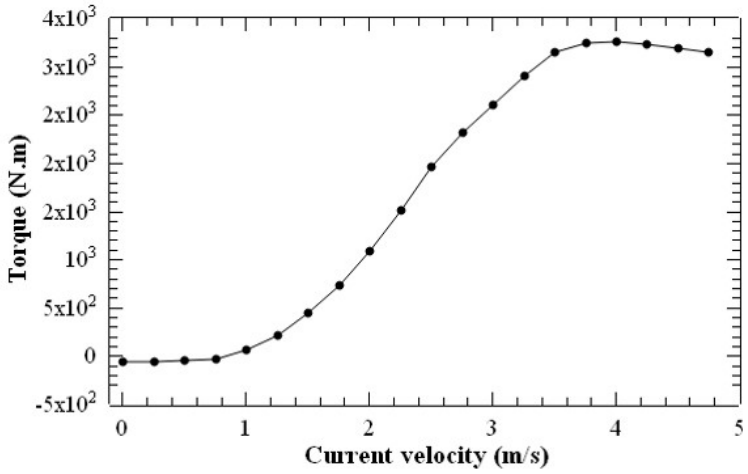

Figure 3.8: Estimated torque of the designed blade with current speed

Table 3.2: Computational conditions

Condition	Values
Inlet current speed	3 m/s
Outlet (static pressure)	0 Pa
Rotational speed (n)	75 rpm
Turbulent model	k-omega SST
Turbulent intensity	10%
Water density (ρ)	1025 kg/m^3
Advection scheme	Modified Petrov-Galerkin

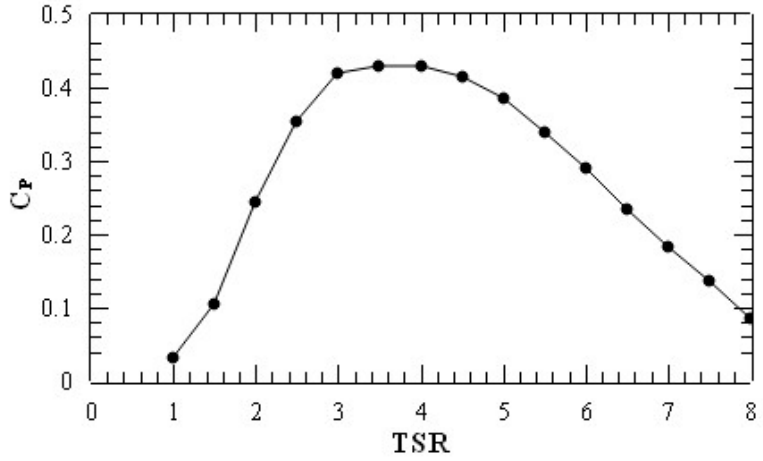

Figure 3.9: Power coefficient curve of the designed turbine with TSR

archipelago area in Indonesia.

Fig.3.10 presents the power curve of the designed HAT 10kW optimized based on the baseline blade, NREL S814 hydrofoil. Considering the tidal-current velocity at the focusing area, the turbine blade could generate the designed power of 10kW at the specific location with minimum averaged velocity 2.0m/s. Theoretically, the designed HAT 10kW could generate the total electric energy per year, 87.66 MWh. According to Word Bank data in 2014 [9] , the energy consumption per capita was estimated, 814 kWh. Therefore, the annual power supply by the designed HAT 10kW, can provide the electricity for about one hundred people at the focused archipelago area. Moreover, when the maximum tidal-current flow at Lombok strait is about 4m/s, the designed turbine would be able to generate electric power for more than five hundreds people living there.

The power curve of the designed turbine as mentioned above is necessary to quantitatively evaluate possibility of harvesting tidal-current energy using the optimized turbine. Based on

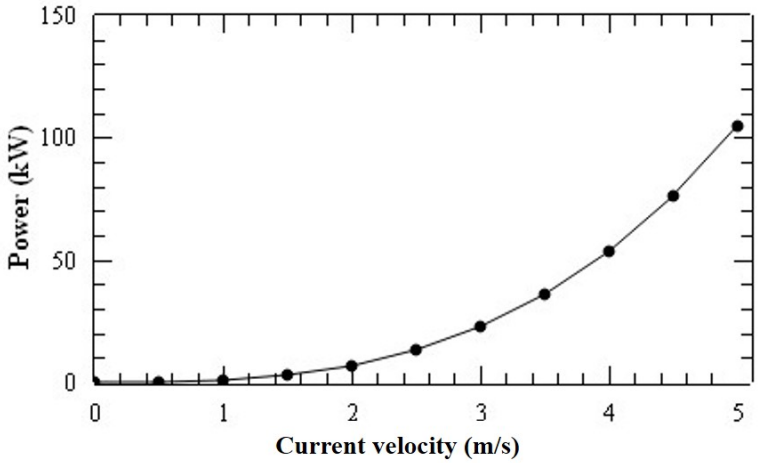

Figure 3.10: Estimated power curve of the designed HAT 10kW with current speed

the estimated power in Fig.3.10, the regression curve of the power can be fitted as below:

$$P_{turbine} = 0.8373V^3 - 6 \times 10^{-9}V^2 + 1 \times 10^{-8}V - 2 \times 10^{-9} \tag{3.2}$$

where V is the current velocity at x-axis. By using the regression equation and the tidal-current velocity field in time and space as mentioned in Sec. 2, the possibility of harvesting tidal-current power produced by the optimized turbine is shown in Fig.3.11.

The designed turbine can harvest the minimum target requirement of the electric power 10kW at the archipelago area. Moreover, some of the focused locations have the main path line of Indonesian Through Flow (ITF), which can strengthen potential of current energy harvesting. In future effort, we have to examine and estimate electric performance considering the velocity potential and characteristics of seasonal and annual variation of ITF.

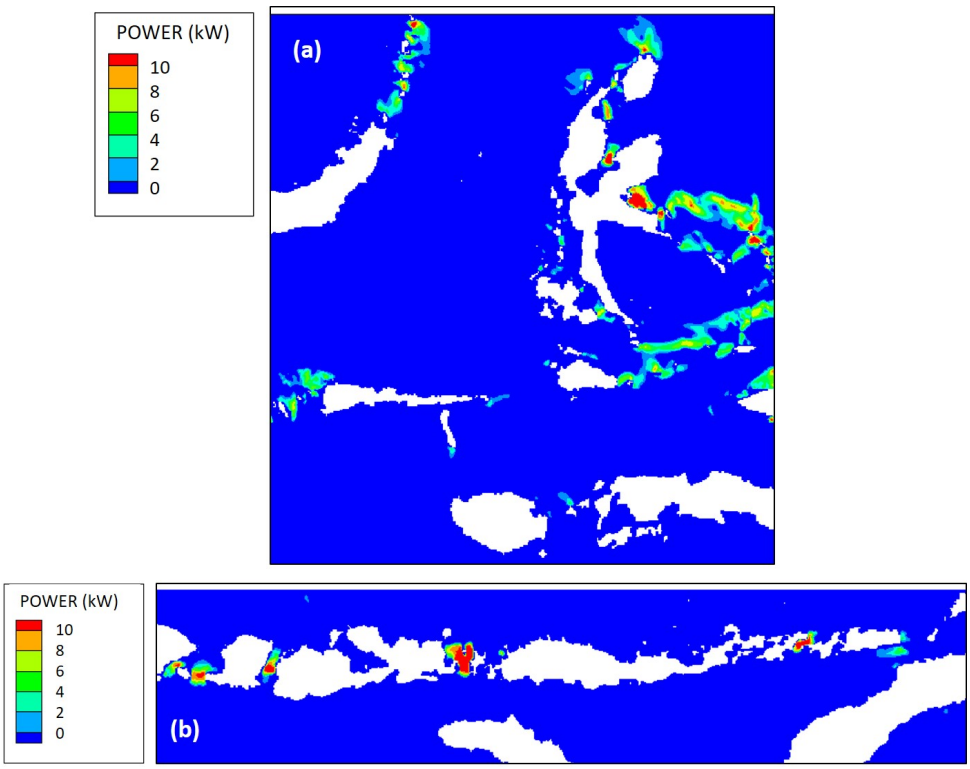

Figure 3.11: Estimated electric power generated by the designed HAT at (a) Maluku islands and (b) Nusa Tenggara islands

3.5 Conclusions

The small-sized HAT 10kW class with the diameter 2.2m, was theoretically and numerically designed and optimized considering the specific tidal-current at the archipelago areas, and also velocity field around the designed turbine and pressure distribution on it were examined. The baseline blade was designed based on NREL S814 hydrofoil with $AoA = 8°$, the $C_L = 1.256$, and $C_L/C_D = 90.5$ at current velocity, 3m/s at the focused archipelago area. The designed turbine can generate electric power for more than one hundred people at Lombok strait. The power distribution produced by the designed turbine was mapped by using the estimated power curve at Maluku islands and Nusa Tenggara islands.

In future efforts, the electric performance of the small-sized HAT will be evaluated considering seasonal and annual variation of tidal-current and ITF using more fine grids to survey a hot spot for installing a tidal-current harvester. And also experiment and fields tests should be conducted with a prototype to examine hydrodynamic and electric performance of the designed turbine.

Bibliography

[1] D Marten, J Wendler, G Pechlivanoglou, C. N Nayeri, and C. O Paschereit. QBlade : An Open Source Tool for Design and Simulation of Horizontal and Vertical Axis Wind Turbines. *International Journal of Emerging Technology and Advanced Engineering*, 3(3):264–269, 2013.

[2] Patrick Mark, Young-Do Choi, Patrick Mark Singh, and Young-Do Choi. Shape design and numerical analysis on a 1 MW tidal current turbine for the south-western coast of Korea. *Renewable Energy*, 68:485–493, 2014.

[3] M. Rafiuddin Ahmed. Blade sections for wind turbine and tidal current turbine applications-current status and future challenges. *International Journal of Energy Research*, 36(7):829–844, 2012.

[4] J.N. Goundar and M.R. Ahmed. Marine current energy resource assessment and design of a marine current turbine for Fiji. *Renewable Energy*, 65, 2014.

[5] Jai N. Goundar, M. Rafiuddin Ahmed, and Young Ho Lee. Numerical and experimental studies on hydrofoils for marine current turbines. *Renewable Energy*, 42:173–179, jun 2012.

[6] Robert Gasch and Jochen Twele. Blade geometry according to Betz and Schmitz. In Robert Gasch and Jochen Twele, editors, *Wind Power Plants: Fundamentals, Design, Construction and Operation*, pages 168–207. Springer Berlin Heidelberg, Berlin, 2012.

[7] H Glauert. Airplane Propellers. In *Aerodynamic Theory: A General Review of Progress Under a Grant of the Guggenheim Fund for the Promotion of Aeronautics*, pages 169–360. Springer Berlin Heidelberg, Berlin, 1935.

[8] Nj Georgiadis, Da Yoder, and Wb Engblom. Evaluation of modified two-equation turbulence models for jet flow predictions. *AIAA journal*, (January):1–16, 2006.

[9] World Bank. Electric power consumption (kWh per capita), 2014.

Chapter 4

Fish Aggregating Device (FAD) with Ocean Energy Harvester

4.1 Overview of FAD

Several kinds of fishes have habit to be easily attracted and gathered around Fish Aggregating Devices (FADs), which is one kind of artificial floating ocean obstacles in the world. Fishermen are often using a drifting type and a mooring type of FAD to aggregate many fish species including tuna, mackerel, scads, sardines, etc., in several countries, especially in East Asia and Southeast Asia. FADs consist of a floater, submerged net, mooring line and a satellite buoy. The utilizations of FAD have been increasing to make fishing activities effective, efficient, stable and regular for a long time. In 2013, the total number of drifting FADs can be estimated from 81,000 to 121,000 around the world, e.g 9,000 in Japan, 7,300 in Philippines, 9,200 in USA and 10,000 in France. Robert et al.[1] discussed size-dependent behavior of tuna in terms of physiological abilities, diet segregation and anti-predator behavior. The review of FAD research can be found in Dempster et al.[2]. To collect large amounts of data and to develop a new method and model to assess the effects of climate change and anthropic pressure on the ocean, Moreno et al.[3] suggested the potential of FAD as scientific platforms with underwater camera, echo-sounders, acoustic receivers, coded tag etc.

In recent years, ocean energy harvesters have been proposed and developed during last three decades. Some of them have been already installed and constructed in real sea operation[4][5][6]. Many researches have been done to explore the possibilities of installing ocean energy harvesters on floating devices[7][8][9][10]. However, ocean energy devices could sometimes cause several ocean environmental problems and human discomfort such as effect on sedimentary process[11], fish dead [12], and noise caused by rotational turbine[13]. Particularly, large-sized ocean energy devices could affect ocean environmental destruction and some collisions in fishery industry and environmental preservation group although electric power is increasing more and more to meet requirement of energy volume consumption. Collision risks to marine mammals, fish and birds from these devices are also uncertain and they may remain until more devices are installed and monitored. However, it is essential to consider the possibility of collisions before installation to highlight potential areas of concern. A collision is considered to be an interaction among a marine vertebrate, fish and a marine renewable energy device. In addition, archipelago areas such as Japan and Indonesia, have many remote areas and small straits where a local and small energy device should be provided and optimized. Although a small-sized ocean energy device is not economically reasonable and feasible in remote area/island far from commercial power plant[14], the small-sized ocean energy device has many features such as compactness, portability, simple structure, and lower noise level. It can be also integrated as a clustered energy system for urban areas, isolated islands, small straits, whose energy system is quite different from ordinary large-sized energy plants. Most of these locations need strongly common demand for a next generation energy-life-style using energy harvesters from several kinds of energy resources including non-utilized renewable energy in many archipelago areas such as Japan, Indonesia and Asian countries. Therefore, a small-sized ocean energy device will be able to help us produce an individual electric power plant and fulfilling energy supply.

Under the above mentioned background, ocean energy harvesters should be needed and designed considering fish gathering devices, which is the most important key issues in fishing rights, fishery zone, fish resources, employment of fishermen and ocean environment/protection. Another potential use of a FAD is to be combined with ocean energy harvester such as current turbine and vibrated harvester using piezoelectric material[15][16], in order to generate independent

energy supply for navigational and environmental sensors. The FAD is a floating structure consisting of cylindrical metal frames and floaters with a mooring line supported by seabed. In general, the FAD can be used to gather many kinds of fishes and to produce an environment-friendly ecosystem by an artificial infrastructure. Some wireless sensors for monitoring ocean environment can be equipped on top of the FAD to record information of GPS and its structure condition in real-time sea state.

4.2 Design of FAD

Fishing Aggregating Devices, FADs plays an important role of gathering and catching fishes around it and also FADs can lead fishes to safety and feed area. In general, the moored type of FAD consists of two main parts such as floating reef and mooring cable with sinker or anchor as shown in Fig.4.1. There are so many types of FADs such as submerged, floating and fixed types for not only deep water region over 1000m but also shallow one less than 10 m. Normally, the life cycle of FAD is about only ten years with maintenance free. The construction and installation cost for FAD are also lower than those of other ocean structures. Fig.4.2 shows one snapshot of the FAD with the mooring cable in the deep water of real sea state. It can be found that many swimming fishes gather around the FAD and they can migrate near the FAD without feed.

In this study, a new type of Fishing Aggregating Device (FAD) with an ocean energy harvester, e.g. horizontal and vertical axis current turbine, is proposed as shown in Fig.4.3. Normally, the FAD has two parts such as the floating reef with many floaters surrounded by aluminum frames and the mooring system part with three sections consisting of the sub-mooring chain, the upper mooring cable and the lower one. The FAD can be floated near the sea surface and mooring by the sinker such as anchor and caisson at seabed. The mooring system of the FAD is usually employed with single catenary cable to reduce the cost for installation, construction and maintenance, and also to avoid snap load caused by severe sea conditions. As shown in Fig.4.3, the FAD can be combined with several kinds of energy harvesters such as wind power generator

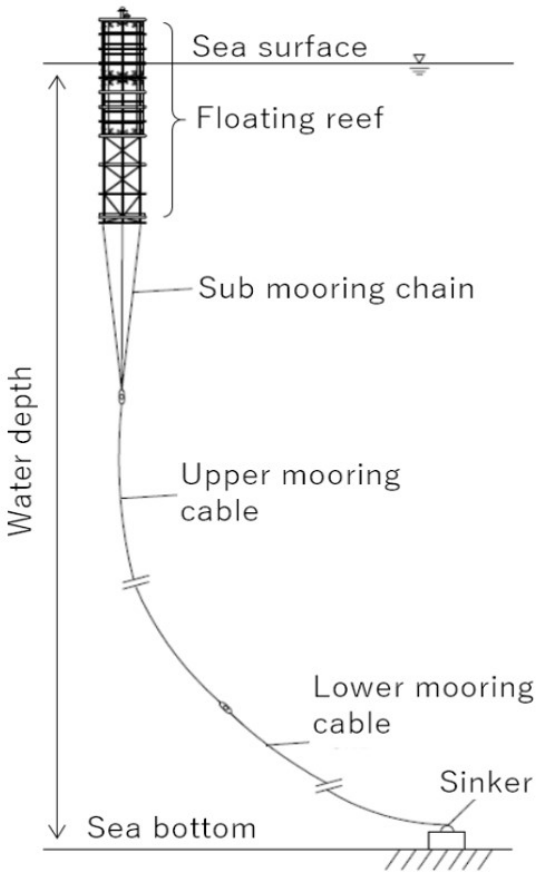

Figure 4.1: Illustration of mooring type of Fish Aggregating Device (FAD)

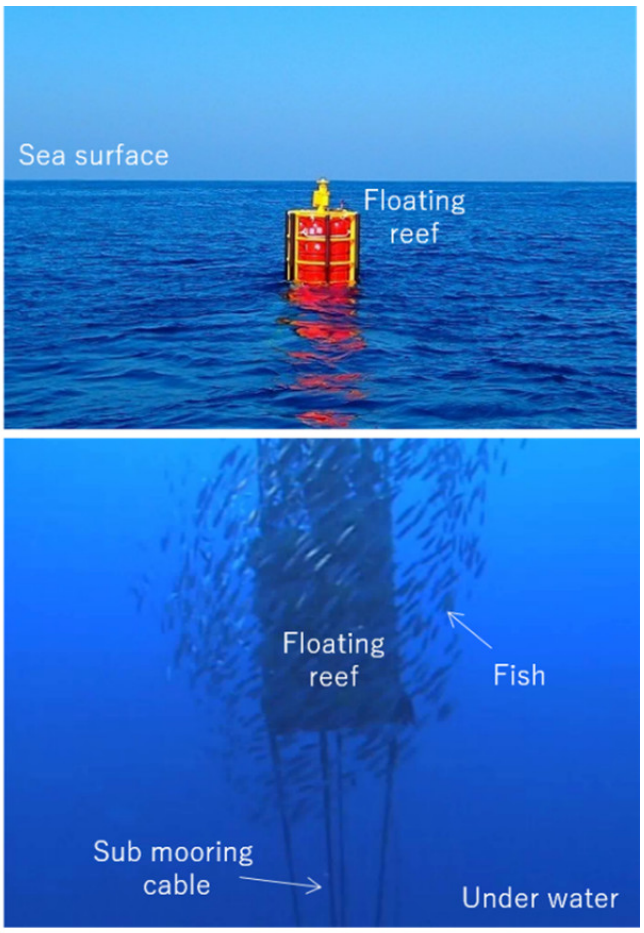

Figure 4.2: Snapshots of mooring type of FAD surrounded by many swimming fishes recorded by a diver in real sea condition

on the top of it, the ocean power generator inside the frame and the vibration energy harvester such as piezoelectric material[15][16] attached with the frames of the FAD. Using these kinds of energy harvesters, the electric power can be used to activate and boot up several sensors for ocean environmental monitoring, warning system for tsunami disaster and navigation system for ship transportation. The generated electric power can be utilized and stored at battery to save energy consumption for social requirement on energy network system in small scale and extensive style, not in big scale and intensive style.

To design an FAD with an ocean energy harvester, several kinds of sea conditions including wave, tidal current and wind should be considered as shown in Fig.4.4. The FAD with the catenary mooring can be stable and floated with the draft line in mild sea state represented by Case 1, which is relatively low velocity condition as a platform with ocean energy harvester.

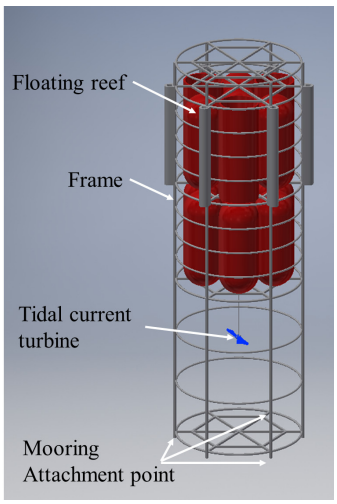

Figure 4.3: Illustration of FAD with ocean energy harvester

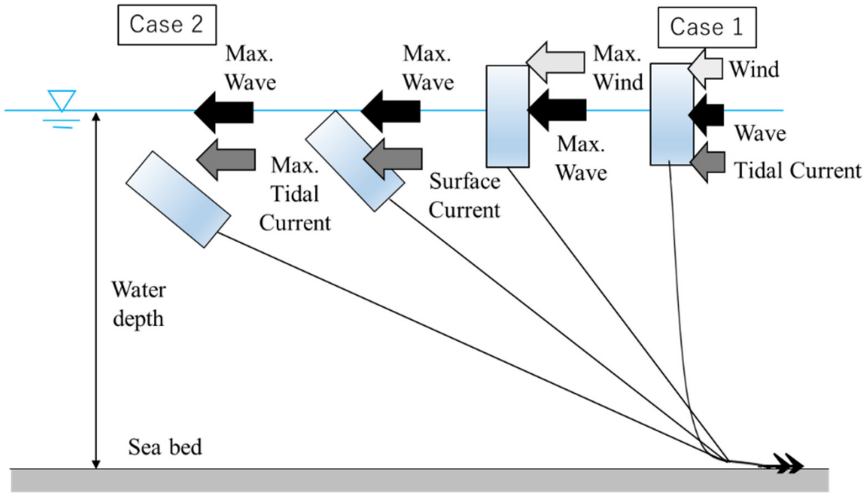

Figure 4.4: Mooring situations of FAD in several sea states

On the other hand, in Case 2, the FAD with tension mooring is inclined and submerged in high velocity condition, in which spiky snap load on mooring system can be often occurred in high velocity condition. VIV can also be excited by Karman vortices around the FAD and then the mooring cable could be fatigued and broken. Therefore, in this study, a suitable and useful technique is investigated to reduce snap load and VIV and then the flow field around the FAD with an ocean energy converter is also examined in Case 1 and Case 2. In practical use, a current turbine inside the FAD would be automatically operated with a stabilized position and flow direction using a gyroscopic control in real time.

4.3 Design of Current Turbine inside FAD

In this study, a current turbine can be installed at the bottom part of FAD to be applied for an archipelago area with fishery and aquaculture as shown in Fig.4.3. A horizontal or vertical axis current turbine can be adjusted to the FAD whose size can be selected by a diameter of the FAD, normally less than a few meters for small scale and extensive energy style. In this preliminary research, both horizontal and vertical types of current turbines are designed to customize energy requirements and to be installed at several locations in archipelago areas with aqua cultures. Fig.4.5 shows illustration of a small-sized current turbine installed at the

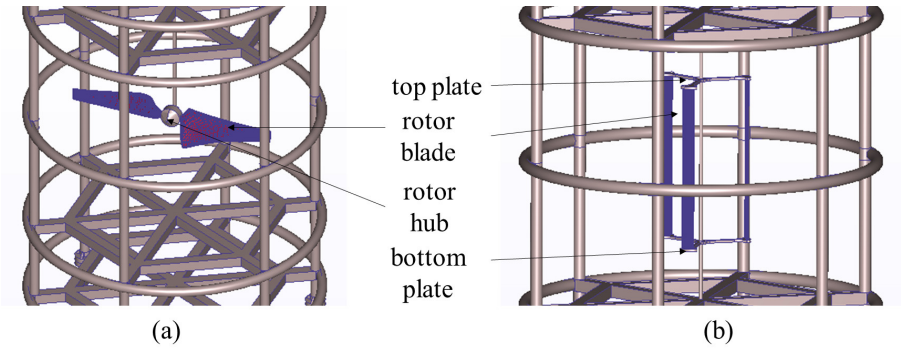

Figure 4.5: A current turbine installed at bottom part of FAD, (a) HAT and (b) VAT

bottom part of FAD. Considering collision between marine vertebrate, fish and a rotational turbine, some frames around the turbine can be arranged to avoid fish strikes, floating debris and seaweed. In the other hand, the frame arrangement of FAD should be optimized to avoid velocity fluctuation caused by frames.

To develop a Horizontal Axis Turbine (HAT) in a unidirectional current field, NREL S814 hydrofoil is chosen because it has 25% thickness and it can keep a good performance even if at rough sea conditions[17]. For a multi-directional current field, a Vertical Axis Turbine (VAT) has many types of its rotor shape, such as straight or curved-bladed Darrieus turbine, Savonius, Helix, and Troposkien type. Considering simple design for installation and maintenance of the FAD in real sea state, the Darrieus type[18] can be selected in this study. To achieve high electric performance of the VAT, NACA0018 is selected to develop the turbine as the main blade chord. The wind section based on NACA0018 is commonly employed for the VAT, especially one can use the Darrieus turbine with relatively high-thickness to chord ratio, which can give it suitable strength in bending[19].

4.4 Experimental Setup

In this experiment, the model scale 1/100 to a real sea condition was decided, based on Froude law, under some limitations in the experimental conditions. The size of FAD in model scale is shown in Fig.4.6. The floating parameters such as gravity center, center of buoyancy, metacenter and draft were decided by the design of FAD in a real scale. The FAD consisting of many

complicated horizontal/vertical frames was actually simplified with the connection part and the surface roughness of the FAD model in this experiment. Model-A was employed as a typical FAD. In general, VIV excited by Karman vortices around a bluff body should be considered in a designing floater with a mooring system. In this study, Model-B with the wider draft line was also designed to escape from VIV depending on Strouhal number with a diameter of floater and a current velocity.

Fig.4.7 shows the experimental setup and the measuring system to investigate the mooring forces acting on the FAD and its motions due to wave and current conditions in the towing tank (Length 100 m × Width 8 m × Depth 3.5 m) at Hiroshima University. The incident wave height is set to be 0.04-0.16m with the wave period 1.0-1.6s, and the current speed is 0.1-0.3m/s in the model scale. The FAD model was supported by the pulley with the mooring line connecting to the load cell to measure the mooring force. The pulley can be located at certain water depth where the deep water condition can be achieved for the wave length used in this experiment. To capture the FAD motions in sway and surge directions and under water motions in several wave and current conditions, the two video cameras were set above the FAD model. The motion in heave direction and the inclined angle of FAD were recorded by the side water proof camera. The wave gauge and current meter were located at the upstream side of the FAD model to obtain incident wave height and current velocity. All of the measuring systems were set on the towing train to create current conditions in the towing tank.

Impact force on the FAD can be occurred by snap load due to big wave with high steepness and then mooring line of the FAD can be broken with fatigue. To reduce the snap load caused by impulsive force on mooring line, two mooring systems were examined as shown in Fig.4.8. The elastic part in the mooring system was partially applied to be compared with the chain mooring system. The dimension of the elastic mooring part is 40mm length and 5mm square. To decide the elastic coefficient by considering the existing mooring system[20] and the previous application[21], installation site, and sea condition, the experiment of tensile force was conducted to evaluate strains of some rubbers with different elastic coefficients (No.1-No.4). As shown in Fig.4.9, the elastic coefficient of the rubber was averaged and selected, 3.75 N/cm in the model scale of this study.

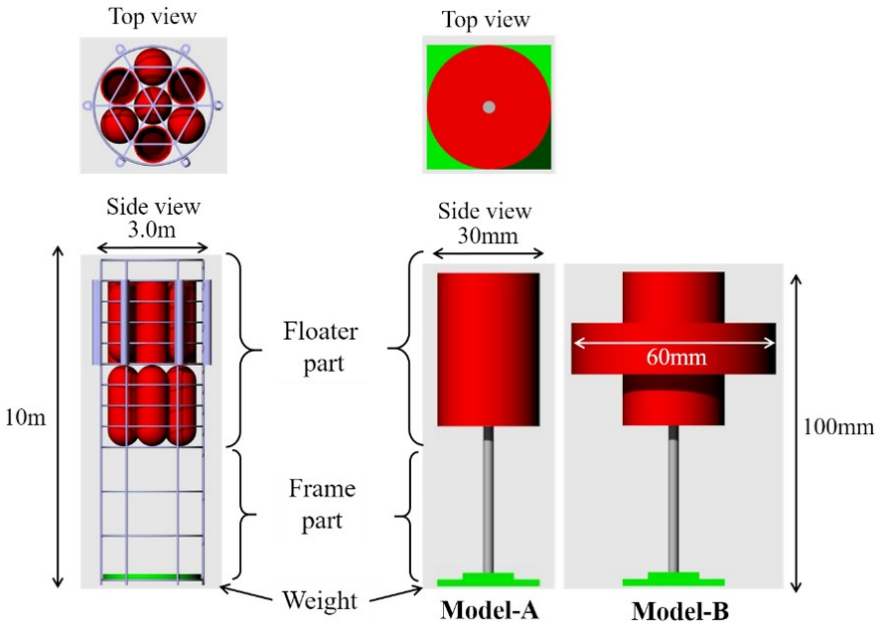

Figure 4.6: Overview of FAD model in real scale (left) and model scale 1/100 (right)

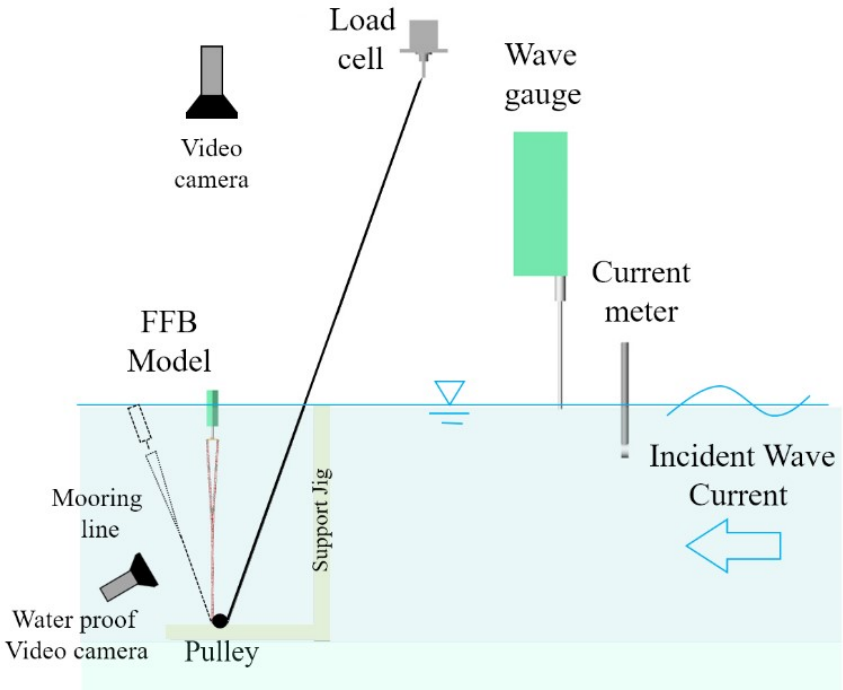

Figure 4.7: Experimental setup and measuring system in towing tank

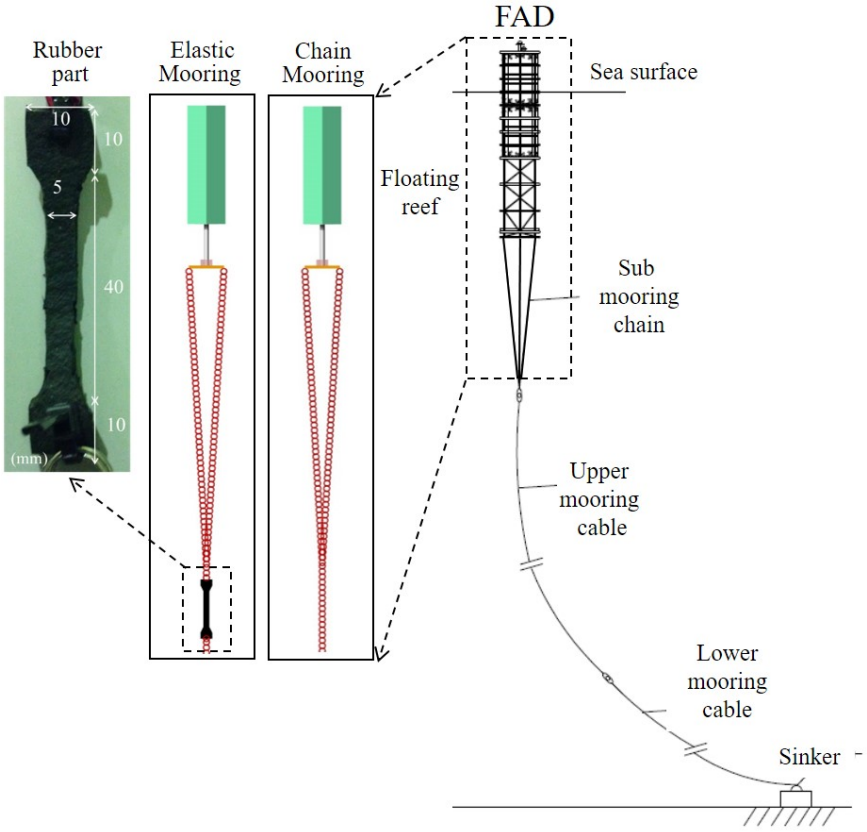

Figure 4.8: Mooring model of FAD with elastic rubber

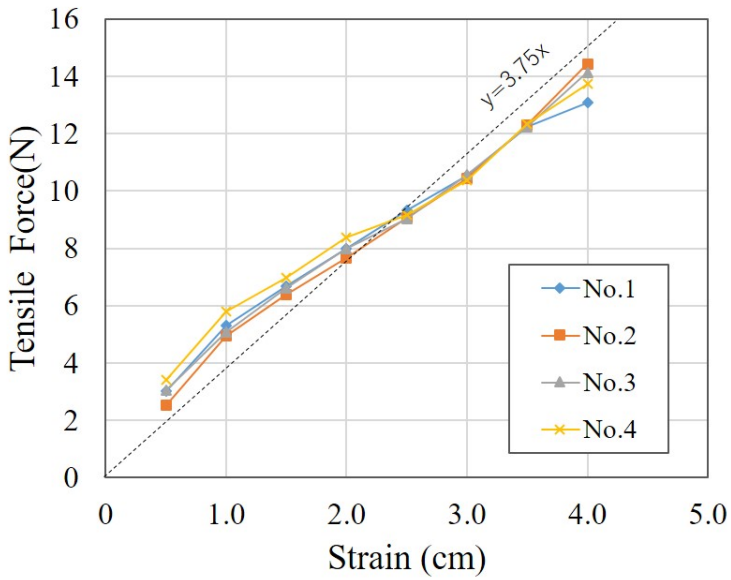

Figure 4.9: Relations between tensile force and strain of elastic mooring part

4.5 Computational Fluid Analysis for FAD

To investigate flow field around the FAD with a current turbine and to estimate electric power, the computational fluid analysis, CFD is conducted by using the commercial software, Autodesk CFD Motion 2016[22]. The continuity and unsteady Reynolds-Averaged Navier-Stokes (URANS) equations are used with the $k-\epsilon$ turbulent model for whole computational domain and the $k-\omega$ SST (shear-stress transport) model for focused one as follows:

$$\frac{\partial \overline{u_i}}{\partial x_i} = 0 \tag{4.1}$$

$$\frac{\partial \overline{u_i}}{\partial t} + \overline{u_j}\frac{\partial \overline{u_i}}{\partial x_j} = -\frac{1}{\rho}\frac{\partial P}{\partial x_i} + \frac{\partial}{\partial x_j}\left\{(\nu+\nu_t)\left(\frac{\partial \overline{u_i}}{\partial x_j} + \frac{\partial \overline{u_j}}{\partial x_i}\right)\right\} \tag{4.2}$$

$$\frac{D(\rho k)}{Dt} = \tau_{ij}\frac{\partial \overline{u_i}}{\partial x_j} - \beta^*\rho\omega k + \frac{\partial}{\partial x_j}\left[(\mu+\sigma_k\mu_t)\frac{\partial k}{\partial x_j}\right] \tag{4.3}$$

$$\frac{D(\rho\omega)}{Dt} = \frac{\gamma}{\nu_t}\tau_{ij}\frac{\partial \overline{u_i}}{\partial x_j} - \beta\rho\omega^2 + \frac{\partial}{\partial x_j}\left[(\mu+\sigma_\omega\mu_t)\frac{\partial \omega}{\partial x_j}\right] + 2\rho(1-F_1)\sigma_{\omega 2}\frac{1}{\omega}\frac{\partial k}{\partial x_j}\frac{\partial \omega}{\partial x_j} \tag{4.4}$$

where $D/Dt = \partial/\partial t + \overline{u_i}\partial/\partial x_i$, ρ is the density, t is the time, $\overline{u_i}$ is the time averaged velocity, ν is the coefficient of kinematic viscosity, ν_t is the coefficient of eddy viscosity, μ is the coefficient of viscosity, μ_t is the coefficient of eddy viscosity due to turbulence, P is the pressure, k is the turbulent kinetic energy, ω is the specific turbulent dissipation rate, τ_{ij} is the viscous stress, F_1 is the function designed to be one in the near wall region and zero away from the surface. And also β, β^*, σ_k, γ, σ_ω and $\sigma_{\omega 2}$ are the constant parameter defined by Menter[23].

The advection term is discretized by the monotone streamline upwind scheme for the whole domain including the FAD and the modified Petrov-Galerkin for the focused domain around a turbine with constant rotational speed. The two mooring situations of the FAD are selected to investigate fluid force on the FAD at low velocity as a mild sea state in Case 1 and high velocity as a severe sea state in Case 2 as shown in Fig.4.4. To focus on flow structure field around the FAD and to examine hydraulic performance of a turbine, mooring cable and motions of the FAD are ignored in CFD. The inclined angle of the FAD is imposed based on the experimental result. The computational domain is $15D$ in length, $5D$ in width, and $5D$ in depth, where D is

the diameter of the FAD. The FAD is located at the distance from the upstream boundary, 3D. The inlet flow condition is set to be the designed velocity, u=1.0-3.0m/s. The outlet condition is imposed with static pressure, zero. The unstructured mesh system is employed in the whole domain. The averaged grid size, dx/D is 0.05 for the surface of turbine blade, especially the minimum one, dx/D is about 0.001 for the local element such as joint part of frame. The total number of elements for the FAD with a current turbine is about 3 to 10 million at each velocity condition. The water density, ρ is 1,025 kg/m^3 and the coefficient of viscosity is 1.08×10^{-3} Pa·s. The time increment is set under Courant-Friedrichs-Lewy (CFL) condition.

4.6 Theoretical Analysis of Fluid Force on FAD

To validate the numerical model as mentioned in Sec.4.5, the total force on the FAD should be compared to the experimental results and theoretical ones. The fluid force can be theoretically calculated by the regulation of floating obstacles supervised by Fisheries Agency of the Ministry of Agriculture, Forestry and Fisheries in Japan, which means a preliminary design manual in Japan [24]. The basic theory at steady state is represented by mechanical balance among wave, current, wind, mooring tension, buoyancy of obstacle and weight.

The fluid force on the FAD can be considered in the theory and the wave force, P_D on the FAD can be written by

$$P_D = C_D A_w \frac{w_0}{2g} V_{m1}^2 \tag{4.5}$$

$$V_{m1} = \pi \frac{H}{T} e^{-2\pi z/L} \tag{4.6}$$

where C_D is the coefficient of drag force on the FAD, A_w is the projected area considering inclined angle of the FAD under the sea water, w_0 is the specific weight in the sea water, g is the gravity acceleration, V_{m1} is the maximum water velocity due to the significant wave H with the wave length L and the wave period T and z is the water depth.

The body force, P_M on the FAD can be also written by

$$P_M = C_M V_{FAD} \frac{w_0}{g} \frac{2\pi}{T} V_{m1} \tag{4.7}$$

where C_M is the coefficient of body force on the FAD, V_{FAD} is the volume of the FAD, and T is the wave period. The current force, P_C on the FAD can be defined by

$$P_C = C_D A_w \frac{w_0}{2g} U_z^2 \tag{4.8}$$

where U_z is the current velocity at the water depth z. The steady fluid force, P_W on the FAD caused by wave and current is represented by

$$P_W = \frac{w_0}{2g} C_D A_w (V^2 + \beta V_{m1}^2) \tag{4.9}$$

where V is the velocity due to tide, ocean current and wind drift current, β ($0 \leq \beta \leq 1$) is the empirical parameter regarding with V/V_{m1}. To consider interaction force between wave and current, the maximum force, P_F on the FAD can be defined by

$$P_F = P_D \left(sin\theta + \frac{V}{V_{m2}} \right)^2 - P_M cos\theta \tag{4.10}$$

where V_{m2} is the maximum velocity due to wave in downstream direction of mooring force, θ is the phase shift from a certain time when the maximum force is occurred, that is obtained by iteration. The wind force, P_A on the FAD above the sea surface is written by

$$P_A = \frac{U_{10}^2}{2g} w_a \sum (C_D A_a) \tag{4.11}$$

where U_{10} is the averaged wind velocity during 10 minutes on the sea surface, w_a is the specific weight in the air, C_D is the coefficient of drag force in the air, A_a is the projected area of the FAD above the sea water. The fluid force, P_k on the mooring part is calculated by

$$P_k = \frac{1}{2} \frac{w_0}{g} \int_0^h C_D A_k U_z^2 dh \tag{4.12}$$

where C_D is the coefficient of drag force on mooring part, A_k is the projected area of mooring part and U_z is the vertical distribution of velocity regarding with water depth, h. The buoyancy force, P_L of the FAD is calculated by

$$P_L = w_0 V_{FAD} \tag{4.13}$$

where V_{FAD} is the volume of FAD. In this paper, all of the forces are considered at each condition as shown in Fig.5.4. According to the designed manual of the FAD supervised by Fisheries Agency of the Ministry of Agriculture, Forestry and Fisheries in Japan [24], the floating part of the FAD consisting of some columns can be assumed by a cylinder and the frame part of the FAD is also considered by a slender pole having the same projected area. In this study, the coefficients of the drag force, C_D can be determined by the primary experiment and the designed manual as mentioned. The value of C_D was set to be 0.82 for Model-A and 0.93 for Model-B, measured by the experiment. The coefficient of the body force, C_M was selected 2.0, considering the added mass. Meanwhile, the coefficient of drag force in the air was also set to be 1.2 based on the designed manual.

4.7 Blade Element Momentum Theory for Blades of HAT and VAT

In this study, the software, Qblade proposed by TU Berlin[25], is employed as the first step to design and optimize a current turbine and to investigate its performance at a focused area. The theory is based on Blade Element Momentum, BEM[26] and it can consider the momentum theory with the blade element theory. Using the momentum theory, inflow factors for a designed blade can be derived in axial and circumferential directions, while tip loss factor is also introduced to take into account a finite blade span. Moreover, drag and torque are also estimated by dividing rotor blade into a number of elemental sections using the blade element theory. The combination of both theories can predict rotor thrust loading and power loading calculated by fluid momentum changes to blade force based on drag and lift coefficients at

angle of attack (AoA) of a blade section. The number of rotor blade is decided by using an approximation based on the Prandtl tip loss factor[27]. Prandtl simplified turbine wake by modeling helical vortex patterns as vortex sheets which have no direct effect on wake itself. The correction factor, F to induced velocity field, can be expressed by

$$F = \frac{2}{\pi} cos^{-1} e^{-f} \tag{4.14}$$

where $f = \frac{N}{2}\frac{R-r}{rsin\varphi}$, R is the blade radius, N is blade number, r is the section radius, and φ is the inflow angle. The correction factor is used to modify the momentum part of BEM theory, so that thrust extracted by each rotor section are equivalent to

$$dT = 4\pi r \rho U_{\infty}^2 (1-a) a F dr \tag{4.15}$$

where ρ is the fluid density, U_{∞} is the mean flow speed, and a is the axial induction factor. The distribution of chord section for a designed turbine can be optimized by Betz or Schmitz[28] as follows:

$$c(r) = \frac{16}{9}\frac{\pi R}{B C_L \lambda_0}\frac{1}{\sqrt{(\lambda_0 r/R)\, 4/9}} \tag{4.16}$$

$$c(r) = \frac{16\pi R}{B C_L} sin^2\left(\frac{1}{3} tan^{-1}\left(\frac{R}{\lambda_0 r}\right)\right) \tag{4.17}$$

where B is the number of blades, C_L is the lift coefficient, and λ_0 is the tip speed ratio.

4.8 Fluid Force on FAD and Its Motions

4.8.1 Validation

Before discussing characteristics of fluid force on the FAD, reduction of mooring force and motions of the FAD, the numerical and theoretical results are validated with the experimental one. Fig.4.10 shows one example of time history of fluid forces such as wave force Fw, current force Fc and wave-current force Fwc on Model-A in the experiment. In the wave-current

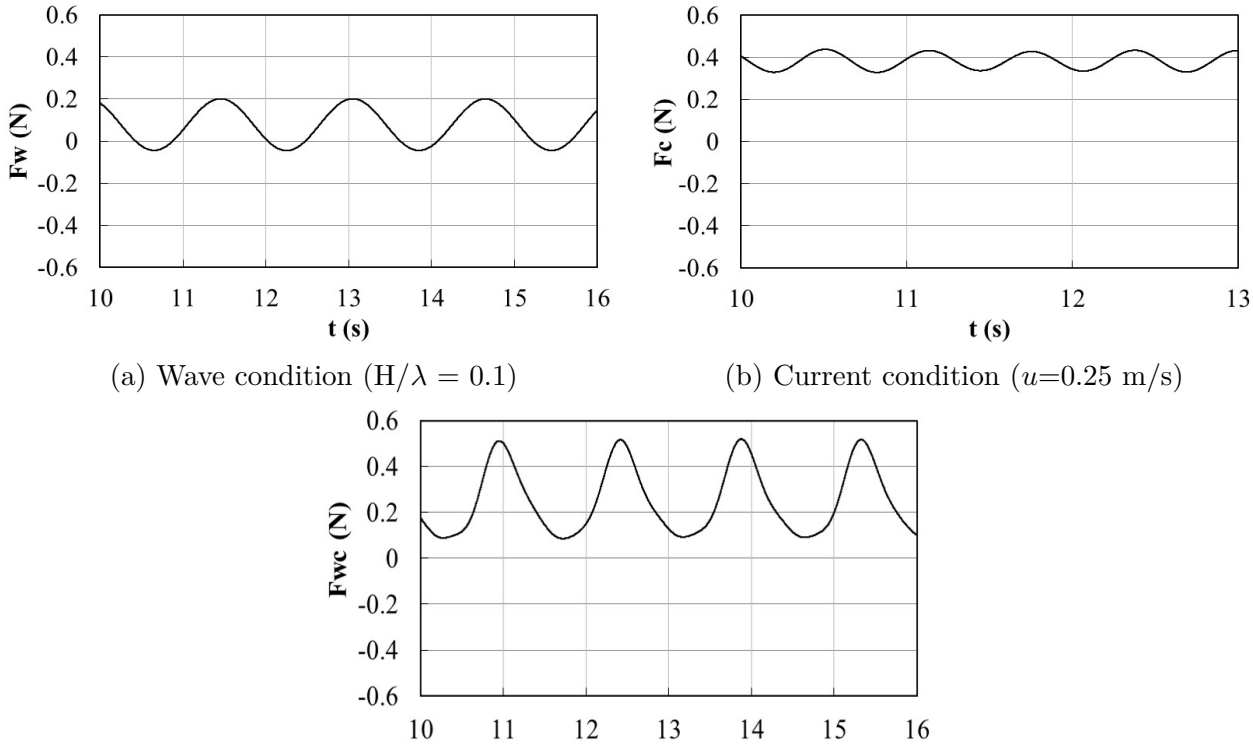

(a) Wave condition (H/λ = 0.1)

(b) Current condition (u=0.25 m/s)

(c) Wave-current condition (H/λ = 0.1, u=0.25 m/s)

Figure 4.10: Example of time history of mooring force acting on Model-A

condition, the Fwc is excited by interaction between wave force and current one, therefore the time history is shifted to the positive side and steepen comparing with the the others. Figs.4.11-4.14 show comparison of fluid force on Model-A and Model-B with theoretical and experimental results at three different conditions such as wave, current and wave-current, where Fw_{max} means the averaged maximum value in five waves with steady state and no-reflection effect, Fc_{ave} is the averaged current value and Fwc_{max} is the averaged maximum value excited by wave and current. The quasi steady state can be assumed in the numerical model and then the inflow condition due to wave and current at the upstream side is imposed by the experimental data obtained by the current meter. The numerical results in all cases are overall agreement with them in all conditions. However, there is a small discrepancy and different tendency in the wave and current condition, especially in the high velocity condition. This is because the water surface motion is gradually generated with spilling breaking and the resultant force can be increased in the experimental work, but nonlinear effect such as wave breaking and steep wave motion were neglected in the numerical model.

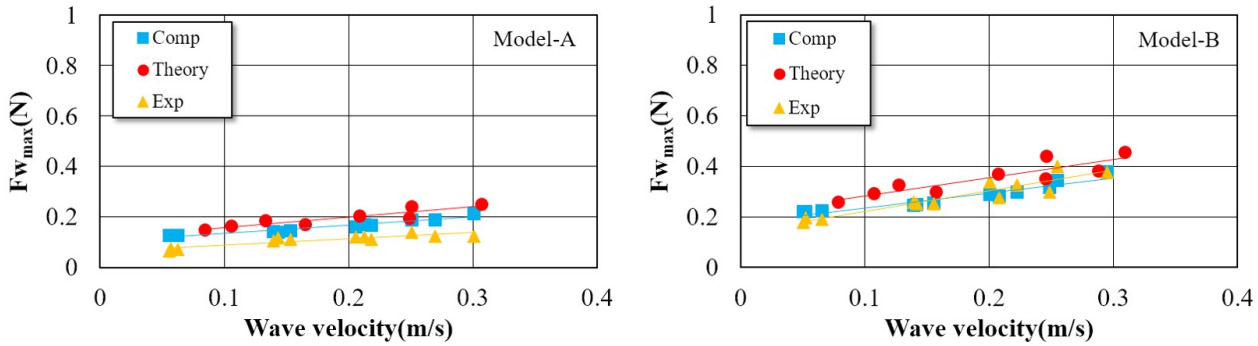

(a) Model-A (b) Model-B

Figure 4.11: Comparison of wave force on FAD between numerical result and experimental one

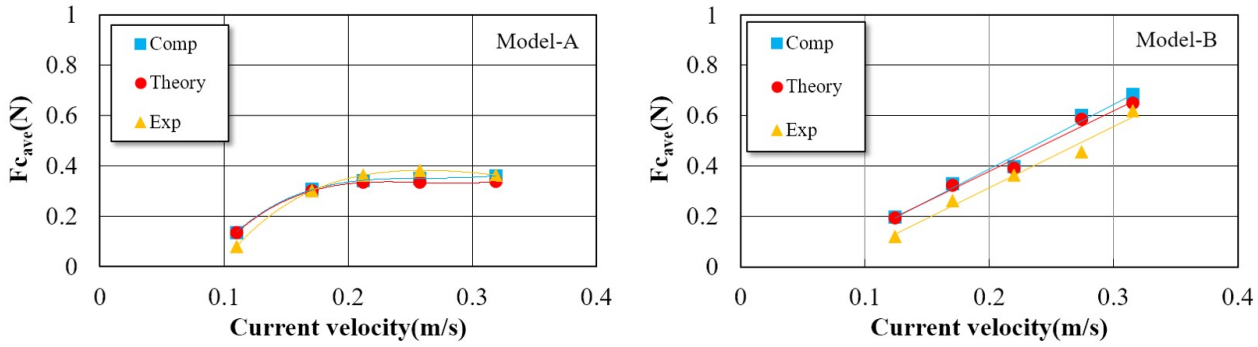

(a) Model-A (b) Model-B

Figure 4.12: Comparison of current force on FAD between numerical result and experimental one

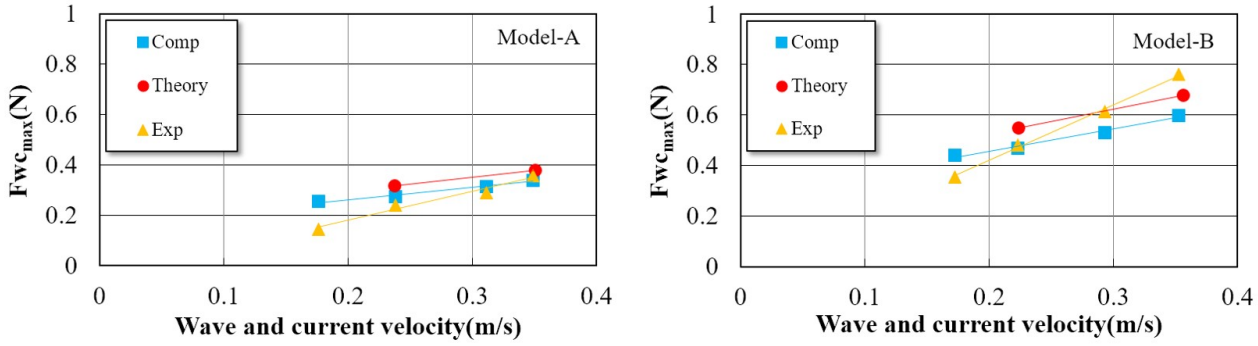

(a) Model-A (b) Model-B

Figure 4.13: Comparison of wave-current force on FAD between numerical result and experimental one when the current velocity is 0.1 m/s

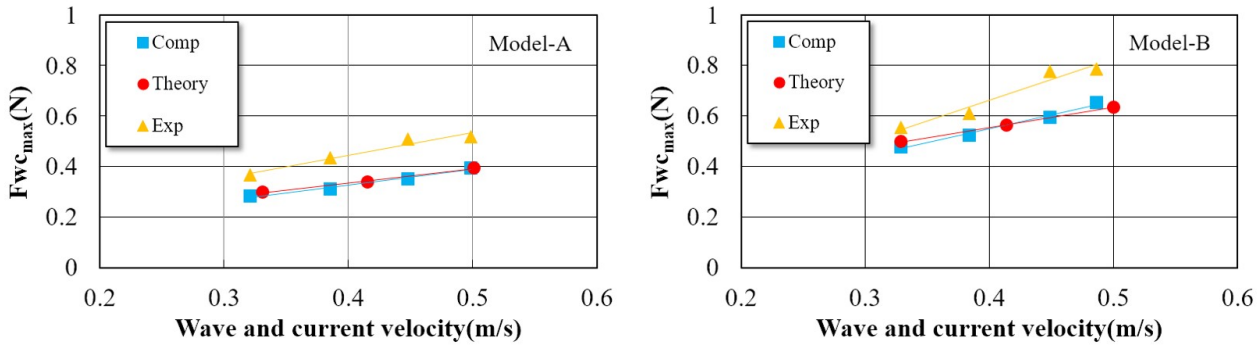

(a) Model-A (b) Model-B

Figure 4.14: Comparison of wave-current force on FAD between numerical result and experimental one when the current velocity is 0.25 m/s

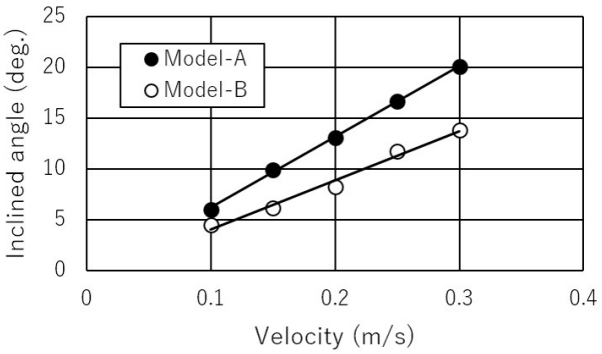

Figure 4.15: Comparison of inclined angle of FAD caused by current

4.8.2 Characteristics of Fluid Force and Flow Field around FAD

This section investigates characteristics of inclined angle of the FAD caused by fluid force. The flow field around the FAD is also visualized to examine a suitable layout of floating reefs and frames to install ocean energy harvester. Considering an installation site at an archipelago area as mentioned later in Sec.4.9.2, the rotational speed is set to be 75rpm to achieve the estimated power, 200W when the current velocity is 2m/s. Fig.4.15 shows comparison of inclined angle of the FAD between Model-A and Model-B. The angle caused by fluid force was captured by the video camera in the experiment. The inclined angle is linearly increasing with the current velocity and also the angle in Model-A is larger than that in Model-B. Because the buoyancy in Model-A is smaller than that in Model-B, and therefore Model-A can be easily submerged and sunk at the high velocity condition. Moreover, the vertical force due to buoyancy in Model-B is larger and Model B can escape from full submergence under these conditions. Fig.4.16 shows

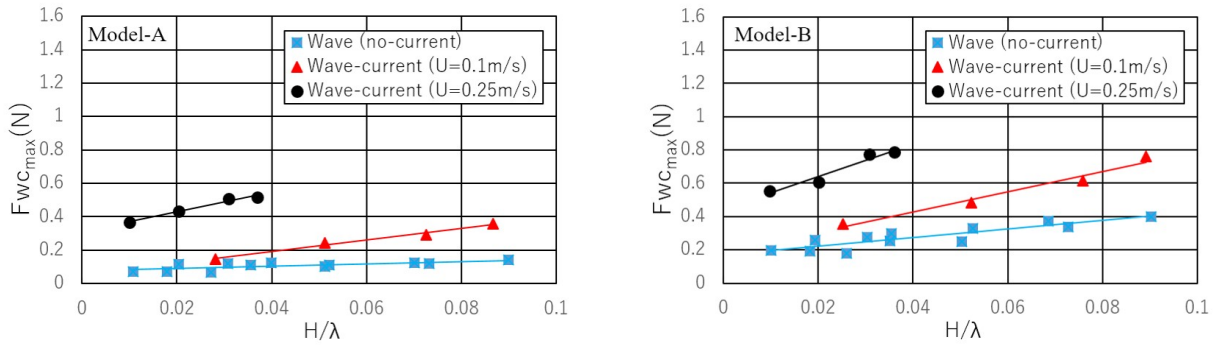

(a) Model-A (b) Model-B

Figure 4.16: Comparison of fluid force due to wave-current interaction with wave steepness

comparison of fluid force in wave and wave-current conditions in the experiment. The fluid force is increasing with wave steepness and also the force in wave-current condition is considerably larger than that in wave condition. This is because the nonlinear interaction between wave and current can be occurred and the resultant forces can be considerably increased. The forces in Model-B are almost twice larger than those in Model-A, especially at the wave-current condition (U= 0.25m/s). This means that the projected area of Model-B in horizontal and vertical directions are larger than that of Model-A and the buoyancy in Model-B is also larger than that in Model-A. Therefore, the fluid force in Model-B is relatively larger under these conditions but the floating motion could be decreased as mentioned in the next section. The fluid force on the FAD has strong relationship with flow field around the FAD with many frames. Firstly, to focus on the whole flow field around the FAD with the turbine, Figs.4.17 and 4.18 show streamline line and vortex field around the FAD with HAT and VAT in 3D at the low velocity condition (Case 1, U_{in}=1m/s) and the high velocity one (Case 2, U_{in}=3m/s) in real scale condition. The inclined angles of the FAD at each velocity were set based on the experimental result. It can be found that the flow field becomes fully turbulent vortex at the downstream side of the floating reef at the upper part of the FAD, whereas at the lower part of the FAD, the flow field is considerably uniform. The result means that the flow field around the turbine inside the FAD are not affected by the designed frame layout of the FAD at the upstream side. The optimized arrangement of frames on FAD should be examined to obtain highly electric performance and to accelerate flow velocity inside the FAD in future effort. On the other hand, the 3D vortex field at the upper part of the FAD can produce

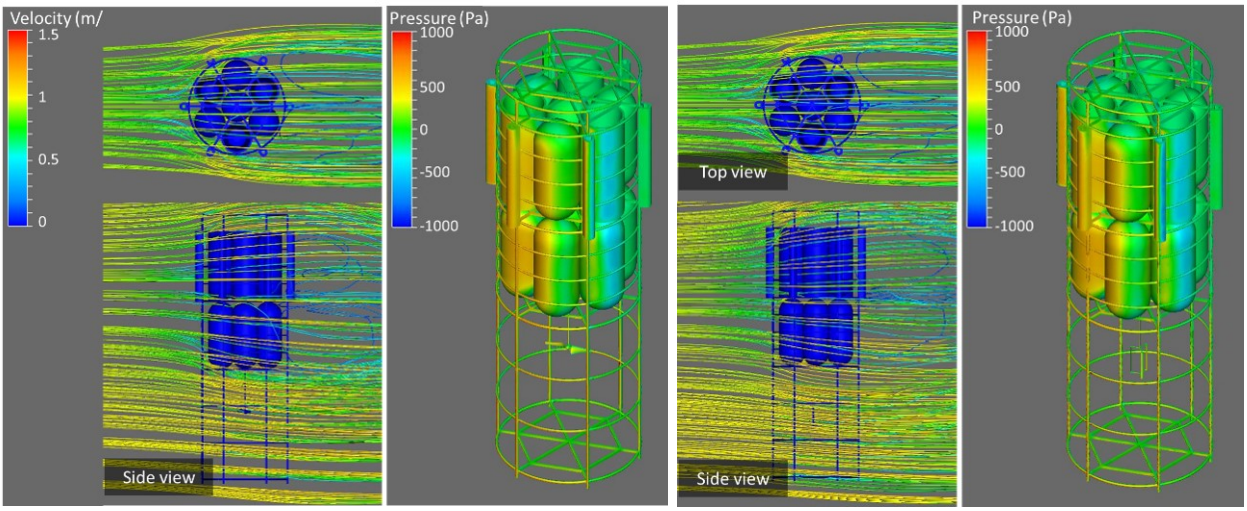

(a) FAD with HAT (b) FAD with VAT

Figure 4.17: Streamline around FAD with turbine and pressure distribution on FAD at low velocity condition

pressure fluctuation at the downstream side, and thus a vibration energy harvester as the previous work[16] can be attached on the frames of the FAD to obtain electric power from wave and current conditions. Next, to focus on flow field around the rotational turbine, Figs.4.19 and 4.20 show streamline line and vortex field in 3D around the rotational turbine at the low velocity condition (Case 1, U_{in}=1m/s) and the high velocity one (Case 2, U_{in}=3m/s) in real scale condition. The complicated and structural flows were fully developed at the downstream side in both HAT and VAT cases. However, it is still small magnitude in the area and also weak in the velocity comparing with a typical Karman vortices field generated around the floating reef, accordingly motions of the FAD and flow interaction between the FAD and the turbine could not be affected by the complicated flow field behind HAT and VAT. More detail discussion on interaction between them in force and motion, should be needed as future work.

To estimate effect of hydrodynamic force on FAD structure, assuming that there is no hydro-elastic deformation and mechanical vibration, the one-way FSI coupling procedure can be used to estimate hydrodynamic pressure on FAD, stress and strain distribution, and maximum displacement of FAD frame. Based on the pressure distribution of the blade surface as shown in Figure 4.21a and 4.21b, it can be observed that the maximum pressure at each blade is occurred at both the leading edge and the pressure side, while the low pressure is acting on the suction side and the trailing edge.

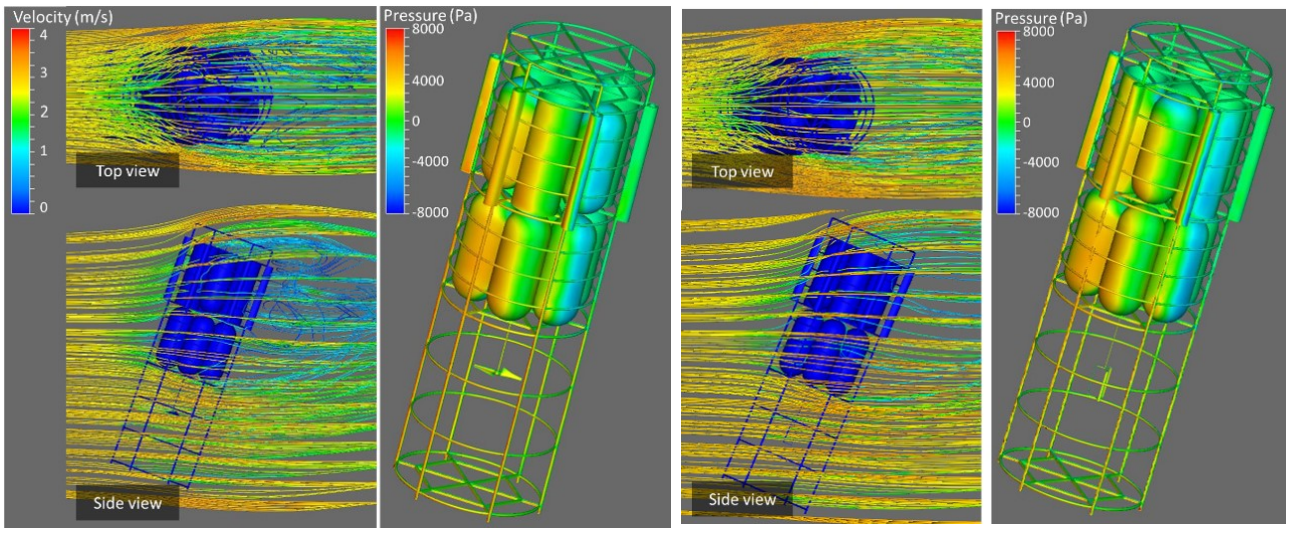

(a) FAD with HAT

(b) FAD with VAT

Figure 4.18: Streamline around FAD with turbine and pressure distribution on FAD at high velocity condition

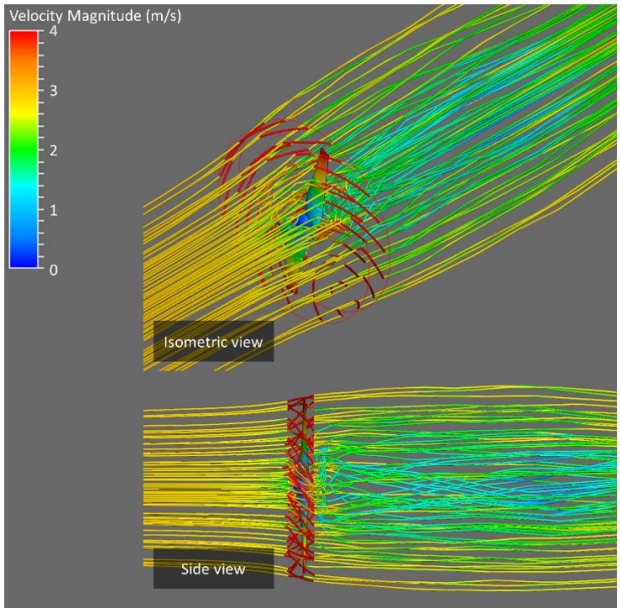

Figure 4.19: Streamline around HAT at high velocity condition

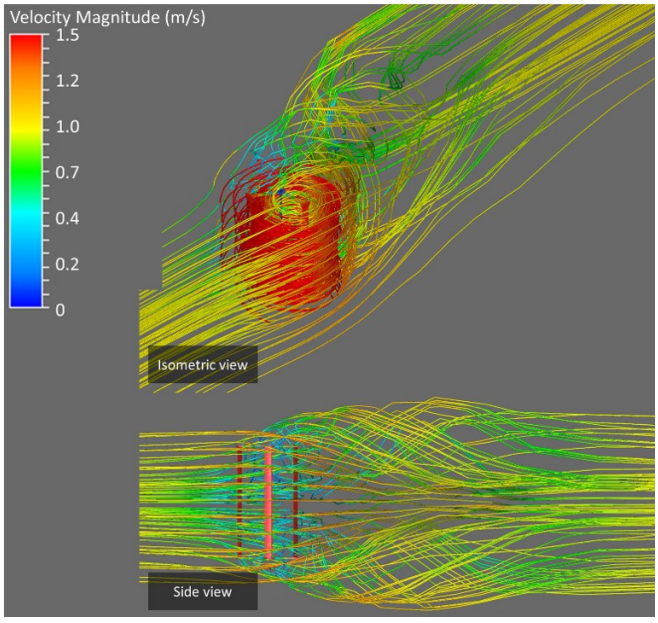

Figure 4.20: Streamline around VAT at low velocity condition

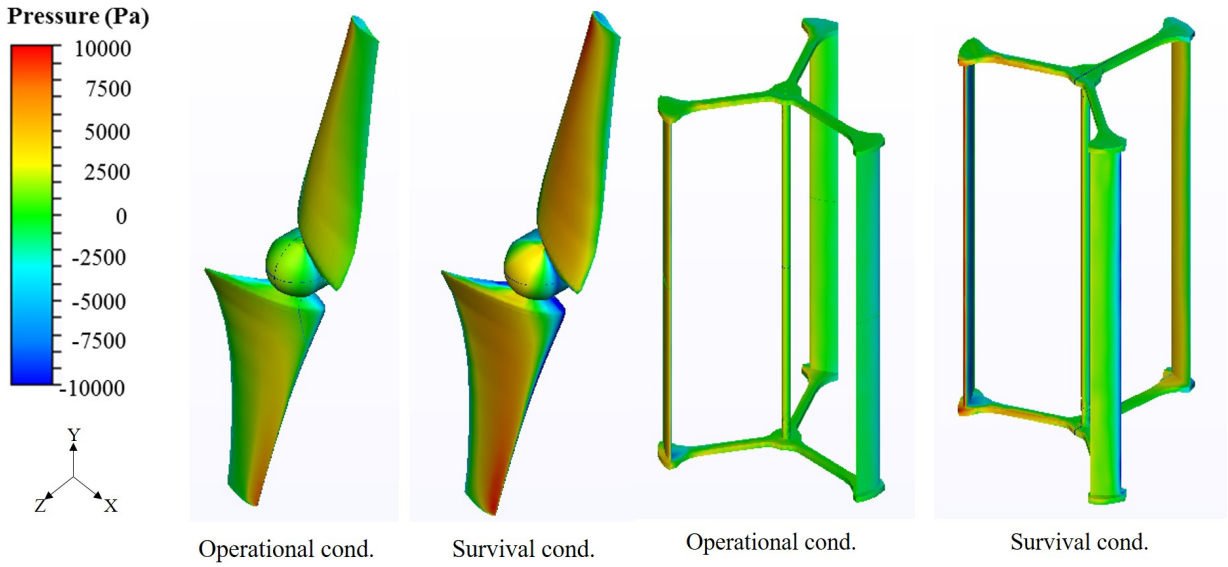

Figure 4.21: Pressure distribution on (a) horizontal, and (b) vertical axis tidal current turbine

The hydrodynamic load (pressure on the rotor blade surface) applied on the blade is imported from CFD analysis at TSR 5 for HAT and 3 for VAT, where the current velocity is 3 m/s for survival condition, and the rotational spreed is 75 RPM. The structural feasibilities is based on the deformation, stress, and strain on the FAD frame and rotor blade, which are summarized in Table 4.1. Under survival condition, the largest deformation of FAD is located at the central inside frame. The maximum displacement of the turbine blade is occur at the blade tip of HAT and at the blade mid-section of VAT, while the maximum stress is occurred at mid-section of the blade for both HAT and VAT, as shown in Fig.4.22. Other critical locations on VAT are located at the blade tip connected to the top and the bottom plates. On the other hand, the tendency of the strain distribution is the same with the stress distribution. However, from material properties explained in Table 4.1, it is observed that both FAD and designed turbines do not exceed the yield strength of all utilized material and remain in elastic region. The design of the FAD, HAT, and VAT is generally reasonable for operation on hydrodynamic performance and structural strength point of view in real sea.

In the operational and the survival condition, the rotational velocity of 75 RPM is significantly generated as the maximum pressure is increasing. Therefore the mechanical analysis is performed for the survival condition as shown in Figure 4.17. It can be seen that the maximum

Table 4.1: Deformation, stress, and strain at survival condition

Part	Deformation (mm)	Stress (N/mm2)	Strain (mm/mm)
FAD (aluminum)	0.023	0.32	6.58×10^{-5}
HAT (ABS)	3.1	1.76	9.25×10^{-4}
VAT (aluminum)	3.2	40.5	8.32×10^{-2}

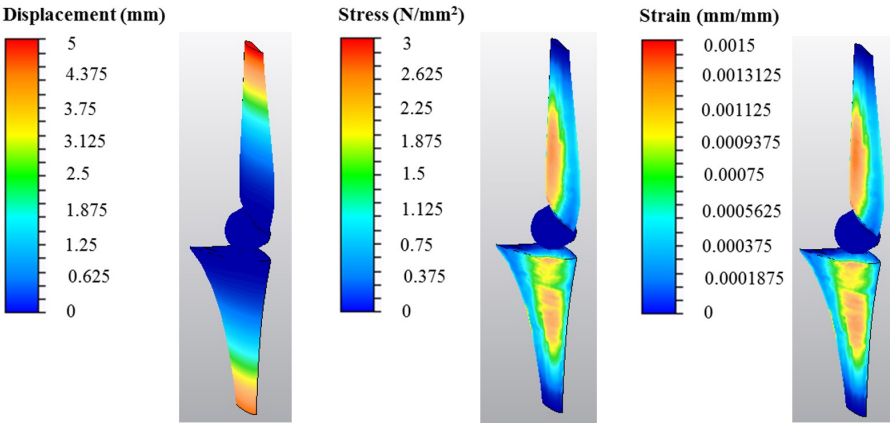

(a)

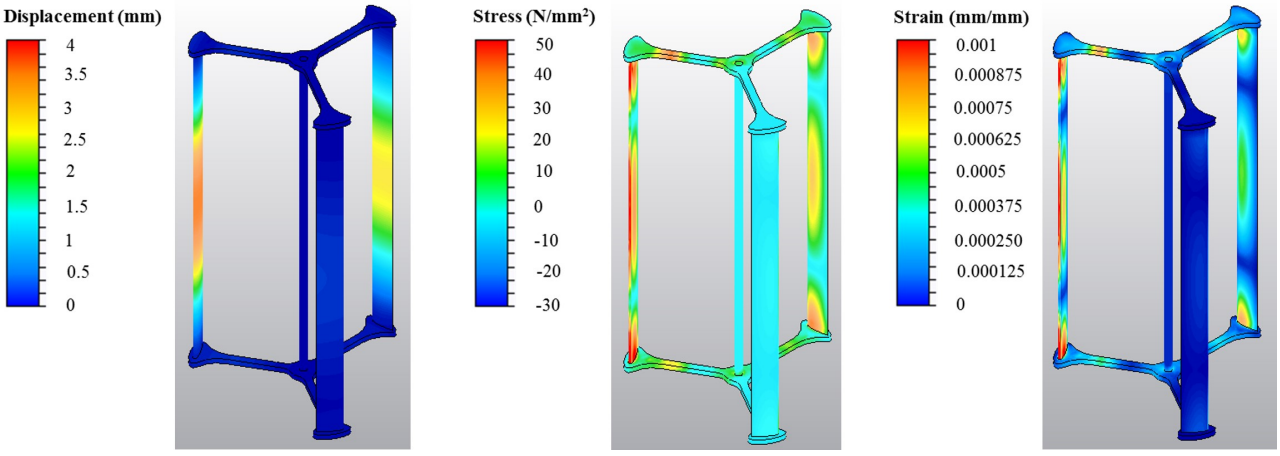

(b)

Figure 4.22: Mechanical response on (a) horizontal and (b) vertical axis turbine in survival condition

displacement of the turbine blade is about 3.1 mm at the blade tip of horizontal axis turbine and 3.2 mm at the blade mid-section of the vertical axis turbine. Despite the high magnitude of the blade displacement, it should be noted that the tidal current turbine is mounted on the FAD and then the structure deformation can be avoided. Under the survival condition, the maximum stress acting on the rotating rotor is occurred with highly stress at mid-section of the blade. Other critical locations can be observed at the blade tip connected to the top and the bottom plates. On the other hand, the tendency of the strain distribution is the same with the stress distribution. However the maximum stress and strain are still far below for the modulus of elasticity. This means that it is considerably safe to operate even if in the survival condition.

4.8.3 Reduction of Mooring Forces and Motions

Snap load often causes breaking force on mooring cable and also the FAD with a single point mooring system could be broken down with floating structure. The snap load can be frequently occurred when wave steepness is larger and then water level is suddenly exchanged. In this study, an elastic mooring system using a rubber cable is proposed as shown in Fig.4.8. In this section, the reduction effect of the snap load caused by wave and current is investigated in the elastic mooring case.

Fig.4.23(a) shows one example of time histories of the mooring force caused by the snap load due to wave in the chain mooring case of Model-A, whereas there is no snap load in the elastic one as shown in Fig.4.23(b). It can be found that the impulsive forces with spiky were clearly occurred during the short time and the maximum peak value in the snap load case is about four times larger than that in no-snap case. Fig.4.24 shows comparison of reduction ratio of the snap load with wave steepness H/λ in Model-A case. The vertical axis means the ratio of the averaged mooring force between the chain mooring case and the elastic mooring one. It can be seen that the maximum reduction ratio reaches nearby 30% and the averaged one is about 15%. The averaged mooring force in the elastic case is relatively lower than that in the chain case, especially when the wave steepness is larger. In this study, the elastic coefficient of the rubber was selected in advance to work well as mentioned in Sec.4.2. This indicates that

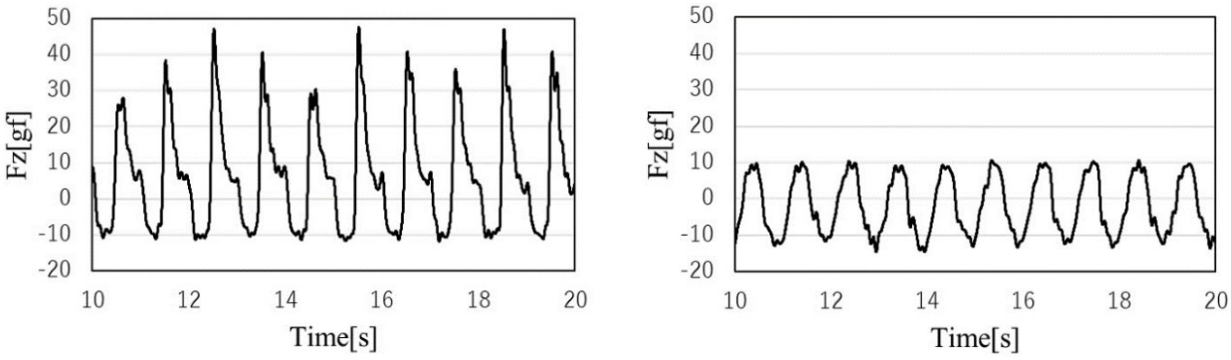

(a) with snap (b) without snap

Figure 4.23: Time history of mooring force in Model-A

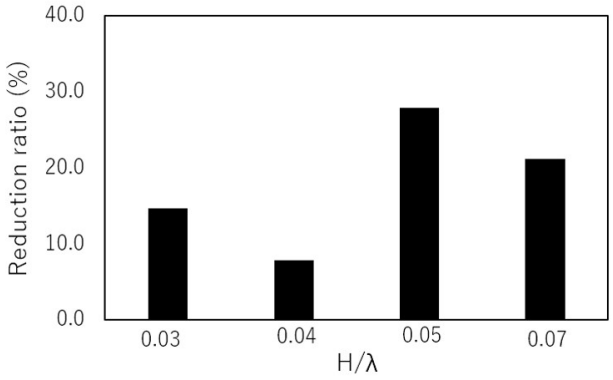

Figure 4.24: Reduction ratio of snap load with wave steepness H/λ

the elastic mooring for FAD is a useful technique for escaping an unexpected snap load and for reducing a mooring force. The elastic coefficient of the rubber should be optimized for a practical operation in future works. Votex Induced Vibration, VIV excited by Karman vortices around the FAD should be reduced in Model-A. The VIV is depend on Strouhal number which also consider the diameter of floater and the current velocity. In this study, the wider diameter is proposed in Model-B to escape from the VIV phenomena as shown in Fig.4.6.

Fig.4.25 shows one example of time histories in sway motion y/D at the center of the FAD, where D is the diameter of the FAD. The sway motion was recorded by the video camera (200fps) from the top view. The result indicates that the sway motion in Model-A is clearly generated by the VIV phenomena, in which Strouhal number is approximately 0.2. The vibrated amplitude y/D is about 0.5 in this case and the maximum one reaches to y/D=1.0. On the other hand, in Model-B, the time history is in stable state without vibration due to the VIV.

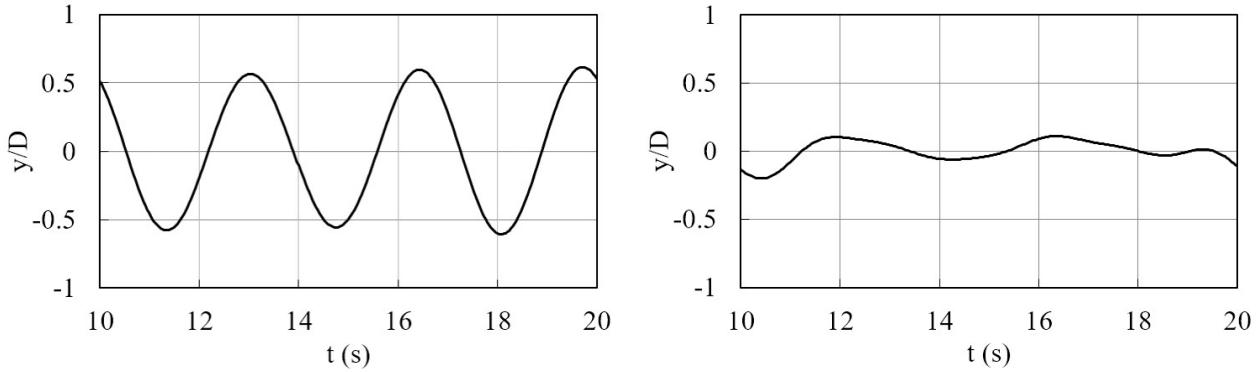

(a) Model-A (b) Model-B

Figure 4.25: Example of time history of sway motion of FAD at $U = 0.2$m/s

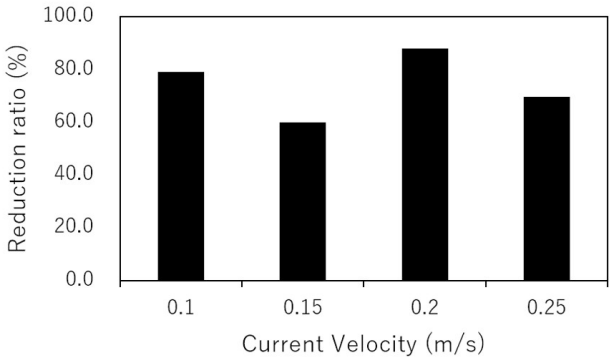

Figure 4.26: Reduction ratio of sway motion in Model-B

Fig.4.26 shows reduction ratio of sway motion in Model-B. The vertical axis means the ratio between sway motion in Model-A and that in Model-B. It can be seen that the maximum reduction ratio is about 80% or more and the averaged one is about 60%. The result indicates that Model-B can perfectly reduce the sway motion in the current condition and also the stable condition can be kept with no-vibration even if at a single point mooring system. Figs.4.27 and 4.28 show reduction ratio of surge and heave motions in Model-B in wave and wave-current conditions. Both surge and heave motions can be reduced in Model-B and the averaged value is approximately 50%. These results imply that the water line of the FAD with the single point mooring system is one the key parameters to reduce their motions in wave, current and wave-current conditions, and it should be optimized at each focused installation sea. However, the reduction ratio of the heave motion is less than 30% in wave-current conditions, which is not so good performance comparing with those in sway and surge motions. This is because the horizontal velocity component excited by wave-current is stronger and then the vertical one is

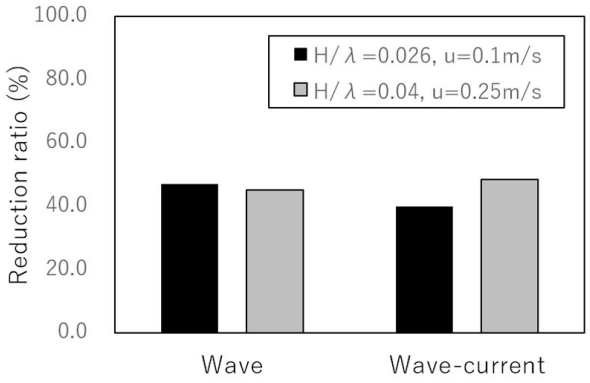

Figure 4.27: Reduction ratio of surge motion in Model-B

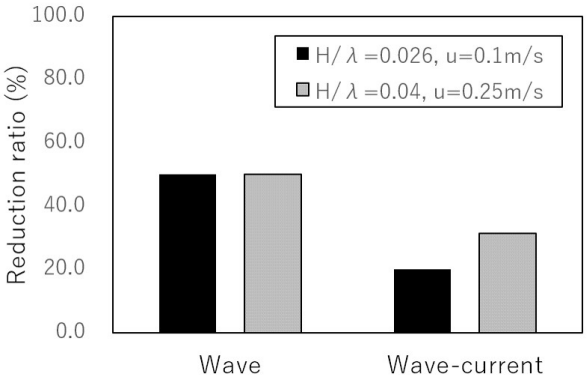

Figure 4.28: Reduction ratio of heave motion in Model-B

relatively smaller than that at the other cases. Therefore, the heave amplitudes are not so large different in both Model-A and Model-B. The results in this section concludes that Model-B with the elastic mooring can reduce the snap load caused by impact force and motions such as heave, sway and surge in wave, current and wave-current conditions. These techniques are useful for designing the FAD. In future efforts, the optimized design of the FAD should be required at focused site in real sea condition.

4.9 Electric Performance of The Designed Turbine inside FAD

4.9.1 Validation and Optimization

As explained in Sec.4.3, the horizontal and vertical axis current turbines are employed, NREL S814 for HAT and NACA0018 for VAT, respectively. Before conducting optimization of turbine for hydrodynamic performance using Blade Element Momentum theory, the basic performance of lift force is validated with the experimental data[29][30] [31].

Fig.4.29 shows comparison of coefficient of lift force, C_L with angle of attack (AoA) for NREL S814 at Reynold's number, Re=1.6×10^5 and 3.2×10^5 and for NACA0018 at Re=8×10^4 and 1.4×10^5. These conditions for each hydrofoil are selected as a designed velocity. The tendency

of C_L is in good agreement with the experimental data at each case. There is a little discrepancy with them. This is because BEM theory cannot consider viscosity effect, and thus some conditions cannot be coincided with the experimental one. But this theory can be used to design a suitable turbine at a focused area in a preliminary optimization process. In this study, NREL S814 for HAT can be chosen with AoA = 8°, C_L = 0.6 and C_L/C_D = 81.409 to avoid dynamic stall and NACA0018 for VAT is also selected with AoA =7°, C_L = 0.9 and C_L/C_D = 37.25. To apply the selected hydrofoils into turbines and to estimate the produced

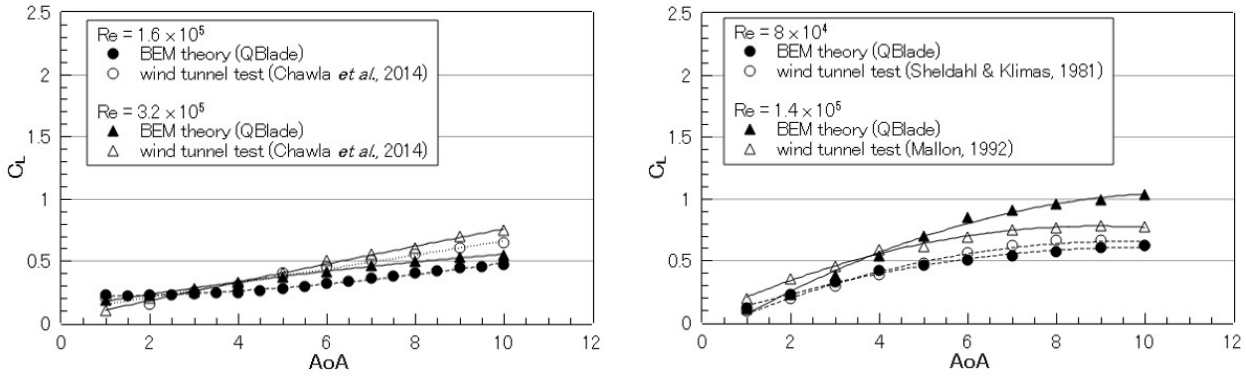

(a) NREL S814 (b) NACA 0018

Figure 4.29: Comparison of lift coefficient with AoA

electric power, the important design parameters for HAT and VAT are selected as shown in Table 4.2 and Table 4.3, while the relationship between the chord length and the twist for HAT is presented in Fig.4.30. In this study, the HAT is optimized to operate at Tip Speed Ratio, TSR=5 while the VAT is designed to operate when TSR=3. Fig.4.31 shows the estimated power coefficient, C_P of the designed turbine with the tip speed ratio for each type. It can be found that the maximum C_P is 0.42 at TSR=5 in Type B for the HAT and also that that one is 0.52 at TSR=3 in Type A for the VAT, comparing with the other types. Therefore, both types under these conditions can be applied as a suitable turbine for the FAD at an archipelago area with active aquacultures as shown in Sec.4.3.

Table 4.2: Design parameters at three different types of NREL S814 for HAT

Parameter	Type A	Type B	Type C
Hydrofoil	NREL S814	NREL S814	NREL S814
Max. chord length (m)	0.188	0.2	0.29
Rotor radius (m)	0.5	0.5	0.5
Optimum AoA	8°	9°	10°
Number of blade (N)	2	2	2

Table 4.3: Design parameters at three different types of NACA0018 for VAT

Parameter	Type A	Type B	Type C
Hydrofoil	NACA 0018	NACA 0018	NACA 0018
Blade span (m)	0.7	0.7	0.7
Chord length (m)	0.065	0.08	0.1
Rotor radius (m)	0.3	0.3	0.5
Number of Blade	3	3	3

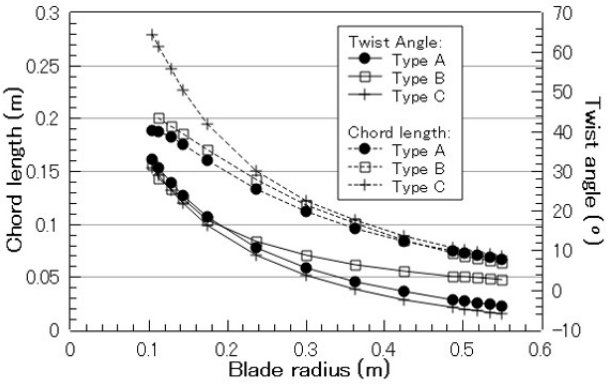

Figure 4.30: Comparison of chord length and twist angle with blade radius at each designed HAT

4.9.2 Power Estimation

In this study, in order to produce environment-friendly ecosystem by an artificial infrastructure, it can be supposed that the FAD with an ocean energy harvester can be installed at an archipelago area with active fishery and aquacultures. Therefore, the electric power generated by an ocean energy harvester inside the FAD as a scientific platform can be utilized with ocean environmental sensors for real time monitoring, e.g underwater camera, echo-sounders, acoustic receivers, coded tag etc. in real sea state. Furthermore, the electric demand for ocean environmental sensors is estimated at the archipelago area. The rotational speed of the turbine should be set to less than 75rpm considering ocean environment at the archipelago area. The HAT is

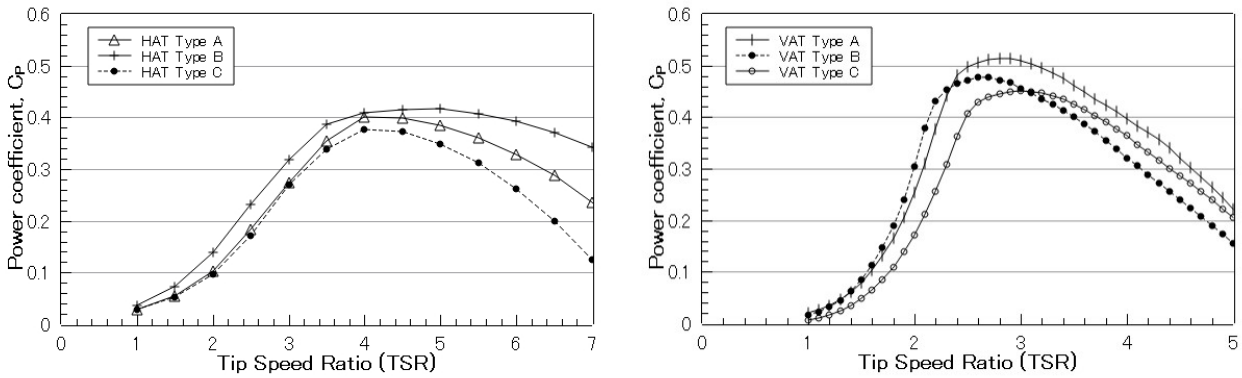

(a) HAT (b) VAT

Figure 4.31: Power coefficient of designed turbine with tip speed ratio at each type

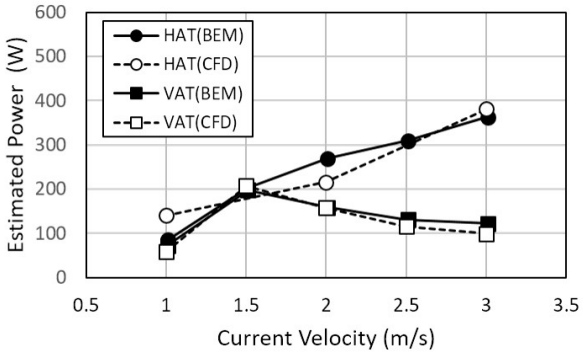

Figure 4.32: Estimated power of the designed turbine at each current condition

designed to operate at the current velocity 2m/s, while the VAT is proposed to be implemented at the lower velocity 1.5m/s. Using the computational fluid analysis as shown in Sec.4.5, the electric power generated by the designed turbine can be estimated based on eq.4.18[32] with BEM theory as below:

$$P = T \cdot \omega = \frac{T \cdot \pi \cdot n}{30} \tag{4.18}$$

where T is torque, n is the revolutions per minute (rpm), and ω is the angular velocity of turbine. Fig.4.32 shows the estimated power of the designed turbine at each current velocity in real scale, which means the theoretical maximum efficiency. The results estimated by BEM theory is overall agreement with those by CFD results with a coefficient of viscosity effect but there is small discrepancy with them because BEM theory is based on the potential theory, and therefore the viscosity effect and turbulent flow cannot be considered. However, the tendency of the electric power can be estimated in both turbines. The maximum powers are reached

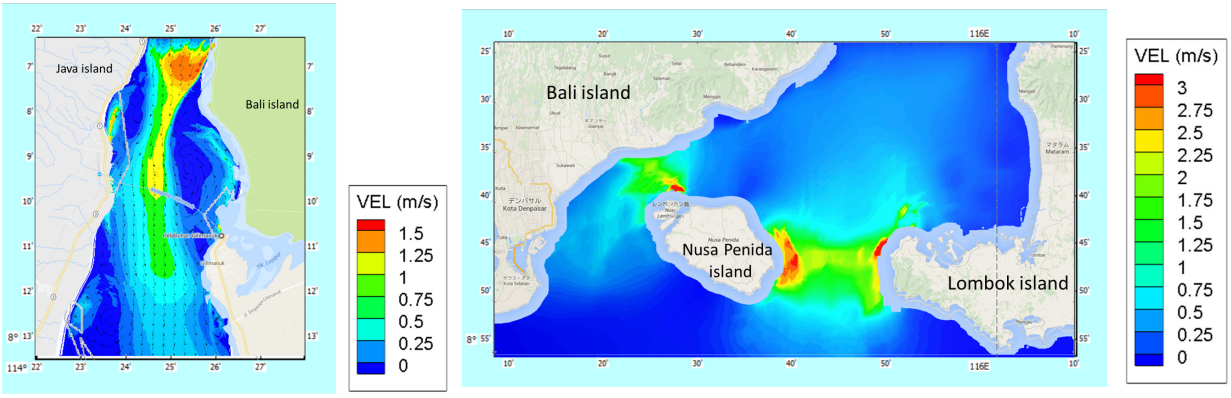

(a) Bali strait (b) Lombok strait

Figure 4.33: Tidal current distribution computed by ocean circulation model[33] in a typical archipelago area with active fishery and aquacultures in Indonesia

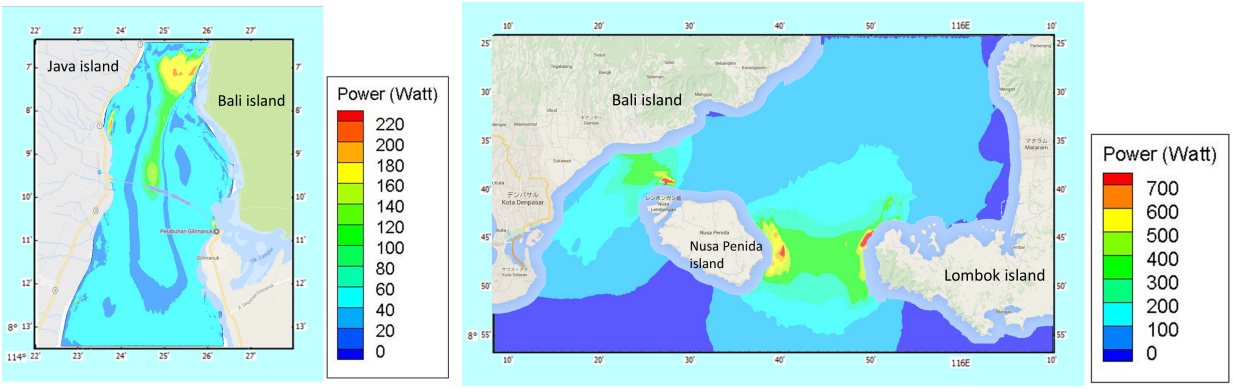

(a) FAD with VAT in Bali strait (b) FAD with HAT in Lombok strait

Figure 4.34: Distribution of estimated electric power generated by the designed turbine

to be about 360W for HAT at 3m/s and 200W for VAT at 1.5m/s, respectively. For the minimum operating velocity, 1 m/s, the estimated powers are approximately 100W for HAT and 65W for VAT, respectively. The estimated electric power could be adequate to turn on LED for gathering fishes and to boot up and activate several sensors such as beacon, ocean environmental, disaster and security devices. In near future effort, the power coefficient should be validated with a field data and then some efficiencies regarding with loss of gear, generator etc. should be considered in practical use.

The designed turbines for HAT and VAT are applied to one of the typical archipelago area with active fishery and aquacultures, Bali strait and Lombok strait in Indonesia where our previous numerical research[33] has been already conducted by using ocean circulation model to examine ocean circulation and to estimate potential of tidal current energy in whole Indonesian sea.

Fig.4.33 shows one snapshot of the tidal current field in Bali strait and Lombok strait. The distributions of estimated power generated by the optimized turbines, HAT and VAT are shown in Fig.4.34. In Bali strait, the maximum tidal current velocity is about 1.5m/s at the northern part where the width of strain between Java and Bali islands is narrowest. The maximum power reaches about 220W using the VAT. It means that the northern part at Bali strait could be a suitable installation site for the FAD with the VAT to generate electric power. On the other hand, in Lombok strait, the mean current velocity is about 2m/s and the maximum one is about 3m/s, especially at the narrow region between Nusa Penida and Lombok islands. The maximum electric power can be estimated to be about 700W. This indicates that the FAD with the HAT could operate with its optimum performance in this focused strait.

4.10 Conclusions

This study has proposed and designed a new type of Fish Aggregating Device (FAD) with an ocean energy harvester in order to generate independent electric power for several sensors such as beacon, ocean environmental, disaster and security devices, especially at an archipelago area with aquacultures where the FAD can be utilized as a scientific platform to produce environment-friendly ecosystem by an artificial infrastructure. The proposed FAD with ocean energy harvester is one of the useful options having an individual electric power platform and fulfilling energy supply for many archipelago areas with fishery and aquacultures. The main conclusions can be summarized by experimental, numerical and theoretical works as follows.

A mooring type of FAD with Horizontal Axis Turbine (HAT) and Vertical Axis Turbine (VAT) was designed considering collision with a marine vertebrate, fish and a rotational turbine. To investigate characteristics of fluid force and motion of the FAD caused by snap load and Vortex-induced Vibration (VIV), the experimental and numerical works were performed with the theoretical work in wave, current and wave-current conditions. The elastic mooring can achieve 15% reduction for the averaged snap load and 30% for the maximum one. The modified FAD with the wider draft line can reduce motions such as surge, sway and heave excited by VIV

in wave-current condition, whose reduction rate is approximately 50% or more, especially in sway motion. The flow field around the FAD and the rotational turbine in 3D can be computed by CFD and also the results in the fluid force are overall agreement with the experimental and the theoretical ones. The flow field is almost uniform at the lower part of the FAD and then the flow field around the turbine inside the FAD are not affected by the frame of the FAD at the upstream side. On the other hand, at the upper part of the FAD in the downstream side, the complicated flow field can be generated with pressure fluctuation, and thus a vibration energy harvester can be attached on the frames of the FAD to generate electric power from wave and current conditions. The electric power generated by the optimized blades of HAT and VAT was estimated. The maximum electric power reaches about 200W for VAT and 360W for HAT. In Indonesian archipelago area, the estimated electric power could reach 220W in Bali strait and 700W in Lombok strait, due to higher current velocity, by using the mooring type of FAD with the designed turbine. It could be adequate to turn on LED for gathering fishes and to boot up and activate several sensors such as beacon, ocean environmental, disaster and security devices.

The first model of the FAD without a turbine was build up and has been tested in real ocean field to survey fluid force on the FAD and its motions and to investigate structural problems such as fatigue, buckling and yield load due to wave and current conditions including severe sea state since 2015 as shown in Fig.4.35. The size of the FAD is 1.5m diameter and 5.4m height. The installation site is 26°39' North Latitude and 128°34' East Longitude, 27km offshore near Okinawa island, where fishery and aquaculture are quite active in Japan. The water depth is approximately 1000 m. The FAD was designed on the basis of theoretical, numerical and experimental works for wave and current conditions in real sea. The FAD was mainly constructed by the aluminum frame and the ABS floaters. The FAD as a scientific platform has been working near sea surface and moored by anchor at seabed in this site. In near future effort, some ocean energy converters will be installed on the second prototype model of FAD. There is a great need for this kind of field test to investigate environmental effects, particularly sea-cage fish farms, and to manage environment-friendly ecosystem without accidental events related with interaction between the FAD and wild fishes. In future effort, unsteady motions of FAD with an ocean energy harvester should be directly considered in theoretical and numerical

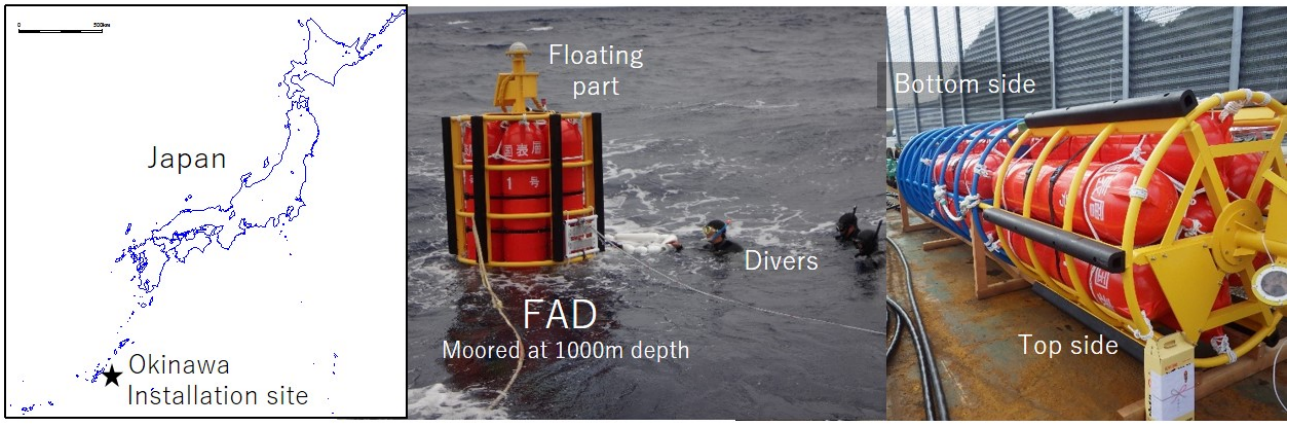

Figure 4.35: First prototype of FAD installed near Okinawa island in Japan

works to investigate fully nonlinear fluid-structure interaction. The power coefficient should be also validated with field data and then some efficiencies regarding with loss of gear, generator etc. should be considered in practical use.

Bibliography

[1] Marianne Robert, Laurent Dagorn, Jean Louis Deneubourg, David Itano, and Kim Holland. Size-dependent behavior of tuna in an array of fish aggregating devices (FADs). *Marine Biology*, 159(4):907–914, 2012.

[2] Tim Dempster and Marc Taquet. Fish aggregation device (FAD) research: Gaps in current knowledge and future directions for ecological studies, 2004.

[3] G. Moreno, L. Dagorn, M. Capello, J. Lopez, J. Filmalter, F. Forget, I. Sancristobal, and K. Holland. Fish aggregating devices (FADs) as scientific platforms. *Fisheries Research*, 178:122–129, 2016.

[4] Adam Westwood. SeaGen installation moves forward. *Renewable Energy Focus*, 9(3):26–27, 2008.

[5] Asif Kabir, Ivan Lemongo-tchamba, and Arturo Fernandez. An assessment of available ocean current hydrokinetic energy near the North Carolina shore. *Renewable Energy*, 80:301–307, aug 2015.

[6] J. King and T. Tryfonas. Tidal stream power technology - state of the art. *Oceans 2009-Europe*, (2):1–8, 2009.

[7] Hiromichi Akimoto, Kenji Tanaka, and Kiyoshi Uzawa. A conceptual study of floating axis water current turbine for low-cost energy capturing from river, tide and ocean currents. *Renewable Energy*, 57:283–288, 2013.

[8] Fengmei Jing, Qihu Sheng, and Liang Zhang. Experimental research on tidal current vertical axis turbine with variable-pitch blades. *Ocean Engineering*, 88:228–241, 2014.

[9] Liang Zhang, Shu-qi Wang, Qi-hu Sheng, Feng-mei Jing, and Yong Ma. The effects of surge motion of the floating platform on hydrodynamics performance of horizontal-axis tidal current turbine. *Renewable Energy*, 74:796–802, feb 2015.

[10] Katsutoshi Shirasawa, Kohei Tokunaga, Hidetsugu Iwashita, and Tsumoru Shintake. Experimental verification of a floating ocean-current turbine with a single rotor for use in Kuroshio currents. *Renewable Energy*, 91:189–195, 2016.

[11] Peter E. Robins, Simon P. Neill, and Matt J. Lewis. Impact of tidal-stream arrays in relation to the natural variability of sedimentary processes. *Renewable Energy*, 72:311–321, 2014.

[12] Marshall C Richmond, John A Serkowski, Laurie L Ebner, Mirjam Sick, Richard S Brown, and Thomas J Carlson. Quantifying barotrauma risk to juvenile fish during hydro-turbine passage. *Fisheries Research*, 154:152–164, 2014.

[13] Weichao Shi, Mehmet Atlar, Roslynna Rosli, Batuhan Aktas, and Rosemary Norman. Cavitation observations and noise measurements of horizontal axis tidal turbines with biomimetic blade leading-edge designs. *Ocean Engineering*, 121:143–155, 2016.

[14] Fergal O. Rourke, Fergal Boyle, and Anthony Reynolds. Marine current energy devices: Current status and possible future applications in Ireland. *Renewable and Sustainable Energy Reviews*, 14(3):1026–1036, 2010.

[15] Hidemi Mutsuda, Ryuta Watanabe, Masato Hirata, Yasuaki Doi, and Yoshikazu Tanaka. Elastic Floating Unit With Piezoelectric Device for Harvesting Ocean Wave Energy. page 233. ASME, 2012.

[16] Hidemi Mutsuda, Ryuta Watanabe, Shota Azuma, Yoshikazu Tanaka, and Yasuaki Doi. Ocean Power Generator Using Flexible Piezoelectric Device. page V008T09A002. ASME, 2013.

[17] M. Rafiuddin Ahmed. Blade sections for wind turbine and tidal current turbine applications-current status and future challenges. *International Journal of Energy Research*, 36(7):829–844, 2012.

[18] S. Kiho, M. Shiono, and K. Suzuki. The power generation from tidal currents by darrieus turbine. *Renewable Energy*, 9(1-4):1242–1245, 1996.

[19] Ryan Gerakopulos, Michael S H Boutilier, and Serhiy Yarusevych. Aerodynamic Characterization of a NACA 0018 Airfoil at Low Reynolds Numbers. *40th Fluid Dynamics Conference and Exhibit*, (July):1–13, 2010.

[20] Andi Ardianti, Hidemi Mutsuda, Kento Kawawaki, Shunsuke Fujii, and Yasuaki Doi. Numerical Simulation of a Strongly Interaction between Tsunami wave and Obstacles Using Particle Based Method. In *Proc. of the 3rd International Conference on Violent Flows, 9-11, March 2016, Osaka, Japan*, pages 9–11, Osaka, Japan, 2016. VF-2016.

[21] D. Kavetski, F. Fenicia, and H. H. G. Savenije. A flexible multi-model framework for catchment-specific calibration, and application to diverse European catchments. In *Geophysical Research Abstracts, EGU General Assembly 2010*, 2010.

[22] Autodesk. Autodesk CFD Motion 2016, 2016.

[23] F. R. Menter. Two-equation eddy-viscosity turbulence models for engineering applications. *AIAA Journal*, 8(32):1598–1605, 1994.

[24] National Association of Fisheries Infrastructure. *Guidance of design for ports and fisheries supervised by Fisheries Agency (in Japanese).* 2003.

[25] D Marten, J Wendler, G Pechlivanoglou, C. N Nayeri, and C. O Paschereit. QBlade : An Open Source Tool for Design and Simulation of Horizontal and Vertical Axis Wind Turbines. *International Journal of Emerging Technology and Advanced Engineering*, 3(3):264–269, 2013.

[26] H Glauert. Airplane Propellers. In *Aerodynamic Theory: A General Review of Progress Under a Grant of the Guggenheim Fund for the Promotion of Aeronautics*, pages 169–360. Springer Berlin Heidelberg, Berlin, Heidelberg, 1935.

[27] W. X M Koh and E. Y K Ng. Effects of Reynolds number and different tip loss models on the accuracy of BEM applied to tidal turbines as compared to experiments. *Ocean Engineering*, 111:104–115, 2016.

[28] Robert Gasch and Jochen Twele. Blade geometry according to Betz and Schmitz. In Robert Gasch and Jochen Twele, editors, *Wind Power Plants: Fundamentals, Design, Construction and Operation*, pages 168–207. Springer Berlin Heidelberg, Berlin, Heidelberg, 2012.

[29] Jasvipul S. Chawla, Shashikanth Suryanarayanan, Bhalchandra Puranik, John Sheridan, and Brian G. Falzon. Efficiency improvement study for small wind turbines through flow control. *Sustainable Energy Technologies and Assessments*, 7:195–208, 2014.

[30] Paul C. Klimas Robert E. Sheldahl. Aerodynamic Characteristics of Seven Sysmmetrical Airfoil Sections Through 180-Degree Angle of Attack for Use in Aerodynamic Analysis of Vertical Axis Wind Turbines. *SAND80-2114*, (1):1–5, 1981.

[31] K J Mallon. The NACA 0018-64 Aerofoil at Low Reynolds Numbers with Application to Vertical Axis Wind Turbines - Including Turbulence Stimulation, 1992.

[32] Halliday and Resnick. *Fundamental of Physics 10th Edition*, volume 1. 2015.

[33] Shade Rahmawati, Hidemi Mutsuda, Yasuaki Doi, Hidemi Mutsuda, and Yasuaki Doi. Numerical Estimation for Tidal-Current Energy Resources in Indonesia. In , editor, *Proceedings of the Twenty-sixth (2016) International Ocean and Polar Engineering Conference*, volume 1, pages 519–527, Rhodes, nov 2016. International Society of Offshore and Polar Engineers (ISOPE).

Chapter 5

Numerical Model on Restoration of Ocean Environment using Steelmaking Slag

5.1 Steelmaking Slag in Ocean Restoration

Enclosed sea areas with a complicated geometry and a variety of marine environments in Japan have been significantly affected by anthropogenic impact during last five decades. Many industries are built up at coastal region surrounding enclosed sea and also urbanizations are rapidly increasing. In addition, reclamation and some dredges were required for progressing in industry and urban development, which caused serious environmental issues and wide range of marine environments in enclosed sea areas. For example, in northern part of Tokyo Bay, there are many dredging trenches covered by bottom sludge, where oxygen solubility is decreased, especially in summer and causing hydrogen sulfide (H_2S) generation. In recent years, oxygen deficiency caused by decomposition of organic matter in bottom sediment is occurred thus the blue tide is annually induced. Therefore, dredging trench could be source point of oxygen deficient water which often cause the blue tide when northeastern wind is blowing [1][2][3].

Due to worse environment in enclosed sea, Council for Transport Policy of Japan's Ministry of Land, Infrastructure, Transport and Tourism has announced a basic plan of a future port environment policy for practical use of recycled materials such as soil and sand dredge from port and harbor, especially in enclosed sea [4]. Considering Status of the London Convention on the Prevention of Marine Pollution by Dumping of Wastes and Other Matter (1972) and the Protocol Thereto (1996), in Japan, the Ministry of Land, Infrastructure, Transport and Tourism has proposed practical use of industrial products and recycled materials including slag because the use of natural mountain sand or crushed stone is not desirable from the viewpoint of the natural environment protection [5]. Ministry of the Environment also showed water environment improvement technology for enclosed coastal seas field using steelmaking slag [6]. These efforts could also make an important contribution to reduce CO_2 emission.

Under this background in recent social requirement, steelmaking slag has been employed from production of steelmaking, which is about 15 million tons/year. Steelmaking slag has been used for social infrastructure construction such as roadbed material, coarse aggregate in concrete, as a component of raw material of cement in civil engineering field. Since 1993, Nippon Slag Association in Japan has been involved in application technology research for the use of steelmaking slag as a material for ground improvement in port and harbor construction [7]. JFE steel corporation in Japan manufactured artificial reefs for Marine block using carbonated steel slag in order to help a great breeding habitats for seaweeds and coral [8]. In recent year, steelmaking slag including high amount of iron has been utilized to recover shore protection and to improve sea bottom sediment [9]. Some research works have been undertaken during last two decades to promote useful practical use of special characteristics of steelmaking slag in enclosed sea environments. Many studies have investigated that slags are useful for removing phosphate and H_2S and for releasing iron in order to produce growth of seaweeds [10][11]. The process and mechanisms of solidification of steelmaking slag at tideland have been investigated and also dredged soil was added to the slag to examine whether it would prevent solidification [12]. More recent works have focused on iron content of steelmaking slag, rocky shore denudation measures and bottom sediment improvement measure in enclosed sea by using Fe ions eluted from steelmaking slag [13][14]. For example, it was examined that steelmaking slag is a useful

material for remediation of organically enriched sediments in enclosed sea areas to suppress H_2S in the field experiment at Fukuyama inner harbor [15][16] and Kawasaki port [17]. The review paper showed the research progress of steel slag utilization [18].

In this study, a numerical model is proposed and developed with considering fluid-particle interaction between ocean circulation and steelmaking slag to investigate advection-diffusion of dissolved sulfide based on the results in the field experiment[15][16]. The model is also applied to Fukuyama inner harbor and Tokyo Bay, where H_2S is highly toxic and fatal to benthic organisms and it causes oxygen-deficient water and the blue tide. This study shows effectiveness and usefulness of steelmaking slag for improving organically enriched sea bottom in enclosed sea.

5.2 Overview of Field Experiment

To reduce dissolved sulfide and suppression of formation of hydrogen sulfide gas, the previous field experiment has been confirmed by JFE Steel Corporation West Japan Works since 2011[16]. The steelmaking slag was covered on sediment including silty and organic matter in Fukuyama inner harbor with 2200m Length × 100m Width × 2m Depth as shown in Fig. 5.1. The right figure shows the horizontal plane and vertical section with monitoring points for measuring water quality at the inner harbor. In this harbor, the capacity of sewage treatment plant at the head of inner harbor is over and the untreated sewage including organic matter is sometimes flushed when the heavy rainfall exceeds the holding capacity. Sulfate-reducing bacteria could generate H_2S and toxic compound with stinking. The properties of the sediment on the bottom in the inner harbor can be seen in [16]. In 2011, the first construction was conducted at Site A with area 432m^2. The fine steelmaking slag with particle size 5-10mm was located and next the coarse slag with the size 10-25mm was placed. The second construction was also constructed at the neighboring location of Site B with area 2620m^2 and Site C with area 890m^2 in 2012. The slag with particle size 30-50mm was also used with the above mentioned slag. The total thickness of the covered slag is about 0.7m on the silty sediment. These conditions such as slag

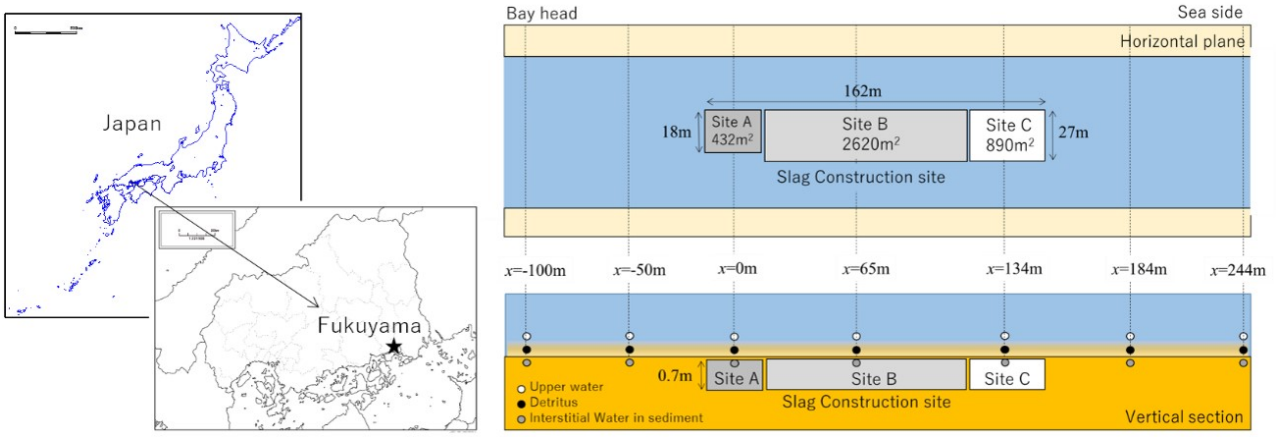

Figure 5.1: Field experimental site at Fukuyama inner harbor.

size, covered area and thickness are considered in numerical model as mentioned in the next section. The chemical composition of the steelmaking slag can be found in [16]. Some important parameters such as water quality, gas and benthos were monitored after the construction at the distance x=-100, -50, 0, 65, 134, 184 and 244m from the center of Site A, where there are three vertical observed points to monitor and analyze dissolved sulfide.

5.3 Numerical Model

The present study employs two different scale models. One is based on 3D Eulerian-Lagrangian model [19] to compute fluid-particle interaction among soil, slag and tidal flow in local area. The other one is quasi-3D Ocean Circulation Model based on Princeton Ocean Model, POM [20] to compute advection-diffusion of dissolved sulfide in global area. Both models can be coupled at sea bottom boundary condition in global area, where steelmaking slag is covered.

5.3.1 Eulerian-Lagrangian Model for Local Area

In local area, to compute multiphase flow considering fluid-particle interactions among soil, slag and water including water surface, Eulerian-Lagrangian model [19] is employed by using both Lagrangian marker particles and density function as shown in Fig. 5.2. In this section, firstly, the grid based method is introduced to compute fluid flow such as current in ground

water and water elevation in global area and next the particle based method is explained to compute behaviors of soil and sand in local area.

Governing Equations

The governing equations in this model are incompressible Navier-Stokes equation, the conservation of mass and equation of the density function ϕ_I for Ith phase (Air phase : I=1, Water phase : I=2, Solid phase such as soil and slag : I=3) given by

$$\frac{\partial u_i}{\partial x_i} = 0 \tag{5.1}$$

$$\frac{\partial u_i}{\partial t} + u_j \frac{\partial u_i}{\partial x_j} = -\frac{1}{\rho}\frac{\partial P}{\partial x_i} + \frac{\mu}{\rho}\frac{\partial^2 u_i}{\partial x_i \partial x_j} + F_e \tag{5.2}$$

$$\frac{\partial \phi_I}{\partial t} + u_j \frac{\partial \phi_I}{\partial x_j} = 0 \tag{5.3}$$

$$\frac{\partial C}{\partial t} + u_j \frac{\partial C}{\partial x_j} = K_h \left(\frac{\partial^2 C}{\partial x^2} + \frac{\partial^2 C}{\partial y^2} \right) + K_z \frac{\partial^2 C}{\partial z^2} + S_{in} + S_{out} + S_{ca} \tag{5.4}$$

where u is the velocity, μ is the coefficient of viscosity for each phase, ρ is the density for each phase, P is the pressure, F_e is the external forces such as gravity acceleration and the surface tension, C is the concentration of dissolved sulfide, K_h and K_z are the coefficients of horizontal and vertical diffusion, S_{in} and S_{out} are the inlet/outlet terms, and S_{ca} is the chemical reaction term which will be explained later. To consider physical properties representing different materials, the density function ϕ_I $(0 \leq \phi_I \leq 1)$ is defined as below:

$$\phi_I = \begin{cases} 1 & \text{if occupied} \\ 0 & \text{if otherwise} \end{cases} \tag{5.5}$$

This density function can be used to distinguish several different phases such as water, air and solid representing soil and steelmaking slag. The density function for each phase can be computed by eq.(5.3) with Navier-Stokes equation. Using the density function, the density and

the coefficient of viscosity can be defined as follows:

$$\rho = \sum_{I=1}^{3} \rho_I \phi_I \tag{5.6}$$

$$\mu = \sum_{I=1}^{3} \mu_I \phi_I \tag{5.7}$$

where ϕ_I is the density function defined by eq.(5.5).

Arrangement of Grids and Particles

The staggered MAC grid system is used to compute velocity, density coefficient of viscosity and pressure as shown in Fig. 5.2. The density function ϕ_I is defined on Eulerian grid to capture sea surface and ground water surface, and then it is stored at nodes of a grid. In this study, this model can be used in both fluid phase and soil one because the sediment area including slag is always submerged in the water for evaluating concentration of dissolved sulfide on this advection-diffusion problem. The velocity components are defined on cell faces of a grid. The pressure is defined at the center of each grid and also density and viscosity are defined at the same position. On the other hand, Lagrangian particles are defined to represent steelmaking slag, sand, gravel and silty sediment related with particle size, drag and permeability. To capture deformation of bottom topography caused by tidal current, Lagrangian particles can be tracked by velocity on Eulerian grid. The density function ϕ_p is defined on all particles to keep physical properties such as density, viscosity, radius, permeability and eluted concentration, which is interpolated by the density function ϕ_I defined on Eulerian grid. Therefore, the range of the value can be defined by $0 \leq \phi_p \leq 1$. The first order explicit is employed in time discretization and then the fractional step is employed to advance velocity and pressure in time integration.

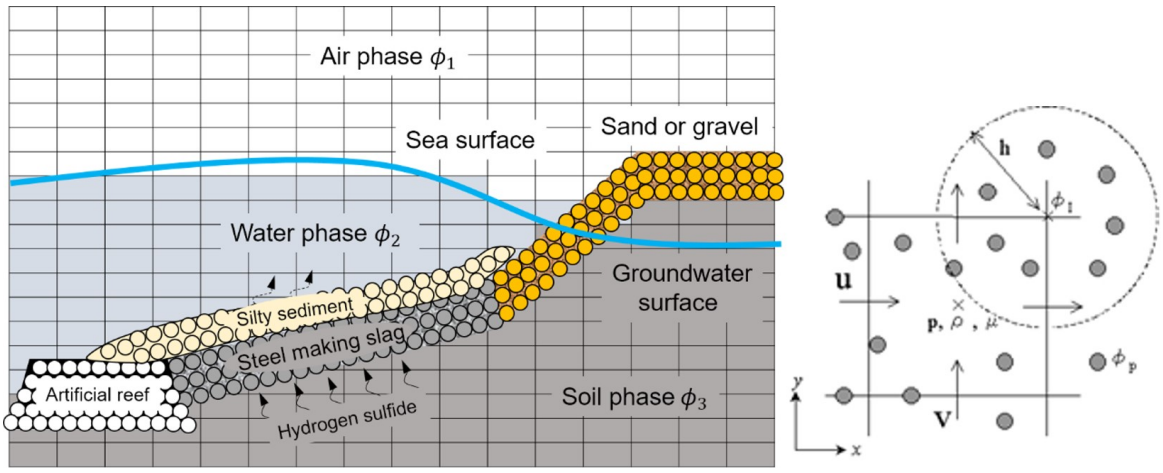

Figure 5.2: Arrangement of grids and particles in computational domain (Left: Definition of density function and particles, Right : Staggered grid system)

Numerical Algorithm

The governing equations are solved using time-splitting method. It is well known that the technique is suitable for solving a multi-phase flow without numerical diffusion and smearing. The advection step is calculated by CIP method [21], which is the third order accuracy in time and space, and also it is a less diffusive and stable algorithm for solving the advection term in eqs.(5.2)-(5.4). The spatial profile of density function between neighboring grids is approximated with a cubic interpolated function. The non-advection step can be computed using the second-order finite difference method and Poisson equation for pressure with specified jump conditions can be used as below:,

$$\nabla\left(\frac{\nabla P^{n+1}}{\rho^*}\right) = \frac{\nabla u^*}{\Delta t} \tag{5.8}$$

where * denotes the physical value after advection step. More details can be seen in [19] and [21].

The particle velocities $\overrightarrow{u}(\overrightarrow{x}_p)$ are interpolated from velocities on underlying grids. Furthermore the density function ϕ_p on lagrangian particle is interpolated from the density function ϕ_I on nodes of grids. In this model, the bilinear or the trilinear interpolation are used with high accuracy and efficiency. Since the velocity on cell faces can be replaced in unsteady flow problem, the interpolation procedure is performed at every time step. Lagrangian particles

representing steelmaking slag and sediment defined previously, can be moved in water phase and then they can be tracked by evolution equation as follows:

$$\frac{d\overrightarrow{x}_p}{dt} = \overrightarrow{u}(\overrightarrow{x}_p) \tag{5.9}$$

where $\overrightarrow{x}_p$ is the particle location, $\overrightarrow{u}(\overrightarrow{x}_p)$ is the particle velocity at $\overrightarrow{x}_p$. The particles having density function ϕ_p is separately integrated forward in time. This equation is integrated using the fourth order accurate Runge-Kutta method. The particle velocity $\overrightarrow{u}(\overrightarrow{x}_p)$ is interpolated from velocity on neighboring cell faces of Eulerian grids as mentioned in the next section.

A methodology for reconstructing an interface is employed using Lagrangian particles. The error of density function ϕ_I defined on nodes of grids can be corrected by using neighboring particles within interaction region with radius h. The smoothing approximation of density function ϕ_I can be constructed by utilizing a kernel function in SPH method [22]. This approximation is commonly known and used in particle based method. The interpolation technique in a meshfree method can be considered as a discretization that uses a set of particles to approximate continuum without grid. The averaging operator is usually defined as

$$\varphi_i = \sum_{j=1}^{N} m_j \frac{\varphi_j}{\rho_j} W_{ij} \tag{5.10}$$

where φ_i is the physical value, m_j is the mass, ρ_j is the density and W_{ij} is the spatial filter as a kernel function of spatial variables. N denotes number of particles which means set of neighboring particles that are closer than interaction radius h. Based on SPH method using a kernel function, the density function ϕ_I defined on nodes of grid can be corrected using density function ϕ_p for each particle within referenced area with a radius h as follows:

$$\phi_I' = max\left(\phi_I, \sum_{j=1}^{N} \phi_p \frac{m_p}{\rho_p} W_p\left(|x_g - x_p|, h\right)\right) \tag{5.11}$$

where ϕ_I' is the density function on node of grids after the error correction, m_p/ρ_p is the volume characterized by radius r_p of particle, and W_p is a kernel function defined as a spline function. x_g and x_p indicate spatial variables on a grid and a particle, respectively. The referenced radius

h is set to be twice for grid size. The corrected density function ϕ_I' is used in eqs.(6) and (7) and it is also utilized in time integration of the advection equation, eq.(3). In addition, in order to consider ϕ_p defined by Lagrangian particles having characteristics of steelmaking slag, ϕ_3 is also corrected by ϕ_3'. The density function ϕ_I' is employed to track the interface between different phases and it is also utilized to solve Poisson equation for the pressure, eq.(8) considering the density ρ calculated by the density function ϕ_I' in eq. (6). This formulation is applied to multiphase algorithm manner with eq.(8) to solve the pressure in all phases. Moreover, the chemical reaction process can be considered with radius of steelmaking slag and elution from each slag represented by Lagrangian particles. This error correction of density function ϕ_I' is carried out periodically, and not at every time step.

In this study, the particle size of the steelmaking slag is approximately 5-10mm and 30-50mm and the averaged density is 3.0g/cm^3 as shown in Section *Overview Of Field Experiment*. The surface of steelmaking slag is generally rough and the friction stress is relatively large, and then motion of the steelmaking slag is very slow for long time duration in flow velocity due to ground water and tidal current near sea bottom. Therefore, in this study, the suspension and sinking processes are not directly computed as a conventional Lagrangian model is normally used. Considering characteristic of interaction process between slag and flow, turbidity and SS caused by current velocity at sea bottom boundary, the relations between them should be imposed by the experimental and field results for steelmaking slag and sediment as mentioned in subsection Ocean circulation model for global area.

In Eulerian-Lagrangian coupled model, at first, the velocity u_3 of the steelmaking slag on Eulerian grids is computed by using the multi-phase formulations, eqs.(1) to (8) considering several different phases defined on Eulerian grids. In this step, some physical properties of the steelmaking slag can be considered, Next, the velocity u_3 on the grids can be interpolated on Lagrangian particles. Finally, particle locations of steelmaking slag can be tracked by eq.(9) and density function ϕ_I for solid phase on Eulerian grids can be obtained by eq.(3). In Eulerian process, numerical diffusion and smearing could be caused by advection phase in eq.(3). To avoid this error, ϕ_I for solid phase is corrected by eq.(11) including density function ϕ_p defined on Lagrangian grids.

Chemical Reaction Process and Conditions

In ocean space, it should be considered that the risk could be occurred by artificial material installed in sea water. The algal blooming due to Fe irons eluted from steelmaking slag was suggested by some research works. On the other hand, other researcher mentioned that Fe irons can help seagrass and seaweed to growth, especially in oligotrophic ocean space. In practical use, considering some risks, Fe irons should be utilized to improve ocean environment and to contribute to prevention of the blue tide and, in turn, recovery of natural habitats for benthic organisms.

The concentration of dissolved sulfide can be computed by eq.(4) including the flow velocity in eq.(2), considering multiphase flow with different density and viscosity, where S_{ca} is the chemical reaction, which is imposed on Lagrangian particle as boundary condition. The chemical reaction process is occurred on the surface of steelmaking slag in micro scale. According to the previous works [13][14][15][16][17][23], the existence of FeS and S^0 was confirmed by the laboratory experiment in the anoxic condition with Electron probe microanalyzer (EPMA) and X-ray absorption fine structure (XAFS), the reactions, eqs.(12) and (13) as below are occurred. In this case, when oxygen is supplied, the FeS formed by the reaction, eq.(12) can be oxidized to iron oxide and S^0. In the reaction, eq.(13), when the ORP is higher, the formed Fe^{2+} can be re-oxidized to 3+, and the reaction, eq.(13) could be occurred again. This means that the Fe functions substantially as a catalyst in suppressing sulfides, which is in a good agreement with the suggestion by [23].

$$HS^- + Fe^{2+} \rightarrow FeS + H^+ \tag{5.12}$$

$$HS^- + 2Fe^{3+} \rightarrow S^0 + 2Fe^{2+} + H^+ \tag{5.13}$$

When a large amount of dissolved sulfide exists in the interstitial water in the sediments at the test field site, it consumes the dissolved oxygen (DO) at the bottom layer as shown in eq.(14) [15][16].

$$2H_2S + O_2 \rightarrow 2H_2O + 2S \tag{5.14}$$

The above chemical process means that water permeability is firstly improved by the crevices of the slag, and an aerobic environment can be formed in the seawater around the slag. Next, the sulfide concentration in the vicinity of the slag can be reduced by the chemical reaction of sulfides with Fe ions eluted from the slag. Then the pH is increased in the vicinity of the slag, suppressing the activity of sulfate-reducing bacteria living in the sea bottom near the slag, thereby reducing generation of H_2S. The supply of DO is increased by the improved water permeability resulting from placement of the slag, and the amount of H_2S generation decreases, resulting in a decrease in DO consumption accompanying the oxidation reaction of hydrogen sulfide. It is believed that a coastal environment could be considerably improved by effective utilization of steelmaking slag, contributing to prevention of the blue tide and, in turn, recovery of natural habitats for benthic organisms.

Considering the above chemical reaction in eq. (4), the dissolved sulfide can be included in the right hand side term, S_{ca} depending on radius of steelmaking slag and chemical reacted volume as below.

$$S_{ca} = S_t \frac{V_{rct}}{V} \tag{5.15}$$

$$V_{rct} = \frac{4}{3}\pi(r - H)^3 \tag{5.16}$$

where S_t is the total elution of steelmaking slag, V_{rct} is the eluted volume, V is the total volume of steelmaking slag, r is the radius of steelmaking slag and H is the reaction depth from surface of steelmaking slag.

Based on the previous experimental works, elution of steelmaking slag is gradually decreased when the chemical reaction is almost saturated at a certain concentration of the dissolved sulfide around slag. Therefore, the elution potential of slag is defined and it is integrated by a certain concentration. If the concentration of the dissolved sulfide is not saturated at a certain time, the elution process is occurred with the chemical reaction. But the elution is limited when the maximum elution per unit time is reached. The process can be expressed as follows:

$$S_{in}(t) = S_e(t) + S_p, \qquad (0 \leq S_{in} \leq S_{max}) \tag{5.17}$$

where $S_e(t)$ is the elution obtained from the experimental work, S_{max} is the maximum elution of slag per unit time and S_p is the elution potential considering the saturated condition.

The previous works revealed that magnesium, Mg is deposited and it could be covered on the surface of steelmaking slag. Then the elution process is decreased by the covered Mg. This reaction model can be expressed as below:

$$S_{Mg}(t) = S_{in}(t) \cdot D(t) \tag{5.18}$$

$$D(t) = D_{max} \frac{M_{sum}(t)}{M_{max}} \tag{5.19}$$

where S_{Mg} is the elution considering the covered Mg, $D(t)$ is the coverage of Mg on the surface of steelmaking slag, $M_{sum}(t)$ is the total deposition of Mg by a certain time and M_{max} is the deposition for total steelmaking slag. More details can be seen in [24][25]. The initial conditions for the chemical reaction as mentioned above are the saturated elution related to dissolved sulfide, maximum deposition of Mg, radius of steelmaking slag and the reaction depth. They can be identified by experimental work with some chemical conditions.

Computational Domains and Conditions

This study focuses on Fukuyama inner harbor as shown in Figs. 5.1 and 5.2 as mentioned in Section *Overview of Field Experiment*. As shown in Fig. 5.3, the computational domain is 400m for x-axis and 2m for y-axis and the surface of sea bottom is y=0. The initial thickness of the soil phase including slag is constant, 1m, where the silty sediment is linearly 0.2 to 0.4 m for $0 \leq x \leq 400$ based on the field work [15][16]. The averaged water depth is approximately 2.5m during the steelmaking slag construction. The tidal elevation is about 3m in the test field and the resultant tidal current is generated at both side boundaries. The sea bottom and the silty sediment can be represented by Lagrangian particles related to radius of soil and silt as shown in Section *Overview of Field Experiment*. In the previous field work [15][16], the steelmaking slag can reduce dissolved sulfide and Fe ions eluted from slag can react with sulfide. This means that adherent effect due to iron sulfide formed on surface of steelmaking slag was found in the

previous field work. Therefore, it can be assumed that adherent effect due to iron sulfide in upper surface of silty sediment is half with linearity for bottom one in silty sediment. This condition is assumed based on the laboratory experiment in Miyata et al. [15], as shown in Figs. 5.5 and 5.8 of this paper, where the temporal changes of dissolved sulfide were covered by Slag Capping, Slag Mixing, Natural Strone Capping and Control area in the overlying water, the upper layer and the lower layer of the interstitial water. Comparing the dissolved sulfide in the upper interstitial water and the lower interstitial one by the day of detection limit, in Slag Capping, the dissolved sulfide concentrations in the lower interstitial water (Silty sediment area) showed a range of 0.5-0.6mg-S/L, whereas that in the upper interstitial water (Slag area) is about 1.0mg-S/L. Based on this laboratory experiments, it can be assumed that adherent effect due to iron sulfide in upper surface of silty sediment is half with linearity for bottom one in silty sediment. The area of deposited slag is $125 \leq x(m) \leq 275$ and $-0.7 \leq y(m) \leq 0$ while the total thickness of slag is 70cm constructed in 2011 and 2012. The size of the steelmaking slag is 5-10mm for fine particles and 10-25mm for coarse particles and also 30-50 mm as the top cover. Considering the total constructed volume and the total surface of the particles, the radius of Lagrangian particle in this model is set to be half or quarter size of the grid one. The time increment of computation is 600 s. The horizontal grid size is 0.1 m and the vertical one is 0.015 m in the all domain. Fig. 5.4 shows one example of time histories of tidal current velocity based on the averaged observation data near the surface of the silty sediment in x and y axis. The dominant component caused by tidal elevation is mainly horizontal direction in the inner harbor

5.3.2 Ocean Circulation Model for Global Area

Governing Equations and Grid Systems

In global area, ocean circulation model can be employed to compute tidal elevation and current at a bay and an inner harbor, which is one of the well-known ocean circulation model based on Princeton Ocean Model (POM) [20]. The specific coordinate system, σ in vertical axis is constructed along bottom topography and water elevation in order to reduce numerical error

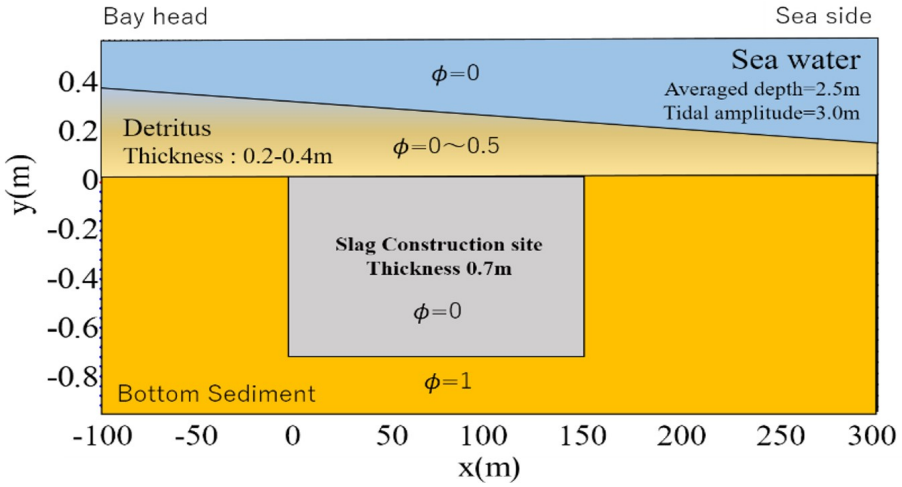

Figure 5.3: Computational domain and condition in Fukuyama inner harbor

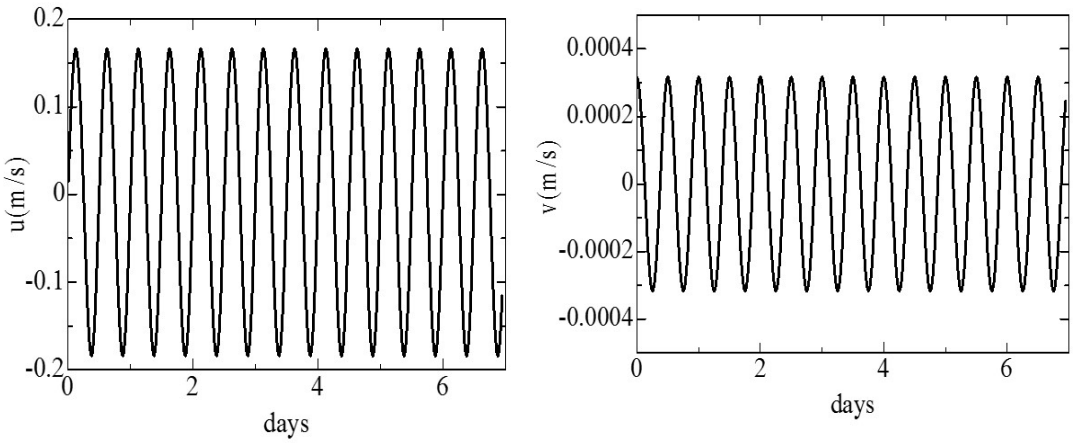

(a) Horizontal velocity

(b) Vertical velocity

Figure 5.4: One example of time histories of tidal current velocity

caused by structural grid generation and complicated bottom topography. The horizontal grid uses Arakawa C-grid and the structured orthogonal coordinates. The basic continuity equation can be written in horizontal Cartesian coordinate after conversion to sigma coordinates, σ , as follows:

$$\sigma = \frac{z - \eta}{H - \eta} \tag{5.20}$$

$$\frac{\partial UD}{\partial x} + \frac{\partial DV}{\partial y} + \frac{\partial \omega}{\partial \sigma} + \frac{\partial \eta}{\partial t} = 0 \tag{5.21}$$

where H is the bottom topography, η is the surface elevation, D is the summation of H and η, t is the time, x, y and z are the conventional Cartesian coordinates, and U, V and ω are the velocity component for x, y and z directions, respectively. The momentum equations can be expressed as follows:

$$\begin{aligned} &\frac{\partial UD}{\partial t} + \frac{\partial U^2 D}{\partial x} + \frac{\partial UDV}{\partial y} + \frac{U\omega}{\partial \sigma} - fVD + gD\frac{\partial \eta}{\partial x} \\ &+ \frac{gD^2}{\rho_0}\int_\sigma^0 \left[\frac{\partial \rho'}{\partial x} - \frac{\sigma'}{D}\frac{\partial D}{\partial x}\frac{\partial \rho'}{\partial \sigma'}\right] \partial\sigma' = \frac{\partial}{\partial \sigma}\left[\frac{K_M}{D}\frac{\partial U}{\partial \sigma}\right] + F_x \end{aligned} \tag{5.22}$$

$$\begin{aligned} &\frac{\partial VD}{\partial t} + \frac{\partial UVD}{\partial x} + \frac{\partial V^2 D}{\partial y} + \frac{V\omega}{\partial \sigma} - fUD + gD\frac{\partial \eta}{\partial y} \\ &+ \frac{gD^2}{\rho_0}\int_\sigma^0 \left[\frac{\partial \rho'}{\partial y} - \frac{\sigma'}{D}\frac{\partial D}{\partial y}\frac{\partial \rho'}{\partial \sigma'}\right] \partial\sigma' = \frac{\partial}{\partial \sigma}\left[\frac{K_M}{D}\frac{\partial V}{\partial \sigma}\right] + F_y \end{aligned} \tag{5.23}$$

where f is the Coriolis parameter, ρ_0 is the sea water density, ρ' is the referenced density, K_M is the vertical kinematic viscosity, F_x and F_y are the diffusivity term for horizontal and vertical axis respectively, t is the time and g is the gravity acceleration. The ocean circulation model can provide vertical mixing coefficients using the second moment turbulence sub-model. The turbulence closure sub-model was introduced by [20] and then it was significantly advanced in collaboration with some researchers. The Mellor-Yamada turbulence closure model is often cited in ocean circulation model. In this study, the Level 2.5 model is used together with a prognostic equation for the turbulence macroscale. More detail can be seen in [26]. The advection-diffusion equations for temperature, salinity and concentration such as DO, H_2S and SS are also employed.

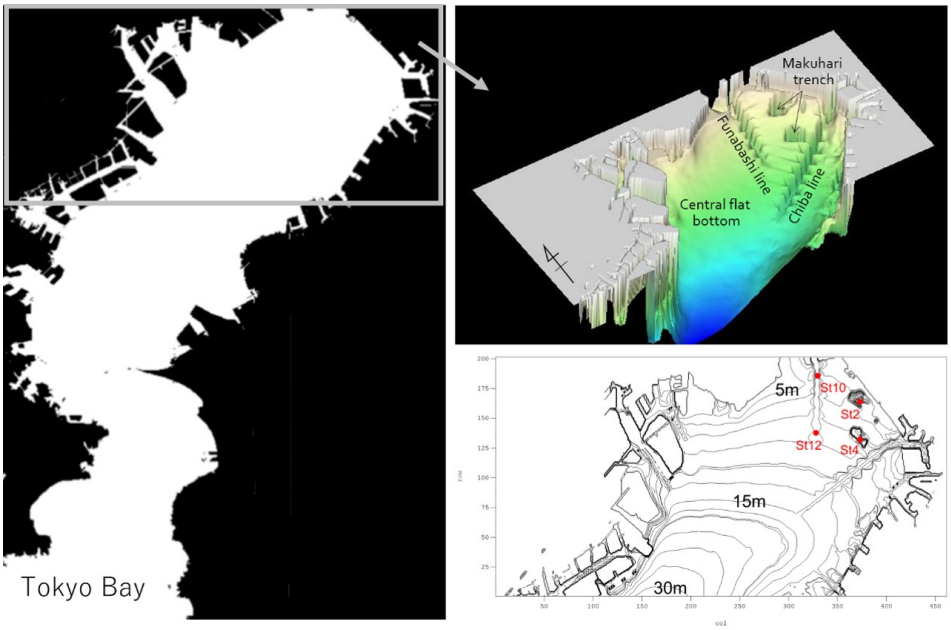

Figure 5.5: Computational domain and bottom topography including trench and navigation channel

Computational Domain and Boundary Conditions

In this study, the focusing site is Tokyo Bay, where the hydrogen sulfide causes the blue tide every year and there is a large number of trenches in which the dissolved oxygen decreases, especially at the bay head in summer season. It was reported that oxygen deficiency was occurred near the sea bottom at the bay head of enclosed area such as Tokyo Bay [1] and Osaka Bay during summer.

The horizontal grid size is 100m for the northern part of Tokyo Bay as the nesting area. The vertical grid is ten layers for sigma coordinate. As shown in Fig. 5.5, the water depth is about 20-30m at the dredged trench of Makuhari and the navigation channel of Funabashi is straight existed from north to south. To evaluate concentration such as H_2S, DO and Suspended solids (SS) in time and space, two kinds of bottom topography are set by covering steelmaking slag at the trenches of Makuhari and navigation channel of Funabashi. The monitoring points colored by red dot are located at these trenches, St.2 and 4 at Makuhari and St.10 and 12 at Funabashi. The boundary condition for the concentration is imposed by the results computed by Eulerian-Lagrangian coupling model. The sulfide reduction effect due to steelmaking slag is imposed at the bottom boundary of these trenches. The condition of the tidal elevation at the mouth of

Table 5.1: Computational conditions

Case	Dredget material	Location	Evaluated items
1	sediment (mud)	Makuhari	H_2S, DO
2	steelmaking slag	Makuhari	H_2S, DO
3	sediment (mud)	Funabashi	H_2S, DO
4	steelmaking slag	Funabashi	H_2S, DO
5	sediment (mud)	Funabashi	SS
6	steelmaking slag	Funabashi	SS

Tokyo Bay is given by the prediction data [27][28].

To impose relation between SS and current velocity at bottom boundary, the experimental results are used as showed in Figs. 5.6 and 5.7. The turbidity is increasing with current velocity. In the steelmaking slag case, the turbidity is considerably low comparing with that in the sediment case and the relationship between SS and the turbidity is linear. Therefore, the regression curve can be represented by the experiment data to clarify the relationship between the current velocity and SS. By using this regression curve, concentration of SS can be imposed at seabed boundary condition under certain current velocity at bottom layer which is computed by ocean circulation model. Fig. 5.8 shows time variation of dissolved sulfide in both sediment (mud) cover case and steelmaking slag one. The dissolved sulfide in the slag case is rapidly decreasing with time and also the minimum value is almost zero after one week in this experiment. Fig. 5.9 shows relationship between H_2S and DO observed by [29]. The data was obtained at three different locations in Tokyo Bay. The field data are widely distributed with field fluctuation at these locations. However, the regression curves can be used at seabed boundary and the initial condition in this study.

The model uses a time split for time step in the external domain, in which two-dimensional part of dynamics (sea surface elevation and depth-averaged currents) is computed separately with a short time step. For vertical distribution of currents in the internal domain time step, salinity and temperature can be computed in 3D with a much longer time step. The coupling process with Euler-Lagrangian model at seabed covered by steelmaking slag is employed in the time step for the internal domain in 3D. The time steps for the external and internal domain are selected to be twelve second and sixty second, respectively. By using the ocean circulation

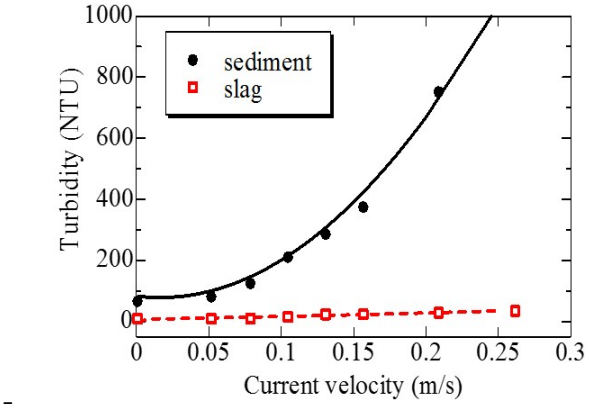

Figure 5.6: Comparison of turbidity to current velocity between sediment and sediment-slag

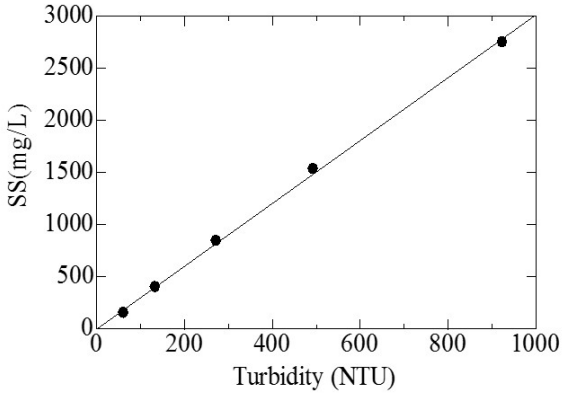

Figure 5.7: Relationship between turbidity and Suspended Solids (SS)

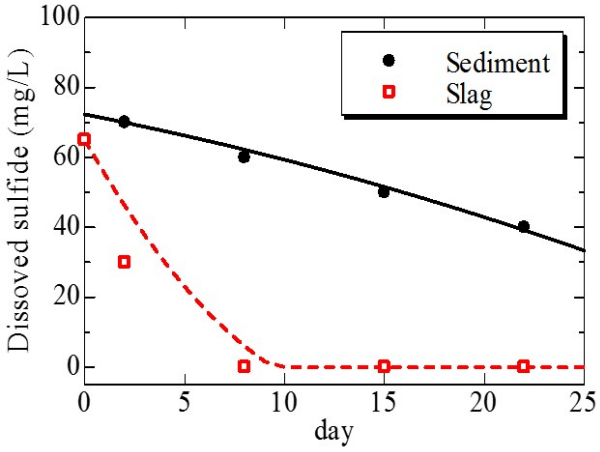

Figure 5.8: Comparison of dissolved sulfide between slag and sediment (mud)

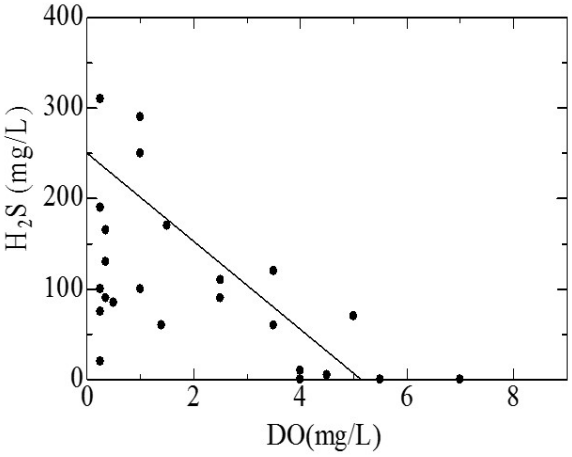

Figure 5.9: Relationship between H_2S and DO [29]

model, water elevation, tidal-current velocity magnitude and vector can be estimated for two-weeks prediction and two days spin-up simulation. The computational conditions are shown in Table 5.1. The dredged materials are set to be both sediment (mud) and steelmaking slag in order to compare sulfide reduction effect due to steelmaking slag. The dredged locations are Makuhari trench and Funabashi navigation channel where the concentrations of H_2S, DO and SS are evaluated.

In this model, a nesting technique is employed at sea bottom boundary to consider dissolved sulfide, turbidity, SS and sea bottom topography exchange. The sea bottom topography on ocean circulation model is exchanged by the surface distribution of steelmaking slag computed by eq.(3). The current velocity at the sea bottom computed by the ocean circulation model

is used to impose the turbidity and SS using the regression curve in Figs. 5.6 and 5.7 as boundary condition. The chemical reaction S_{ca} in eq.(4) based on the explanation in chemical reaction process and conditions section is considered with the elution results in Fig. 5.8. The dissolved oxygen is also imposed by the relationship based on the observed data in Tokyo Bay as shown in Fig. 5.9. The suspended matter for steelmaking slag and sediment caused by current velocity at sea bottom boundary are modeled by using the turbidity and SS obtained in the experiment and therefore the relations are imposed by the result as shown in Figs. 5.6 and 5.7. To work well without numerical instability, the horizontal grid size, Δx_c for Eulerian-Lagrangian model should be fine comparing with one, Δx_o for ocean circulation model, which is set to be $\Delta x_c = \Delta x_o/M$, where M is about $50 \sim 100$ in this study. Then the time increment Δt_c for Eulerian-Lagrangian model is set to be Δt_c=Δt_o/N, where Δt_o is the time increment for ocean circulation model and N is set to be about $10 \sim 50$. More details can be seen in [24][25][30][31].

5.4 Validation with Field Experimental Data

In Fukuyama inner harbor, the initial conditions for temperature of sea water, DO and pH are based on the field observation in [16]. This chemical process was confirmed by some research works as the referenced papers. The validations with field observation at Fukuyama inner harbor are shown in Figs. 5.10 and 5.11.

Fig. 5.10 shows comparison of tidal elevation during one week, at the nearest location, Onoshima, provided by Japan Meteorological Agency and the result is overall agreement with JMA data. Fig. 5.11 also shows comparison of dissolved sulfide at three different vertical positions after two weeks from the 2^{nd} construction in the field site. The horizontal axis indicates distance from origin at the center of Site A (x=0) from head of harbor to sea side in Fukuyama inner harbor. The interstitial water was measured at both 5-10cm depth from surface of silty sediment and floating mud. The overlying water in floating mud with detritus was obtained at 5-10cm above the surface of the floating mud. This results indicate that the steelmaking slag

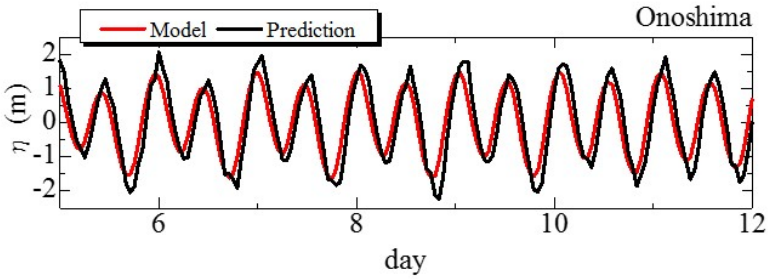

Figure 5.10: Comparison of tidal elevation at the nearest location, Onoshima, provided by JMA

has potential for recovering organically enriched sediment including H_2S and also it is one of the useful remediation techniques for improving ocean environment on sea bottom sediment. The computational results by Eulerian-Lagrangian model are overall agreement with the field experimental data in Fukuyama inner harbor. The concentrations of the resolved sulfide in the interstitial water at the construction sites A, B and C are drastically decreased comparing with those at the referenced site, that is, the head of harbor and the sea side. On the other hand, the concentration of the resolved sulfide in the overlying water is quite low and it is almost stable condition at both the construction and the referenced sites. This tendency is the same with the computational results and the model is a useful assessment tool for evaluating and predicting concentration of dissolved sulfide due to tidal current. However more detailed validations in velocity and concentration during long time, should be quantitatively conducted in future effort.

5.5 Reduction Effect of Dissolved Sulfide using Steelmaking Slag

Fig. 5.12 shows comparison of horizontal distribution of dissolved sulfide at three different construction conditions, that is, present case, no-construction one with no steelmaking slag and expanded one. The expanded area is set to be twice for the present area at -75$\leq x(m) \leq$225 where the steelmaking slag is covered. It can be seen that the reduction effect of the dissolved sulfide is remarkably emerged in the expanded area and also the horizontal distribution of the

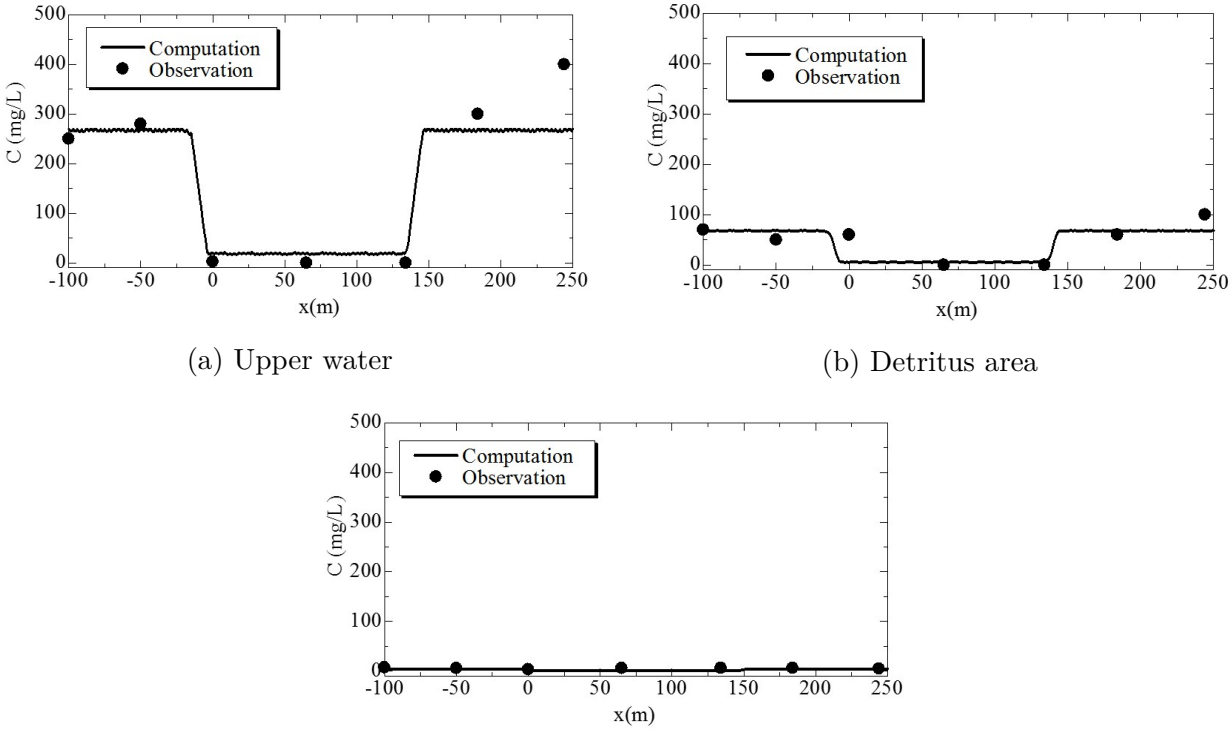

(a) Upper water

(b) Detritus area

(c) Interstitial water at sediment layer

Figure 5.11: Comparison of dissolved sulfide at three different vertical positions with filed experimental data in Fukuyama inner harbor

dissolved sulfide is the same tendency with the present case. This means that the steelmaking slag in silty sediment can reduce concentration of dissolved sulfide in interstitial water at not only silty sediment but also floating mud over whole area covered by steelmaking slag.

Fig. 5.13 shows comparison of vertical distribution of dissolved sulfide for three different construction conditions. The horizontal axis indicates concentration of dissolved sulfide and origin of vertical axis (y=0) indicates surface of silty sediment. The conditions for the construction area of steelmaking slag and floating mud are mentioned in Eulerian-lagrangian model for local area. In the construction site, the concentration of dissolved sulfide in silty sediment area, $y_{(m)} \leq 0$, is almost zero and it could be perfectly controlled by the steelmaking slag. In the floating mud region at $0 \leq y_{(m)} \leq 0.2 \sim 0.4$ as shown in Fig. 5.3, the concentration of dissolved sulfide is gradually decreasing and it is almost zero at the surface of silty sediment, y=0. This is because iron sulfide, FeS, formed on the surface of steelmaking slag can suppress sulfide in the silty sediment [15][16]. On the other hand, the concentration of dissolved sulfide is increased near the top of the floating mud because the steelmaking slag diminishes in effectiveness. The

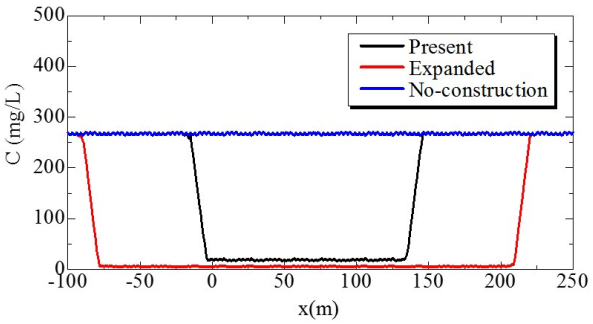

(a) Upper water

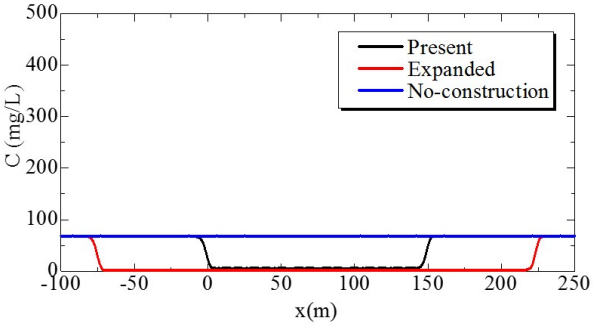

(b) Detritus area

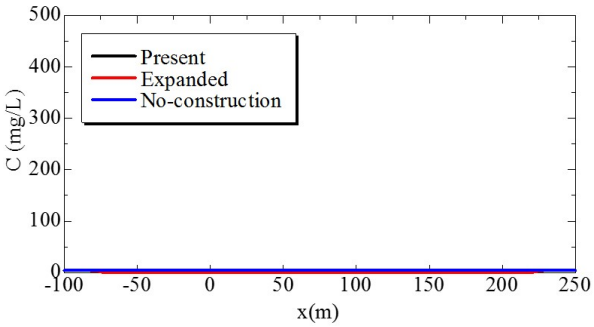

(c) Interstitial water at sediment layer

Figure 5.12: Comparison of spatial distribution of dissolved sulfide for three different vertical constructions

concentration of the dissolved sulfide is drastically decreasing from the surface of the floating mud to the overlying water. The tendency was also found in [15][16]. However, more detail validations should be required in future work although it is difficult to take a sample by divers without any disturbance in floating mud where porosity is higher in sea water.

5.6 Application to Tokyo Bay

Before constructing steelmaking slag at seabed in real sea condition, environmental impact assessment should be demonstrated in semi-enclosed sea as a numerical survey. The numerical model based on ocean circulation model [30] coupling with Eulerian-Lagrangian model [19] is applied to Tokyo Bay including the dredged trench and the navigation channel one at the sea bottom as shown in Fig. 5.5, during short time period, only two weeks. The initial conditions are based on [29] and the experimental results as shown in Figs. 5.6, 5.7 and 5.8 considering the chemical process mentioned in Chemical reaction process and conditions section. The

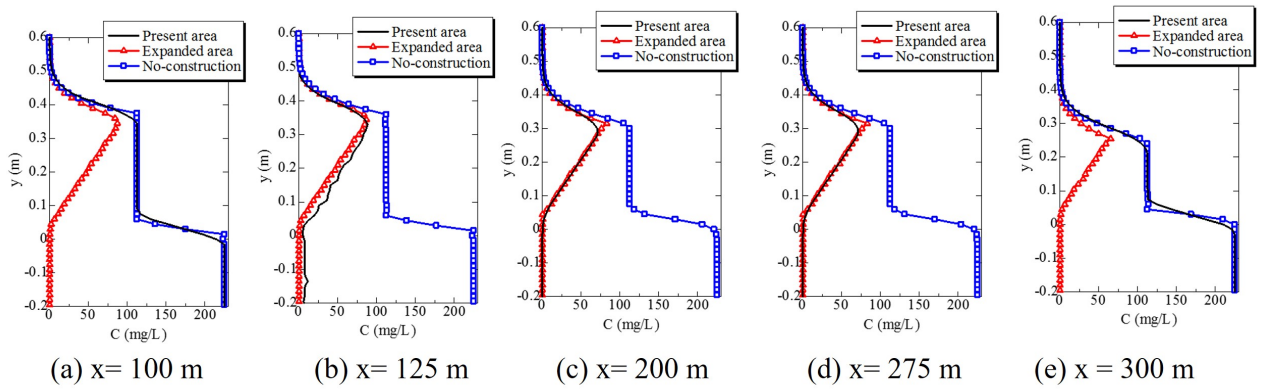

Figure 5.13: Comparison of vertical distribution of dissolved sulfide for three different construction conditions

distributions of salinity and temperature in August 2015 are set by the observed data provided by Japan Coast Guard [32]. However, there is no research works on relationships among dissolved sulfide, temperature of sea water, salinity and the reaction speed. In this model, it is assumed that the chemical reaction is not affected by salinity and temperature of sea water even if in stratification condition. The chemical reaction with temperature and salinity should be investigated by laboratory experiments and their results must be considered in future effort.

Fig. 5.14 shows comparison of time histories of water elevation between numerical results, prediction and observed ones during August 1^{st} to 15^{th} in 2015. The prediction data is given by astronomical tide of Japan Meteorological Agency, JMA [27]. The mathematical method [28] is based on the harmonic analysis of tide assuming that the rise and fall of the tide in any locality can be expressed theoretically by the sum of a series of harmonic terms having certain relations to astronomical conditions, what we call astronomical tidal level. And also the referenced data [27] is given by Japan Meteorological Agency. The provided data is mathematically predicted by astronomical tidal level and also the observed data at 71 locations is validated and opened on the web site. The comparison of tidal elevation at Kawasaki is also added with the nearest observed location at Harumi given by Japan Meteorological Agency, as shown in Fig. 5.14(e). The model results in the tidal amplitude are overall agreement with the predictions and observations ones. However, it is a little overestimated and the tidal phase is also slightly shifted. There is also a small fluctuation and little discrepancy of the tidal phase at low tide period and tide amplitude. The difference between them is generated by the implementation of

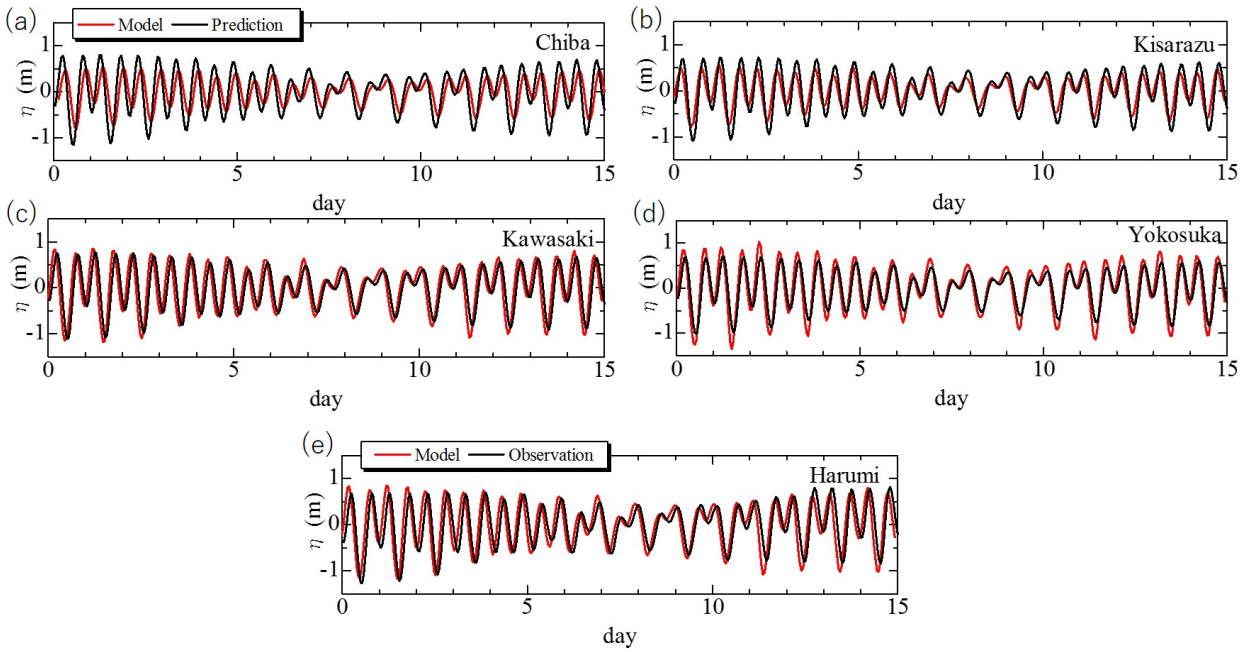

Figure 5.14: Comparison of time history of water elevation between model results, prediction and observed ones by JMA

leapfrog advection scheme in the ocean circulation model, and therefore it should be improved in future effort. However, the results are reasonably good for investigating concentration of DO, H_2S, SS, and characteristic of tidal assessment in Tokyo Bay in the following section.

Fig. 5.15 shows comparison of current velocity near sea bottom with the observed data at Tokyo light beacon near Haneda, the northern part of Tokyo Bay, which is provided by the Bureau of Port and Harbor, Tokyo Metropolitan Government [33]. The model results cannot reproduce spiky fluctuation with high frequency and some of the amplitude in the model cannot be represented with the observed ones. This is because the weather condition caused by wind was ignored and the discharges from Sumida and Arakawa rivers were assumed by the monthly averaged data. However, the model could be available for examining some scenarios as a preliminary study for ocean environmental assessment to install steelmaking slag. Fig. 5.16 shows one example of velocity field in flood tide and ebb one at whole area in Tokyo Bay. Figs. 5.17-5.21 shows time and spatial variation of DO, H_2S, and SS after three days, one week and two weeks in order to investigate them in the present situation. It is assumed that the high concentration of H_2S and the oxygen-deficient condition are occurred, where the blue tide sometimes occurs and sulfate-reducing bacteria is quite active at the dredged trench in the

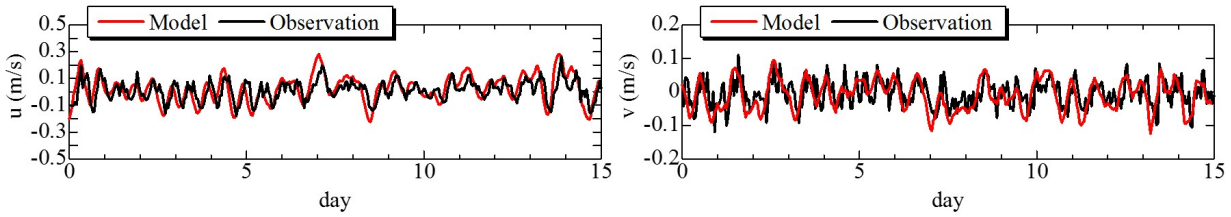

(a) East-West current (b) North-South current

Figure 5.15: Comparison of time history of current velocity near sea bottom with the observed data at Tokyo light beacon

(a) Flood tide (b) Ebb tide

Figure 5.16: One example of velocity field in flood tide and ebb tide at whole area of Tokyo Bay

present situation.

After one week, the concentrations of DO, H_2S and SS at the trench are spreading by advection-diffusion due to tidal current. The low concentration region of DO, less than 2mg/L, is diffused from the trench and it is extended with advection-diffusion in the direction from north-west to south-east. The high concentration region of H_2S, over 70mg/L, can also be found at the same distribution tendency with the concentration of DO. These results mean that the concentration of DO causes oxygen deficient for marine biology and fish and also the high concentration of H_2S makes stink so that the blue tide could occur especially in summer. On the other hand, in the steelmaking slag case, the low concentration area of DO is not generated and also the high

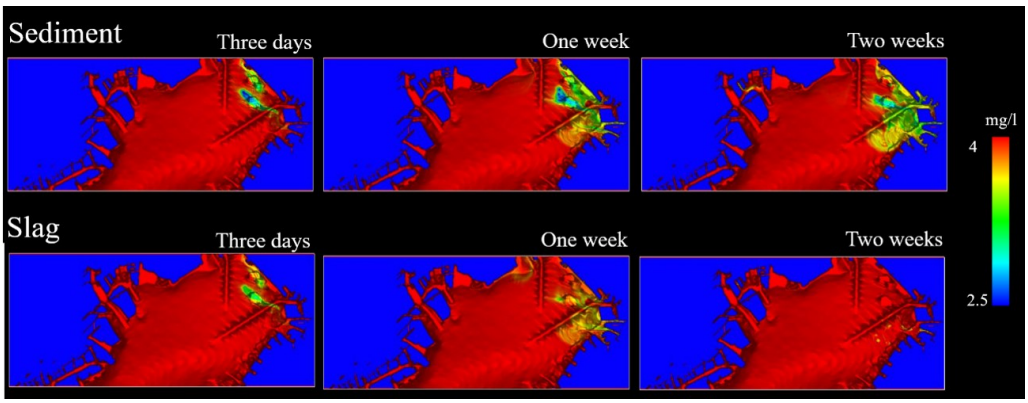

Figure 5.17: Spatial variation of dissolved oxygen, DO in Makuhari trench

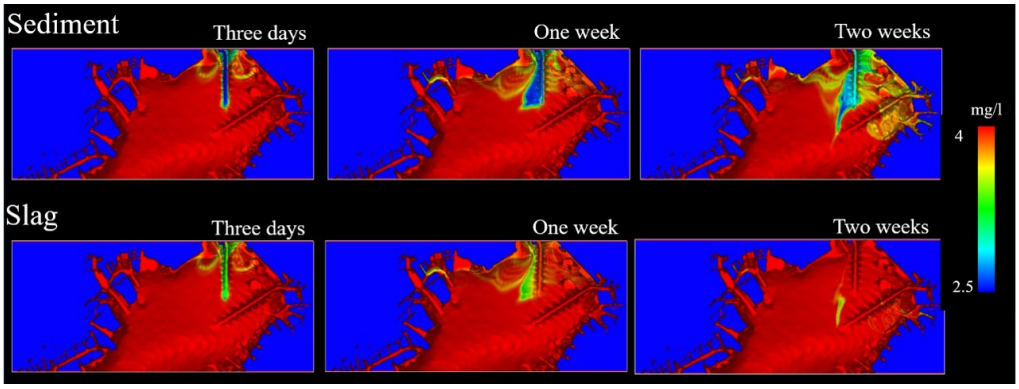

Figure 5.18: Spatial variation of dissolved oxygen, DO in Funabashi line

concentration area of H_2S cannot be found around the dredged trench when the steelmaking slag is constructed at the trench. This result indicates that the steelmaking slag could cover on the organically enriched bottom sediment at the dredged trench to control hydrogen sulfide and oxygen deficient water.

The monitoring points are located at Makuhari trench and Funabashi line as shown in Fig. 5.5 to investigate time variation of H_2S, DO and SS at the assessment area in Tokyo Bay. Figs. 5.22 and 5.23 show time histories of DO concentration and H_2S at Makuhari trench (St.2 and St.4) and Funabashi line (St.10 and St.12). The concentration of DO in slag case is in stable state in high level of concentration after two weeks. On the other hand, in sediment case, it is lower than that in slag case at all monitoring points, St.2 and St.4, which is sometimes less than 3.0mg/L, that is oxygen-deficient water. The concentration of H_2S in slag case is rapidly decreasing and it gradually reaches zero after one week. Whereas in sediment case, it is not stable and not drastically decreasing by two weeks. This is because the dissolved sulfide in slag case is rapidly

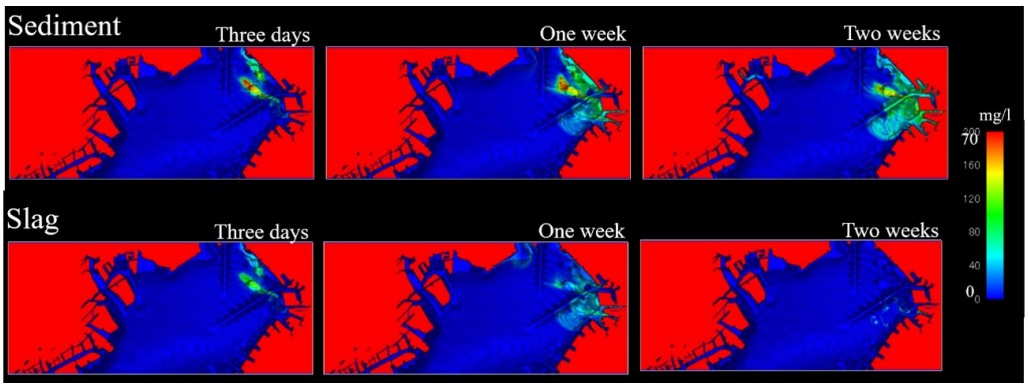

Figure 5.19: Spatial variation of hydrogen sulfide (H_2S) in Makuhari trench

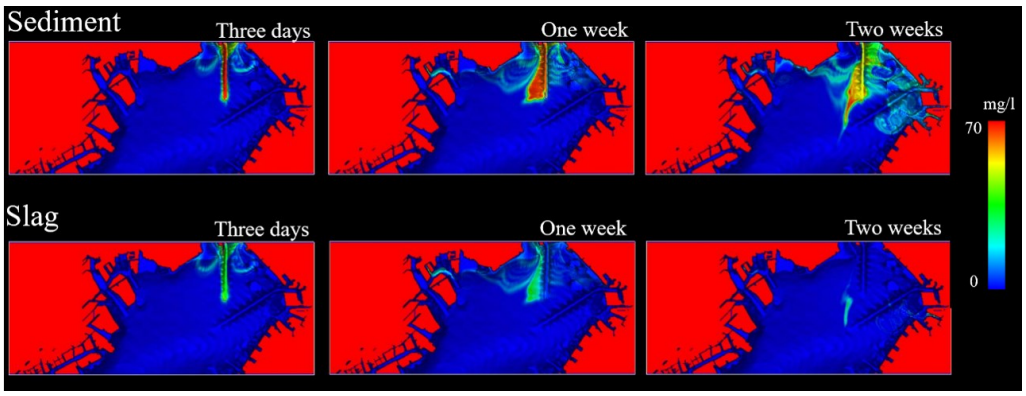

Figure 5.20: Spatial variation of hydrogen sulfide (H_2S) in Funabashi line

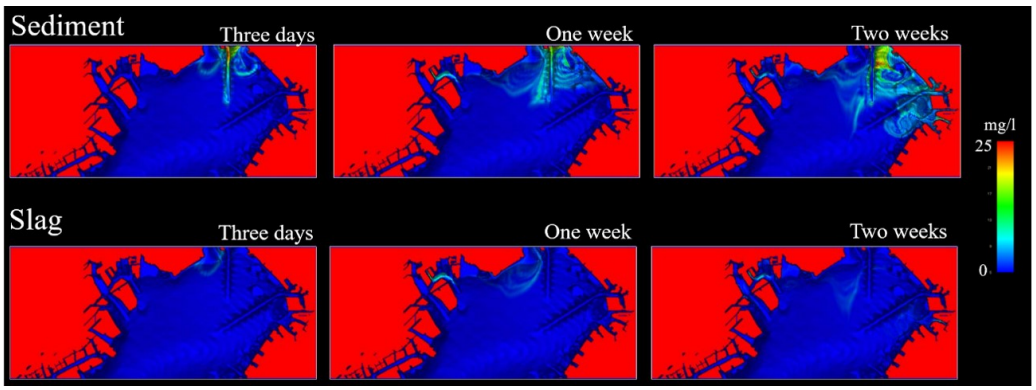

Figure 5.21: Spatial variation of suspended solid (SS) in Funabashi line

decreasing during one week, but in sediment case, it is gradually decreasing. In slag case, the concentrations of DO and H_2S are stable state for remediation of ocean environment, which is relatively high concentration of DO, about 6 mg/L and the low concentration of H_2S, about less than 30 mg/L. Fig. 5.24 shows time history of SS at Funabashi navigation line (St.10 and St.12). In slag case, SS is almost zero during two weeks but it is relatively high concentration in sediment case. As shown in Figs. 5.6 and 5.7, SS is imposed with current velocity at seabed boundary. Considering this experimental data, the slag could cover suspended matter

escaping from trench area. These results indicate that steelmaking slag is one of the useful and effective material for improving sea bottom sediment including hydrogen sulfide, especially at deep trench, where organic material and sulfate-reducing bacteria in anaerobic condition are accumulated.

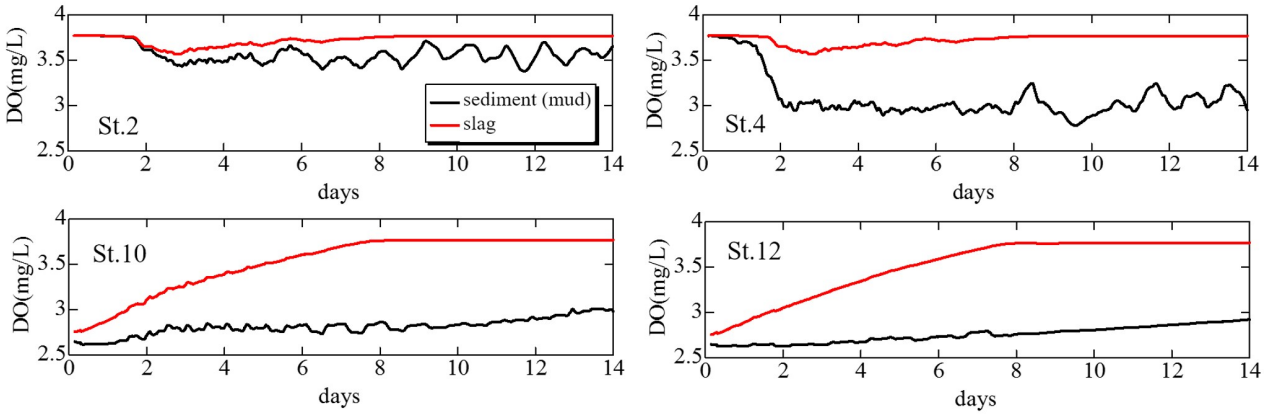

Figure 5.22: Time histories of DO at Makuhari trench (St.2 and St.4) and Funabashi line (St.10 and St.12)

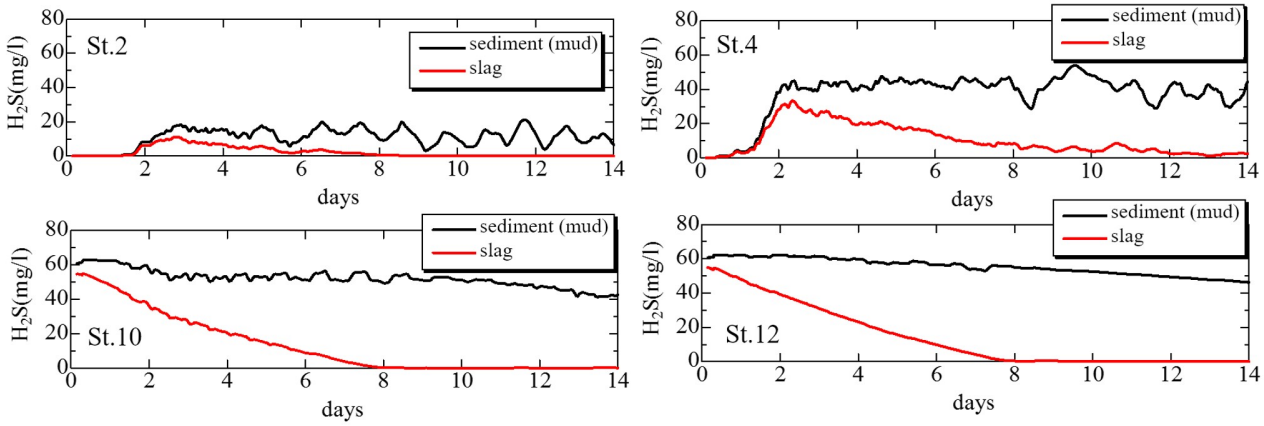

Figure 5.23: Time histories of H_2S at Makuhari trench (St.2 and St.4) and Funabashi line (St.10 and St.12)

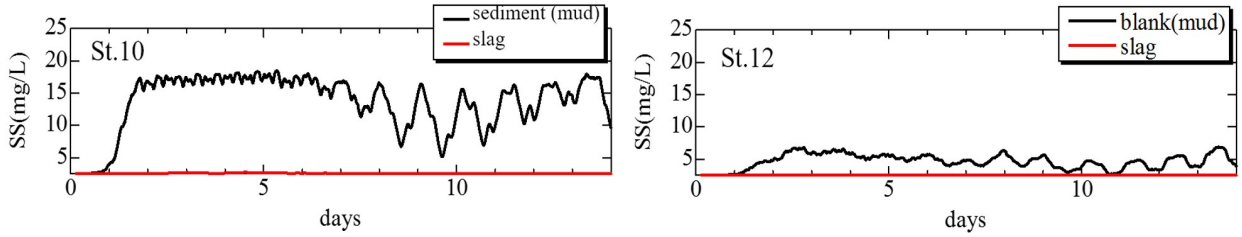

Figure 5.24: Time histories of SS at Funabashi line (St.10 and St.12)

5.7 Conclusions

In this study, the numerical model has been proposed and developed using Eulerian-Lagrangian model with ocean circulation model in order to consider fluid-particle interaction between tidal current and steelmaking slag, and advection-diffusion of dissolved sulfide. The model was also applied to Fukuyama inner harbor and Tokyo Bay using the experimental and field data. The numerical results are overall agreement with the experimental ones. The results showed that the model is a useful assessment tool for evaluating and predicting concentration of dissolved sulfide due to tidal current. Furthermore, the numerical results demonstrated that steelmaking slag can control advection-diffusion of concentration of DO and H_2S which is highly toxic and fatal to benthic organisms and it causes oxygen-deficient water and the blue tide at the dredged trench in Tokyo Bay. Accordingly, steelmaking slag could improve organically enriched sea bottom in enclosed sea area. In future effort, more detailed validation should be quantitatively conducted and also a more sophisticated model should be developed in physical-chemical interaction process between slag and sea water.

Bibliography

[1] Jun Sasaki, M. Isobe, A. Watanabe, and M. Gomyo. Field measurement and a mathematical model of seasonal variation of temperature and dissolved oxygen in Tokyo Bay. In *Proc. of Coastal Engineering Vol.40, JSCE*, pages 1051–1055. Japan Society of Civil Engineers, 1993.

[2] Maki Hideaki. Deterioration of sedimentary environment and assessment of its impact on benthic fauna in coastal sea close to urbanized area. Technical report, National Institute Environmental Studies, 2013.

[3] Shiho Ichioka, Jun Sasaki, Yuya Yoshimoto, Kenichiro Shimosako, and Shunsuke Kimura. Analysis of sulfide dynamics including outbreak of blue tide in navigation channels and

dredged trench of tokyo bay. *Journal of Japan Society of Civil Engineers, Ser. B2 (Coastal Engineering)*, 65(1):1041–1045, 2009.

[4] Ministry of Land, Infrastructure, Transport and Tourism, Japan. Report of the Transport Policy Council on the Basic Plan of a Future Port Environment Policy. Technical report, Tokyo, 2005.

[5] Ministry of the Land, Infrastructure, Transport and Tourism: Japan Coast Gurard. White Paper on Land, Infrastructure, Transport and Tourism in Japan, 2013, 2013.

[6] Ministry of Environment. Slag report, 2014.

[7] S Ozeki. Properties and usage of steel plant slag. enco-steel: steel for sustainable development. pages 23–25, 2004.

[8] JFE Steel Corporation. Environmental report for jfe holdings inc. and jfe steel corporation. Technical report, JFE Steel Corporation, Tokyo, 2004.

[9] Nippon Slag Association. Environment-friendly Material, Iron and Steelmaking Slag. Technical report, Tokyo, 2010.

[10] Kyunghoi Kim, Satoshi Asaoka, Tamiji Yamamoto, Shinjiro Hayakawa, Kazuhiko Takeda, Misaki Katayama, and Takasumi Onoue. Mechanisms of hydrogen sulfide removal with steel making slag. *Environmental Science & Technology*, 46(18):10169–10174, 2012.

[11] Taichi Nagai, Osamu Miki, and Chikako Okumura. Effects of chelated iron on the growth of sargassaceae species at the germling and immature stages. *Journal of Water and Environment Technology*, 12(3):285–294, 2014.

[12] Hitomi Yano, Tetsuji Okuda, Satoshi Nakai, Wataru Nishijima, Terumi Tanimoto, Satoshi Asaoka, Shinjiro Hayakawa, and Satoru Nakashima. Mechanisms of solidification and subsequent embrittlement of dephosphorization slag used in a subtidal zone as an alternative to sea sand and prevention of solidification by adding dredged soil. *Clean Technologies and Environmental Policy*, 18(4):1167–1176, 2016.

[13] Akio Hayashi, Satoshi Asaoka, Tetsuya Watanabe, Ryoko Kaneko, Katunori Takahashi, Yasuhito Miyata, Kyunghoi Kim, Tamiji Yamamoto, Ryo Inoue, and Tatsuro Ariyama. Mechanism of suppression of sulfide ion in seawater using steelmaking slag. *ISIJ International*, 54(7):1741–1748, 2014.

[14] Akio Hayashi, Hirokazu Tozawa, Katsuya Shimada, Katunori Takahashi, Ryoko Kaneko, Fumitaka Tsukihashi, Ryo Inoue, and Tatsuro Ariyama. Effects of the seaweed bed construction using the mixture of steelmaking slag and dredged soil on the growth of seaweeds. *ISIJ International*, 51(11):1919–1928, 2011.

[15] Yasuhito Miyata, Akio Hayashi, Michihiro Kuwayama, Tamiji Yamamoto, and Norito Urabe. Reduction test of hydrogen sulfide in silty sediment of fukuyama inner harbor using steelmaking slag. *ISIJ International*, 55(12):2686–2693, 2015.

[16] Yasuhito Miyata, Akio Hayashi, Michihiro Kuwayama, Tamiji Yamamoto, Kazuho Tanishiki, and Norito Urabe. A field experiment of sulfide reduction in silty sediment using steel-making slag. *ISIJ International*, 56(11):2100–2106, 2016.

[17] Akio Hayashi, Tetsuya Watanabe, Ryoko Kaneko, Akira Takano, Katunori Takahashi, Yasuhito Miyata, Shouko Matsuo, Tamiji Yamamoto, Ryo Inoue, and Tatsuro Ariyama. Decrease of sulfide in enclosed coastal sea by using steelmaking slag. *ISIJ International*, 53(10):1894–1901, 2013.

[18] Huang Yi, Guoping Xu, Huigao Cheng, Junshi Wang, Yinfeng Wan, and Hui Chen. An overview of utilization of steel slag. *Procedia Environmental Sciences*, 16:791–801, 2012.

[19] Suandar Baso, Hidemi Mutsuda, Takehiro Kurihara, Takayuki Kurokawa, Yasuaki Doi, and Jiangang Shi. An eulerian scheme with lagrangian particles for evaluation of seakeeping performance of ship in nonlinear wave. *International Journal of Offshore and Polar Engineering*, 21(2):103–110, 2011.

[20] Alan F. Blumberg and George L. Mellor. A Description of a Three-Dimensional Coastal Ocean Circulation Model. In *Three-Dimensional Coastal Ocean Models*, volume 4, pages 1–16. 1987.

[21] Takashi Yabe, Feng Xiao, and Takayuki Utsumi. The Constrained Interpolation Profile Method for Multiphase Analysis. *Journal of Computational Physics*, 169(2):556 – 593, 2001.

[22] R. A. Gingold and J. J. Monaghan. Smoothed particle hydrodynamics - Theory and application to non-spherical stars. *Mon. Not. R. Astron. Soc.*, 181:375–389, November 1977.

[23] S Asaoka, T Yamamoto, H Yamamoto, H Okamura, K Hino, K Nakamoto, and T Saito. Estimation of hydrogen sulfide removal efficiency with granulated coal ash applied to eutrophic marine sediment using a simplified simulation model. *Marine Pollution Bulletin*, 94(15):55–61, 2015.

[24] H Mutsuda, M Kamada, T Okuda, and Y Doi. co_2 sequenstration capacity using chemical extraction from steel slags in ocean space. *Journal of Japan Society of Civil Engineers, Ser. B2 (Coastal Engineering)*, 69(2):1276–1280, 2013.

[25] T Okuda, K Yoshitugu, H Yano, Y Akiyama, S Nakai, W Nishijima, S Asaoka, M Okada, and T Katayama. Solidification behavior of steel slag in seawater. *Proceedings of the 23rd Annual Conference of Japan Society of Material Cycles and Waste Management*, 2013.

[26] Princeton Ocean Model. Users Guide for a Three-Dimensional, Primitive Equation, Numerical Ocean Model : POM, 2002.

[27] Japan Meteorological Agency. Tide Chart, 2015.

[28] Paul Schureman, U.S. Coast, and Geodetic Survey. *Manual of harmonic analysis and prediction of tides*, volume 98. Washington, D.C.: U.S. Coast and Geodetic Survey, 1971.

[29] G. Kanaya, Koshikawa, Y. Nakamura, H. Higashi, and Maki Hideaki. Deterioration of sedimentary environment and assessment of its impact on benthic fauna in coastal sea close to urbanized area. Technical report, NIES Research Project Report, No.106, 2013.

[30] Shade Rahmawati, Hidemi Mutsuda, and Yasuaki Doi. Numerical Estimation for Tidal-Current Energy Resources in Indonesia. In *Proceedings of the Twenty-sixth International Ocean and Polar Engineering Conference*, volume 1, pages 519–527, 2016.

[31] T Takahashi, H Mutsuda, H Arai, and Y Doi. Numerical simulation of tidal current and topography change caused by wave and tide. *Proceedings of Hydraulic Engineering*, 50:1459–1464, 2006.

[32] Japan Coast Guard. Tide data, 2015.

[33] Bureau of Port and Harbor, Tokyo Metropolitan Government. Current data, 2015.

Chapter 6

Preliminary Assessment of Ocean Pollution Effect in Sunda Strait Indonesia on Fishery and Aquaculture

6.1 Overview of Sunda Strait Environment Conditions

Sunda Strait is bordered by two islnads, Sumatera Island in the north and west and Java Island in the south and east, and administratively within two provinces that are Banten Province and Lampung Province. At its narrowest part in the north-east sill, it is only about 24 km wide [1]. It is a very deep, more than 90 m, in several locations but also very shallow, about 20m or less especially near small Sangiang Island in the middle part of Sunda Strait as shown in Fig.6.1. Sunda Strait has a shallow bay with a shoreline about 37 km and provides economic services ranging from port and shipping industries, tourism to fishery sectors. Fishery has been a major income for local communities for long time. The coastal bay of Sunda Strait is home for almost 23,000 fisherman work on fishing and marine-culture [2] [3]. Fisherman use almost all types of fishing equipment, such as . Based on national data from Ministry of Marine Affairs and Fisheries Indonesia, there are about 6,000 units of fishing equipment within Sunda Strait area [4]. While fishery activity provide an income for local communities, the concern over the

Figure 6.1: Main study site location of Sunda Strait in Indonesia. Study site is marked with yellow square.

land-based pollution is also growing as the coastal area becomes a major site of illegal waste disposal.

Previous reports have showed the presents of high concentration of heavy metal solution in Sunda Strait area, especially along the west coast of Java Island [5][6] and southern part of Sumatera Island[7]. Population growth is affecting the land-based population amount, especially Pb (lead), as reported by Hosono [8]. Booij [9] reported that Banten Bay, located on northern part of Sunda strait, has a similar values of Pb found in Jakarta Bay which has increasing coastal pollution tendency[10]. However, Suwandana in 2007 [11] reported that heavy metal contamination was lower than Jakarta Bay. Despite the lower pollution amount, Pb concentrations, both in water and sediment, are still significantly high in the mixing layer, about 20 mg/L [8], and they may lead to a decrease in productivity of fishery and marine aquaculture. Based on previous researches [12][13], Pb can contaminate and infiltrate the ocean biota. Although the contamination process occur slowly, Pb can quickly inhibit respiration and photosinthesys process on phytoplankton algae [14]. Phytoplankton algae is an autotrophic microorganism which has the ability to produce organic matter from inorganic material through photosynthesys process with the help of light. Approximately 95% of primary productions in the ocean come from phytoplankton [15]. Therefore, it is very important to understand the environment condition that affecting the phytoplankton production ability.

Generally, phytoplankton algae in the sea is composed by diatom species (*Bacillariophyceae*),

followed by dinoflagellates (*Dinophyceae*) and blue green algae (*Cyanophyceae*) [14-in pratiwi]. In Indonesia, specifically around Java Island, phytoplankton species are dominated by *Bacillariophyceae* where it compose 73-85% phytoplankton in offshore and 71-78% for nearshore location [16]. By estimating the Pb (lead) concentration distribution due to tidal current flow, the influence on phytoplankton algae photosynthesis can also be known and understood. Spatial and temporal variation in pollutant accumulation were most probably affected by distance from source and physical conditions of the environment such as current and mixing[6] which not accomplished yet in previous researches. Ke [17] also suggests that spatial distribution of phytoplankton is significantly influenced by the surface current pattern. Therefore, until this environment problem is solved, it is important to understand the relationship between land-based pollution and ocean circulation in order to avoid fishery loss by considering the monsoon season in Indonesia.

6.2 Method

This research utilized Princeton Ocean Model (POM) [18] to compute tidal elevation and current flow which affecting pollutant diffusion. The principal attributes of the model are including: second moment turbulence closure sub-model to provide vertical mixing coefficients, sigma coordinate model scaled on the water column depth as the vertical coordinate, unstructured horizontal grid, free surface, and split time steps [19]. The specific program that is now applied to the research simulates tidal-driven flow across the strait with a prescribed vertical temperature stratification, constant salinity, zero surface heat and salinity flux, an a zero wind stress distribution although wind stress may also be applied. By applying point-source pollution, the model simulates the pollutant which distributed due to tidal current flow. The horizontal viscosity and diffusion terms are defined as below:

$$F_x = \frac{\delta}{\delta x}(H\tau_{xx}) + \frac{\delta}{\delta y}(H\tau_{xy}) \tag{6.1}$$

$$F_x = \frac{\delta}{\delta x}(H\tau_{xy}) + \frac{\delta}{\delta y}(H\tau_{yy}) \tag{6.2}$$

where x, y is cartesian coordinate, H is the bottom topography, and $\tau_{xx}, \tau xy, \tau yx, \tau yy$ as below.

$$\tau_{xx} = 2A_M \frac{\delta U}{\delta x}, \tau_{xy} = \tau_{yx} = A_M \left(\frac{\delta U}{\delta y} + \frac{\delta V}{\delta x} \right), \tau_{yy} = 2A_M \frac{\delta V}{\delta y} \tag{6.3}$$

where U, V is tidal current velocity in x, y direction respectively, and A_M represents Smagorinsky diffusivity for horizontal diffusion. A_M decreases as resolution improves.

The computational area of Sunda Strait simulation is shown in Fig.6.2 where there are 12 monitoring points to acquire numerical results. The area is 36km in x and 18.7km in y direction which divided into 61 x 61m grid size. The minimum depth is 5m while maximum depth is 120m, and this depth range is divided into four sigma layer. As the tide data are taken from Tide Model Driven (TMD) which is used to achieve tide prediction data by ESR/OSU [20]. Because Indonesia lies in the region which form the connection between Pacific Ocean and Indian Ocean, the ocean circulation variations are strongly affected by the monsoons [21]. Therefore, the simulation will be divided into two cases: (1) South East Monsoon case which use one month tide data of May 2017, and (2) North West Monsoon case which use one mont tide data of November 2017. Tidal increment is one hour while tidal constituent including principal lunar semidiurnal (M_2) and principal solar semidiurnal (S_2) according to Sunda Strait tide characteristic. Ocean circulation model can be estimated for four weeks prediction with two days spin-up simulation. As split time steps are used in current simulation, time step for external domain, in which water elevation and tidal current velocity can be computed in two-dimensional depth-averaged mode, is 1 second, and the time step for internal domain, in which tidal current, salinity, and temperature can be computed in three-dimensional mode, is 5 seconds. Environmental initial and boundary conditions are based on previous researches data which are achieved by performing field experiment. Ray [22] reported that ocean temperature in South East Monsoon (data June 2015) ranges from 29.5^{o}C near surface to 18^{o}C near sea bottom, while in North West Monsoon (data November 2015) ranges from 29.5^{o}C near surface to 21^{o}C near sea bottom. Pb (lead) concentrations as the main pollutant in Sunda Strait area are set as highest value in the sea bottom, that is 20 mg/L, as reported by Hosono [8] in both monsoon seasons. Other important factor in coastal environment is turbidity, because

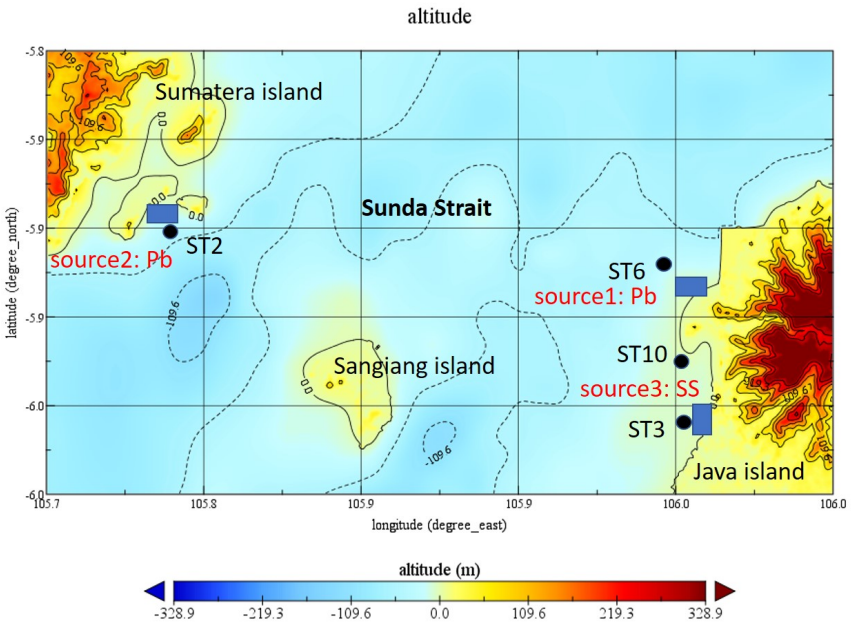

Figure 6.2: Topography map of Sunda Strait including pollutant point sources and monitoring points of numerical model

suspended solid (SS) in Sunda Strait area is very high, in range of 25 to 100 mg/L, especially near the south sill which is affected by strong wave from Indian Ocean, [23]. Therefore, SS value will also be included in the model and the distribution due to ocean circulation can be analyzed. Pb source point is located at Source1 and Source2 which represents large port in Java and Sumatera Island respectively, while SS source point is located at Source3, which lies at the southern coast of Java island, as shown in Fig.6.2.

After the tidal current and pollutant distribution in both seasons are obtained, the effects to aquaculture are studied by determine the direct influence of Pb (lead) concentration to phytoplankton algae as reported by Woolery [14] that Pb could inhibit photosynthesis process based on laboratory experiment. The photosynthesis rate was drastically decreased as the Pb concentration increased as shown in Fig.6.3. For more than 10mg/L Pb concentration, the photosynthesys rate is inhibited to 0% which lead to lethal condition[14]. The experiment object is *Bacillariophyceae* algae which is very common in Java sea [16]. By using this laboratory experiment results, the effect of Pb concentration on *Bacillariophyceae* algae photosythesis can be known in Sunda Strait area. The summary of computational conditions are shown in Table.6.1.

Table 6.1: Computational conditions

Case	Monsoon season	Location	Evaluated items
1	South East	Source1	Pb, Algae
		Source2	Pb, Algae
		Source3	SS
2	North West	Source1	Pb, Algae
		Source2	Pb, Algae
		Source3	SS

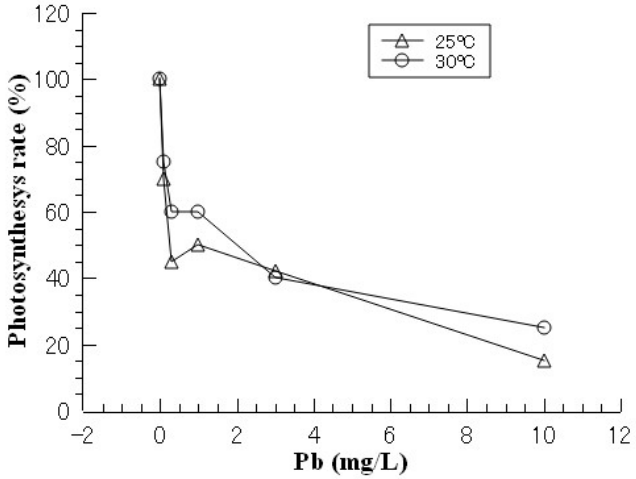

Figure 6.3: Photosynthesis rate of *Bacillariophyceae* algae after 72hours laboratory treatment [14]

6.3 Results and Validation

Firstly, SEM and NWM cases are validated by comparing water elevation from both computational results to tide data from Geospatial Information Agency Indonesia [24], which are generated from the assimilation of permanent tide stations and altimeters data, as shown in Fig.6.4. The simulation results show a good agreement with the field data with little discrepancy in the tide phase. The most notable differences are occur in the first and second day because at that period, the models are still in spin-up stage. In SEM case, tidal currents are mostly flowing from south sill to north sill, both at surface and near bottom, with maximum velocity of 1.5m/s, although there are lower velocity from north sill about 0.3m/s as shown in upper figure of Fig.6.5. In the other hand, NWM case shown in lower figure of Fig.6.5 has most of its tidal current flowing to the south sill with maximum velocity of 1.4m/s. The tidal currents are flowing strongly along the coastal area both in SEM and NWM cases as shown in Figs.6.6-6.8. Due to the tidal current flow characteristic in SEM case, Pb concentration spreads

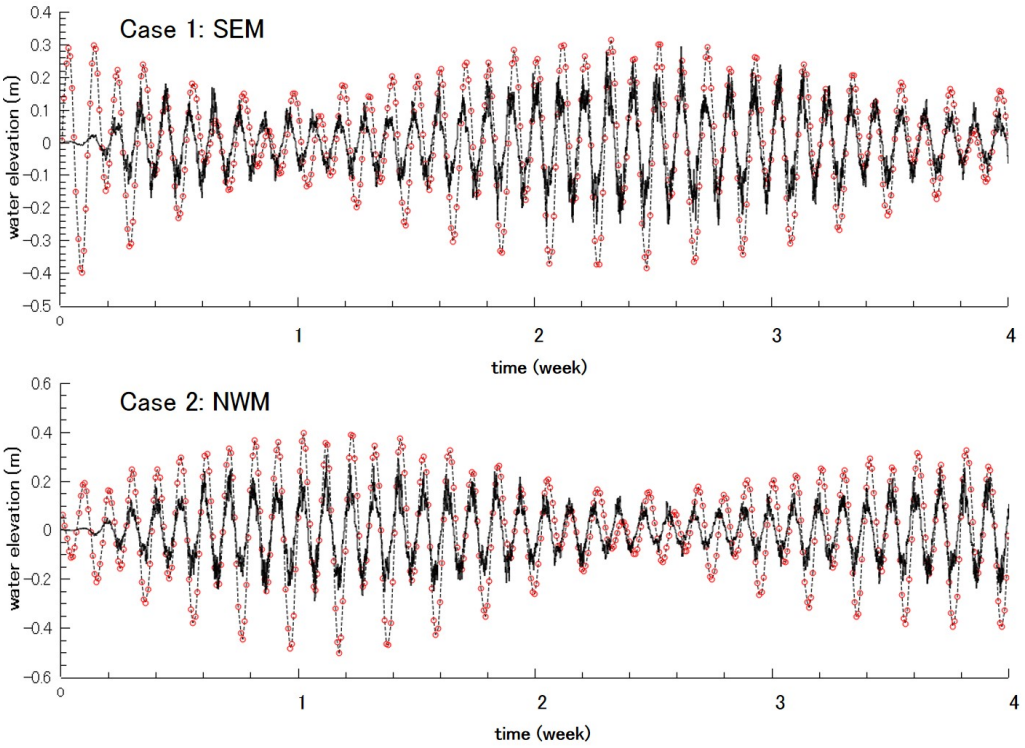

Figure 6.4: Water elevation of Sunda Strait in SEM and NWM season validated with tide data from Geospatial Information Agency Indonesia [24]

in the nothern area only even after 4 weeks, while SS, which originated from south coast of Java Island, spreads strongly to wider area in northern part of the strait. In NWM case, the tidal current flow helps Pb and SS concentrations to spread into further western part of the strait. Therefore, although the tidal current flow is lower, it distributes the ocean pollutant wider and evenly to other part of the strait. SS distribution is covering much larger area as shown in Fig.6.8 which could lead to wider effect on oxygen decrease and temperature rise[25]. In the other hand, the Pb concentration distribution is estimated to affect a very large area as shown in Fig.6.6 and 6.7 for SEM and NWM case respectively. After four weeks contamination from two point source of Pb west and east coast of Sunda Strait, the photosynthesis rate in the 5km radius from the source 1 is decreased to 0% which means the phytoplankton algae is in lethal condition, both in SEM and NWM cases. However, in NWM case, 60-75% photosynthesys rate area are wider and those could lead to less production of phytoplankton algae in Sunda Strait area. The time histories also shown that during SEM season, ST6, located near Source1, is contaminated with high Pb concentration which cause algae photosynthesys rate decrease to less than 20% at several periods. This results also validated by Suwandana report from

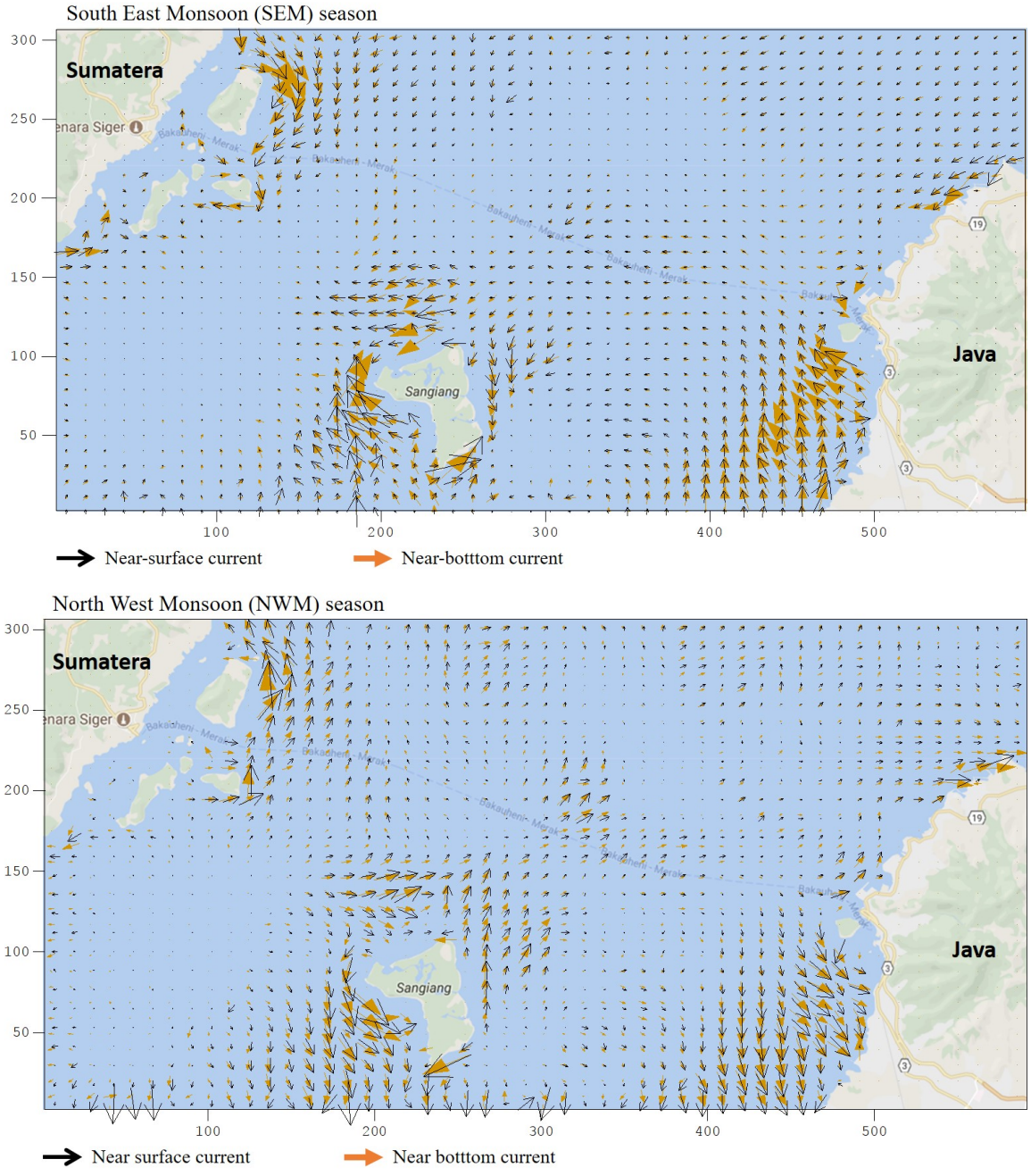

Figure 6.5: Tidal current flow in Sunda Strait at different monsoon season

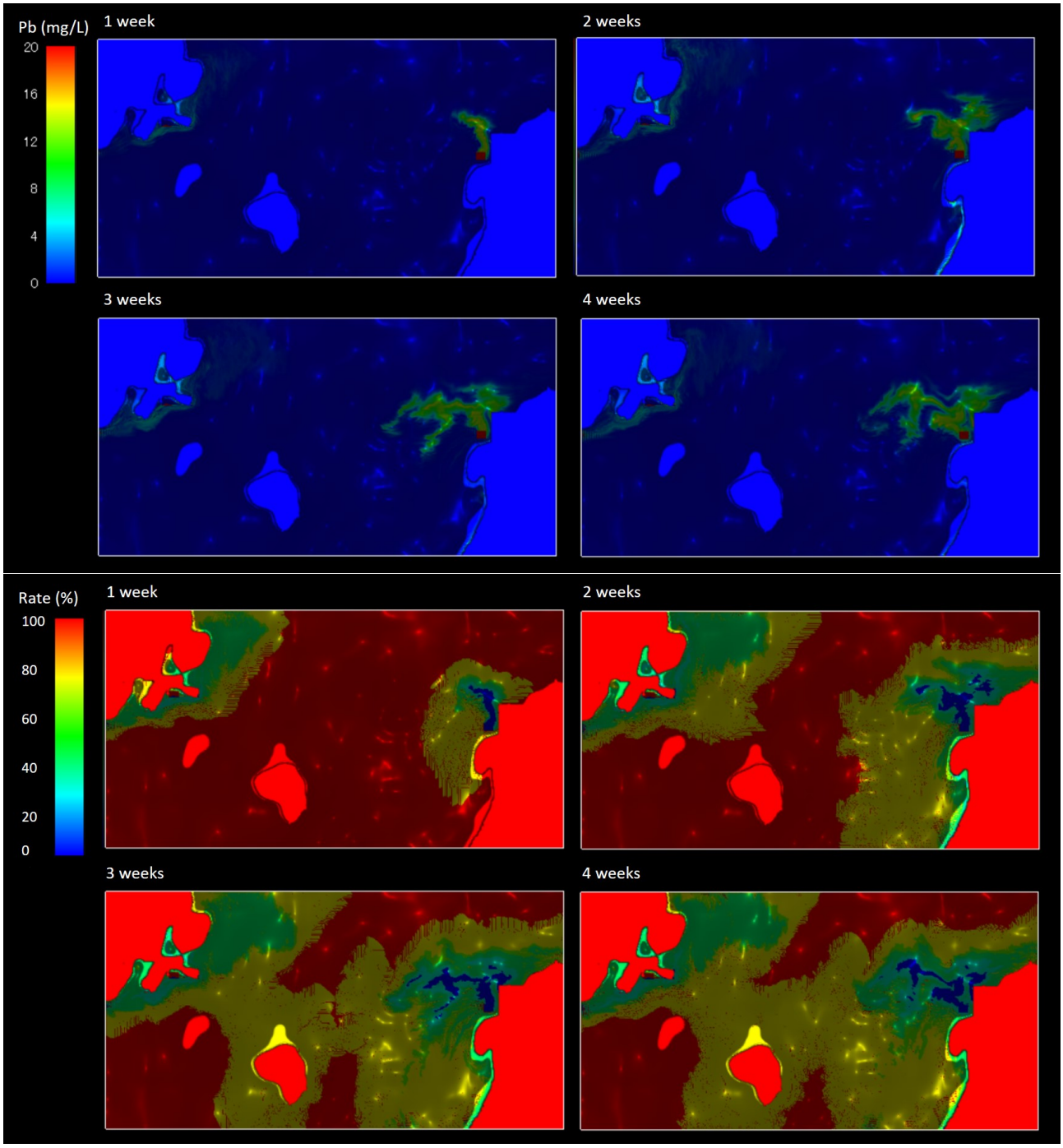

Figure 6.6: Pb distribution from point-sources due to tidal current flow and Algae photosynthesis rate due to Pb contamination in SEM season

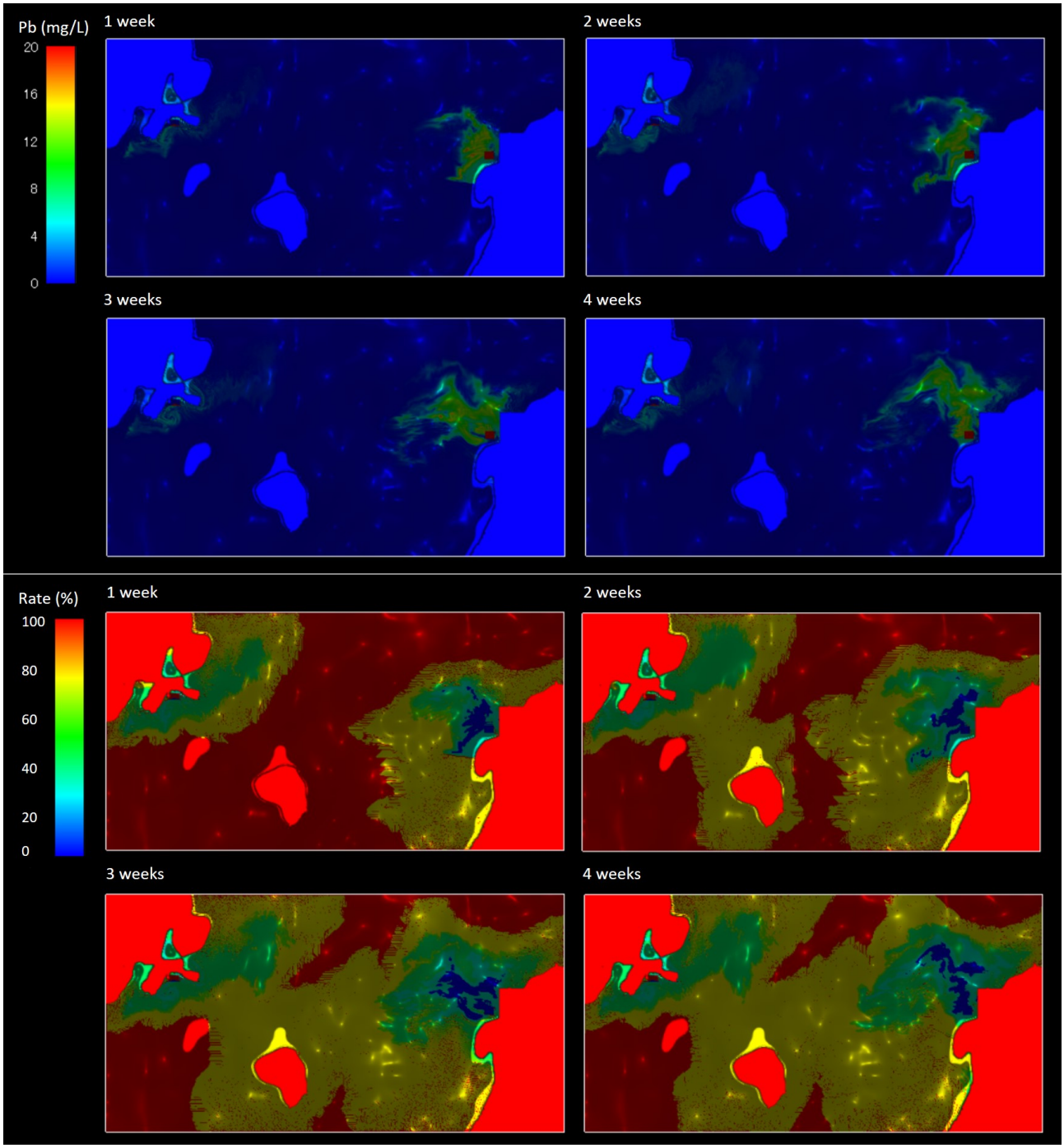

Figure 6.7: Pb distribution from point-sources due to tidal current flow and Algae photosynthesis rate due to Pb contamination in NWM season

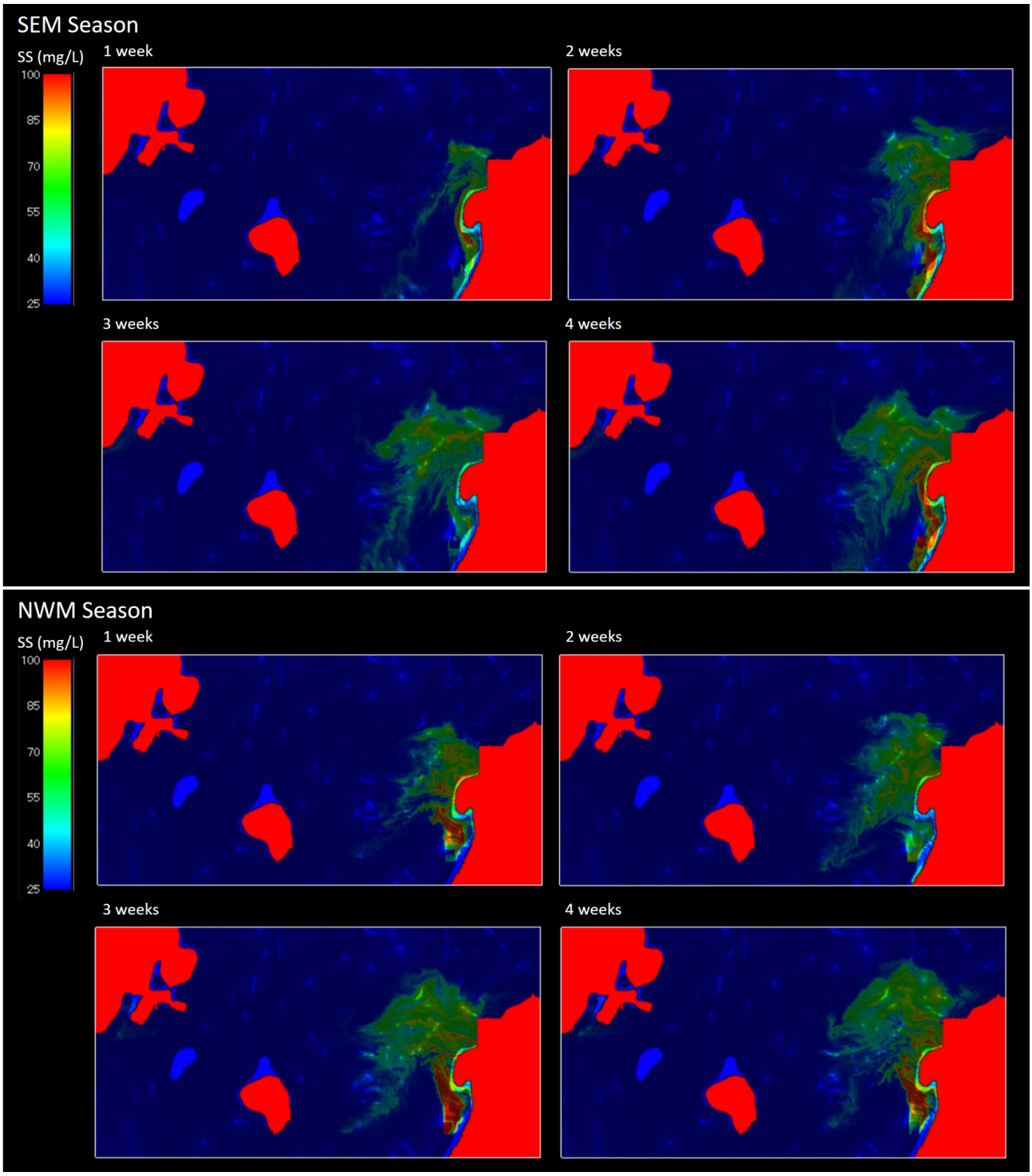

Figure 6.8: distribution from point-sources due to tidal current flow in SEM and NWM season

field experiment in SEM season 2010, who found the Pb concentration at north side of Sunda Strait about 10mg/L [11]. In the other hand, Pb contamination is low at ST2, located near Source2, about 2-4 mg/L. Despite low Pb concentration, it still affect algae photosynthesys rate which reduced to 40%. Otherwise, in NWM season, ST6 affected by lower Pb concentration, about 4 mg/L which lead to 40% algae photosynthesys rate, while ST2 contains higher Pb concentration with maximum 8 mg/L which caused lower algae photosynthesys rate in range of 30-80%. Refers to field data in SEM season 2010 and 2011 from [17], Phytoplankton abundance and biodiversity were significantly higher in Sunda strait, about 9.75×10^3, compared to other locations near Java Sea[26][27][28]. It can be concluded that marine pollution in Sunda Strait area could lead to large ocean primary production and significantly affect the fisheries and other aquaculture sectors results[29]. Based on time history of suspended solid results at ST3 and ST10 which located near SS point-source Source3, the SS concentrations are very high. At St10, SS concentrations are within range of 50-90 mg/L in SEM, and 40-90 mg/L in NWM. High concentrations of SS are causing high turbidity which can reduce sunlight penetrates in water and decrease the algae phosynthesys rate, although those phenomena are common in tropic country with high rainfall intensity thus lead to sediment washoff from land, especially in esturary area [30].

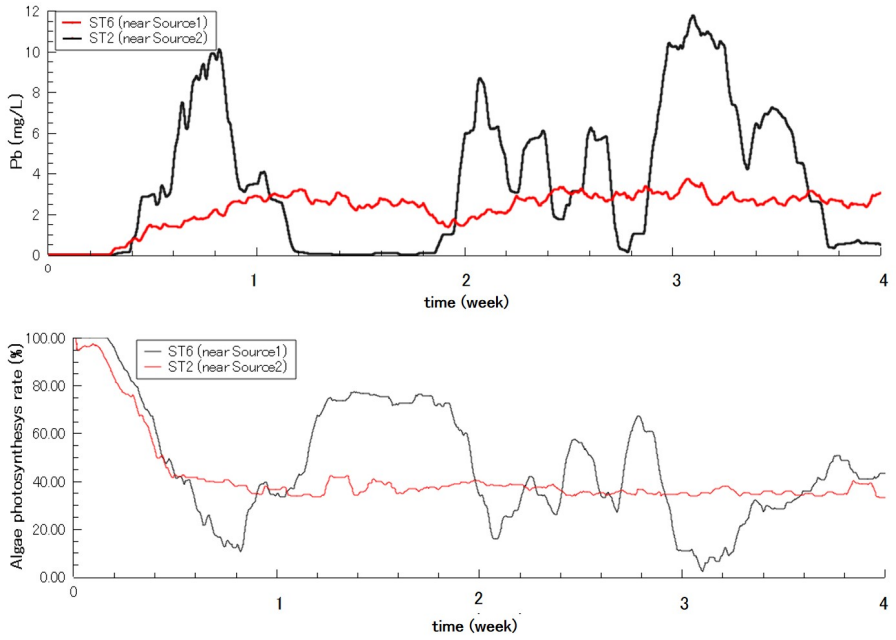

Figure 6.9: Time histories of Pb concentration and algae photosynthesys rate in Sunda Strait during SEM season

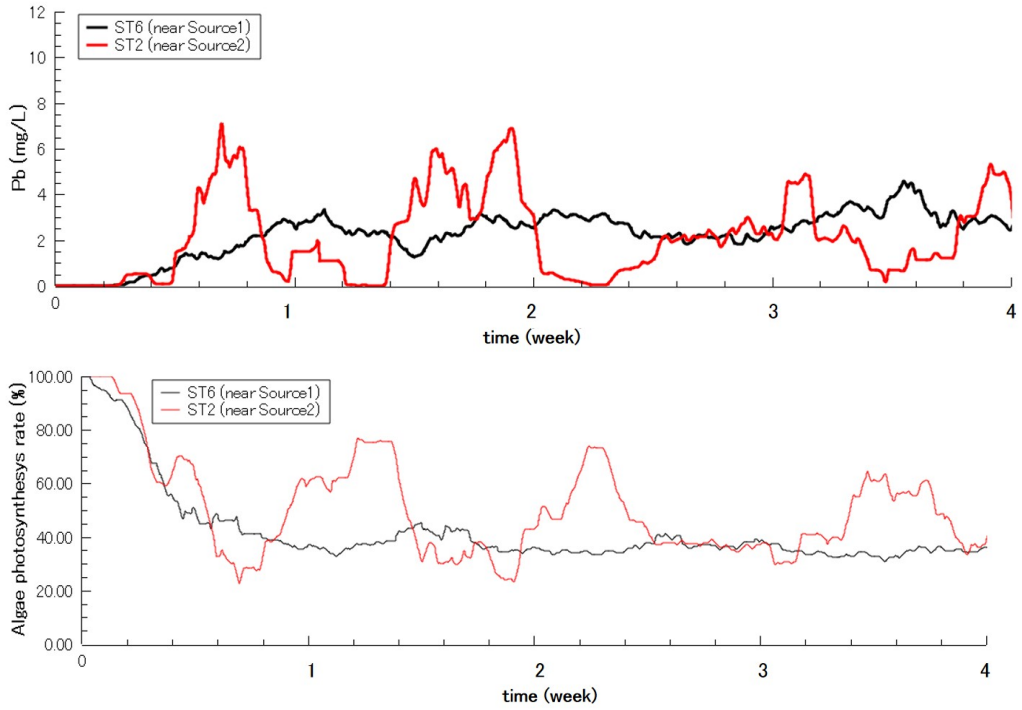

Figure 6.10: Time histories of Pb concentration and algae photosynthesys rate in Sunda Strait during NWM season

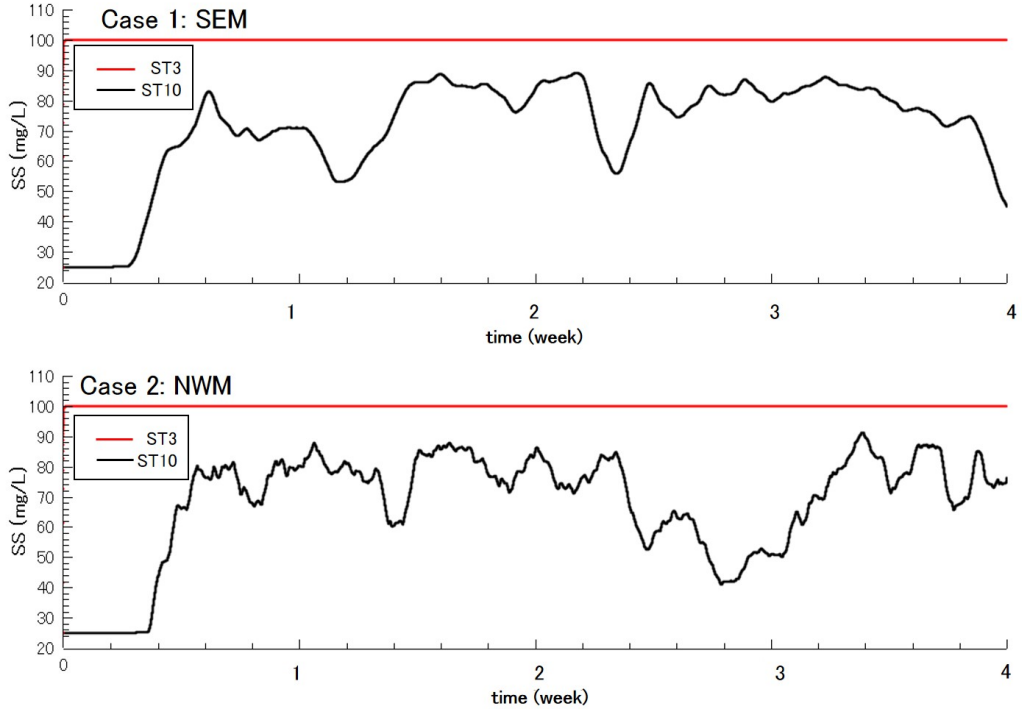

Figure 6.11: Time histories of SS concentration in Sunda Strait during SEM and NWM season

6.4 Conclusions

Environmental analyses of marine pollution in Sunda Strait, which consider the tidal current flow in South East Monsoon (SEM) and North West Monsoon (NWM) seasons are simulated for one month period at each case. Validations with field data shows good agreement with little discrepancy which does not affect the end results of the simulations. SEM case results show dominant flow to the north which affect the Pb (lead) and Suspended Solid (SS) concentration distribution. In NWM case, tidal current flows to south mostly and spread Pb and SS concentration to wider area from the east to the west side of the strait. This is also affect more contaminated area which has lower photosynthesis rate of phytoplankton algae, about 60-75%. Meanwhile, in 5km radius from Source 1 of Pb concentration, photosynthesis rate is very low, or nearly 0%, and threaten the living ability of the phytoplankton algae. Moreover, high SS concentration phenomena in Sunda Strait as part of tropic area could also decrease algae photosynthesis rate because of less sunlight penetration.

Bibliography

[1] A. Soegiarto. Introduction to The Regional Oceanography of The South East Asian Waters. In Food and Agriculture Organization of the United Nations, editor, *Lectures presented at the fifth FAO/SIDA Workshop on Aquatic Pollution in Relation to Protection of Living Resources*, pages 1–11, Manila, 1978. Food and Agriculture Organization of the United Nations.

[2] Ministry of Marine Affairs and Fisheries Banten Province. Statistic Report 2014. Technical report, Serang, Banten, 2014.

[3] Fadilah, Zainal Abidin, and Umi Kalsum. Household Income and Welfare of Torch Fisherman in Bandar Lampung City (in Indonesian). *JIIA*, 2(1):71–76, 2014.

[4] Ministry of Marine Affairs and Fisheries Indonesia. Number of National Fishing Equipment, 2012.

[5] Ririn Irnawati, Adi Susanto, Mustahal, and Mohamad A Syabana. AES BIOFLUX Heavy metals concentration in water and sediment at Panjang Island, Serang Regency, Banten Province, Indonesia. *AES Bioflux*, 6:256–260, 2014.

[6] Faiza Fauziah and Devi N. Choesin. Accumulation of Pb and Cu heavy metals in sea water, sediment, and leaf and root tissue of Enhalus sp. in the seagrass bed of Banten Bay. In *AIP Conference Proceedings*, volume 1589, pages 329–333, 2014.

[7] Tri Muji Susantoro, Djoko Sunarjanto, and Ariani Andayani. Distribution of Heavy Metal in Sediment at Coastal Area Jambi Province. *Jurnal Kelautan Nasional*, 10(1), 2015.

[8] Takahiro Hosono, Chih Chieh Su, Robert Delinom, Yu Umezawa, Tomoyo Toyota, Shinji Kaneko, and Makoto Taniguchi. Decline in heavy metal contamination in marine sediments in Jakarta Bay, Indonesia due to increasing environmental regulations. *Estuarine, Coastal and Shelf Science*, 92(2):297–306, 2011.

[9] Kees Booij, M. Theo J Hillebrand, Rob F. Nolting, and Jan Van Ooijen. Nutrients, trace metals, and organic contaminants in Banten Bay, Indonesia. *Marine Pollution Bulletin*, 42(11):1187–1190, 2001.

[10] Naoyuki Sakumoto and Hikmahanto Juwana. Reforming Laws and Institutions in Indonesia: An Assessment. Technical report, Institute of Developing Economics, 2007.

[11] Endan Suwandana, Kensuke Kawamura, and Endro Soeyanto. Assessment of the Heavy Metals and Nutrients Status in the Seawater, Sediment and Seagrass in Banten Bay, Indonesia and Their Distributional Patterns. *Journal of Fisheries International*, 6(1):18–25, 2011.

[12] Zainal Arifin, Rahma Puspitasari, and Nobuyuki Miyazaki. Heavy metal contamination in Indonesian coastal marine ecosystems: A historical perspective. *Coastal Marine Science*, 35(1):227–233, 2012.

[13] Tommy Martho Palapa and Alfonds Andrew Maramis. Heavy Metals in Water of Stream Near an Amalgamation Tailing Ponds in Talawaan – Tatelu Gold Mining, North Sulawesi, Indonesia. *Procedia Chemistry*, 14:428–436, 2015.

[14] Marti L. Woolery and Ralph A. Lewin. The effects of lead on algae. *Water, Air, and Soil Pollution*, 6(1):25–31, Aug 1976.

[15] John J. Walsh. Steemann nielsen, e. 1975. marine photosynthesis with special emphasis on the ecological aspects. elsevier sci. publ. co., amsterdam and new york, x + 142 p.21-75. *Limnology and Oceanography*, 21(4):633–633, 1976.

[16] N T M Pratiwi, D Y Wulandari, I P Ayu, and A Iswantari. Diversity and Spatial Distribution of Plankton in Connected Waters of Bali Strait, Between Eastern Part of Java and Western Part of Bali Island. *IOP Conference Series: Earth and Environmental Science*, 54(1):12090, 2017.

[17] Zhixin Ke, Yehui Tan, Yane Ma, Liangmin Huang, and Songbo Wang. Effects of surface current patterns on spatial variations of phytoplankton community and environmental factors in Sunda shelf. *Continental Shelf Research*, 82:119–127, 2014.

[18] George L Mellor. *Users guide for a three-dimensional, primitive equation, numerical ocean model*, volume 8544. 2002.

[19] V. M. Kamenkovich and D. A. Nechaev. On the time-splitting scheme used in the Princeton Ocean Model. *Journal of Computational Physics*, 228(8):2874–2905, 2009.

[20] Laurie Padman. Tide Model Driver (TMD) Manual. *Arctic*, pages 1–12, 2004.

[21] Klaus Wyrtki. Physical Oceanography of the Southeast Asian waters. Technical report, The University of California, California, 1961.

[22] Richard D. Ray and R. Dwi Susanto. Tidal mixing signatures in the Indonesian seas from high-resolution sea surface temperature data. *Geophysical Research Letters*, 43(15):8115–8123, 2016.

[23] Helfinalis. Total Suspended Solid Content And Sediment On The Bottom Surface Of Panimbang Water. *Makara Seri Sains*, 09(2):45–51, 2005.

[24] Geospatial Information Agency Indonesia. Online Tide Prediction, 2017.

[25] Harashit Kumar Mandal. Assessment of wastewater temperature and its relationship with turbidity. *Recent Research in Science and Technology*, 6(1):258*262, 2014.

[26] H. Thoha, Q. Adnan, T. Sidabutar, and Sugestiningsih . Note on The Occurence of Phytoplankton and Its Relation with Mass Mortality in The Jakarta Bay, May and November 2004. *MAKARA of Science Series*, 11(2), oct 2010.

[27] Hefni Effendi, Mujizat Kawaroe, Dea Fauzia Lestari, Mursalin, and Tri Permadi. Distribution of Phytoplankton Diversity and Abundance in Mahakam Delta, East Kalimantan. *Procedia Environmental Sciences*, 33:496–504, jan 2016.

[28] Dong-Yang Cui, Jiang-Tao Wang, Li-Ju Tan, and Ze-Yi Dong. Impact of atmospheric wet deposition on phytoplankton community structure in the South China Sea. *Estuarine, Coastal and Shelf Science*, 173:1–8, may 2016.

[29] S. M. Vallina, M. J. Follows, S. Dutkiewicz, J. M. Montoya, P. Cermeno, and M. Loreau. Global relationship between phytoplankton diversity and productivity in the ocean. *Nature Communications*, 5, jul 2014.

[30] S.H. Le, L.H.C. Chua, K.N. Irvine, and H.S. Eikaas. Modeling washoff of total suspended solids in the tropics. *Journal of Environmental Management*, 200:263–274, sep 2017.

Chapter 7

Conclusions and Future Works

7.1 Conclusions

In this final chapter, the results of this research which based on objectives in Chapter 1 are briefly described. Considering that for several aspects only a preliminary investigation which then could be executed, suggestions of future works are also presented.

The topic of the dissertation is motivated by the desire to understand in more detail not only the ocean potential including renewable energy, fishery, and aquaculture, but also the environmental problems that occurred due to human activity, especially in archipelago area. Both aspects should be balanced to keep ocean resources sustainability. After conducting this study, the main conclusions drawn are summarized as following.

- Indonesian archipelago is chosen as it is one of the largest tidal current resource in the world. Investigation on tidal current characteristics and its energy potential shows that the tidal current velocity is relatively high in narrow straits at Maluku islands and Nusa Tenggara islands. In particular, Lombok strait is the most notable location with the maximum tidal current velocity, 4m/s. The narrow straits at Nusa Tenggara islands can produce more than 2.8m/s for tidal current and more than 12kW/m^2 for tidal current energy. In the northern and the southern part of Halmahera island, the resultant tidal

current kinetic power also produces about 5kW/m^2. The tendency of tidal current at Lombok strait and Maluku sea is almost south direction and therefore a small sized Horizontal Axis Turbine (HAT) is appropriate for the flow conditions to generate electric power with high efficiency to avoid ocean environmental damages caused by installing and operating HAT and to suitably supply electric power with low transmission cost to local living people.

- In order to harvest the tidal current energy in Indonesia and distribute it to local communities, a small-sized HAT 10kW class with the diameter 2.2m, was theoretically and numerically designed and optimized considering the specific tidal-current at the archipelago areas, and also velocity field around the designed turbine and pressure distribution on it were examined. The designed turbine can generate electric power for more than one hundred people at Lombok strait. The power distribution produced by the designed turbine was mapped by using the estimated power curve at Maluku islands and Nusa Tenggara islands.

- For country with aquaculture such as Indonesia and Japan, small-sized tidal current turbine can be combined with Fish Aggregating Device (FAD) considering several sea states for practical use. FAD can also be utilized as a scientific platform to produce environment-friendly ecosystem by an artificial infrastructure. In this study, a mooring type of FAD with Horizontal Axis Turbine (HAT) and Vertical Axis Turbine (VAT) was designed considering collision with a marine vertebrate, fish and a rotational turbine. The designed FAD has been optimized to reduce fluid force and motion using elastic mooring. In Indonesian archipelago area, the estimated electric power could reach 220W in Bali strait and 700W in Lombok strait, due to higher current velocity, by using the mooring type of FAD with the designed turbine. It could be adequate to turn on LED for gathering fishes and to boot up and activate several sensors such as beacon, ocean environmental, disaster and security devices.

- In order to accomplish the balance between coastal development and ecosystem sustainability, environmental research should be conducted especially in urban coastal area such

as enclosed sea in Japan. Study on hydrogen sulfide reduction in order to recover ocean environment by utilizing recycled material had been conducted using Eulerian-Lagrangian model with ocean circulation model in order to consider fluid-particle interaction between tidal current and steelmaking slag, and advection-diffusion of dissolved sulfide. The model was also applied to Fukuyama inner harbor and Tokyo Bay using the experimental and field data. The numerical results demonstrated that steelmaking slag can control advection-diffusion of concentration of DO and H_2S which is highly toxic and fatal to benthic organisms and it causes oxygen-deficient water and the blue tide at the dredged trench in Tokyo Bay. Accordingly, steelmaking slag could improve organically enriched sea bottom in enclosed sea area.

- Preliminary assessment of ocean pollution effect on fishery and aquaculture is a very important step in order to prevent further marine production loss and ocean environmental damage in Indonesian seas. By considering tidal current flow in different monsoon season in Indonesia, pollutant distribution can be estimated and spatial effect on marine aquaculture can be predicted, which was not achieved in other researches before. Sunda Strait is chosen to be specific study site because it is one of important strait where industry, transportation, and tourism are heavily established, while fishery has been a major income for local communities. Environmental analyses of marine pollution in Sunda Strait, which consider the tidal current flow in South East Monsoon (SEM) and North West Monsoon (NWM) seasons are simulated for one month period at each case. Pb (lead) has chosen as the main contaminant because of its high concentration in this area. Validations with field data shows good agreement with little discrepancy which does not affect the end results of the simulations. SEM case results show dominant flow to the north which affect the Pb (lead) and Suspended Solid (SS) concentration distribution. In NWM case, tidal current flows to south mostly and spread Pb and SS concentration to wider area from the east to the west side of the strait. This is also affect more contaminated area which has lower photosynthesis rate of phytoplankton algae, about 60-75%. Meanwhile, in 5km radius from Source1 of Pb concentration, photosynthesis rate is very low, or nearly 0%, and threaten the living ability of the phytoplankton algae. Moreover, high SS concentration

phenomena in Sunda Strait as part of tropic area could also decrease algae photosynthesis rate because of less sunlight penetration.

7.2 Future Works

From this study, an enhanced understanding has been gained in the tidal current energy resources and ocean environment assessment in order to keep fishery and aquaculture sustainability. Some recommendations for further research are presented below.

Tidal current energy harvesting

The electric performance of the small-sized HAT should be evaluated considering seasonal and annual variation of tidal-current and ITF using more fine grids to survey a hot spot for installing a tidal-current harvester. Experiment and fields tests should also be conducted with a prototype to examine hydrodynamic and electric performance of the designed turbine.

Fish Aggregating Device (FAD) with an ocean energy harvester

Unsteady motions of FAD with an ocean energy harvester should be directly considered in theoretical and numerical works to investigate fully nonlinear fluid-structure interaction. The power coefficient should be also validated with field data and efficiency regarding with loss of gear, generator etc. should be considered in practical use.

Eulerian-Lagrangian coupling model

More detailed validation on the numerical model should be quantitatively conducted and also a more sophisticated model should be developed in physical-chemical interaction process between slag and sea water.

Investigation on marine pollution in Indonesia

The dynamic wind and river discharges data from each monsoon season should be included in future numerical model, as it play important roles in water contaminant and sediment distribution in coastal area. Furthermore, the ocean pollution effect on fishery and marine aquaculture should be supported by detailed data of marine biota abundance and specific physical and biogeochemical mechanism should be included in the numerical model so that the ecosystem model can be well described.